ELECTROMAGNETIC FIELD SOLUTION WITH THE BOUNDARY ELEMENT METHOD

A THESIS SUBMITTED TO
THE FACULTY OF GRADUATE STUDIES
IN PARTIAL FULFILLMENT
OF THE REQUIREMENTS FOR THE DEGREE
DOCTOR OF PHILOSOPHY

BY
MENG HIN LEAN
DEPARTMENT OF ELECTRICAL ENGINEERING
THE UNIVERSITY OF MANITOBA
WINNIPEG, CANADA

JULY 1981

ELECTROMAGNETIC FIELD SOLUTION WITH THE BOUNDARY ELEMENT METHOD

BY

MENG HIN LEAN

A thesis submitted to the Faculty of Graduate Studies of
the University of Manitoba in partial fulfillment of the requirements
of the degree of

DOCTOR OF PHILOSOPHY

To the 連 (Lean) family

ABSTRACT

The Boundary Element Method (BEM) is shown to be a viable mechanism for the solution of field problems posed in integral form. It allows parametric representation of surfaces and sources to high fidelity, with the use of expansion functions derived from the Lagrange interpolation scheme. A variational solution is obtained using the Rayleigh-Ritz technique to construct a minimizing sequence that is guaranteed to converge in *energy*. The parallel of the variationally derived system of equations to that obtained from a direct application of Galerkin's method is discussed. A novel numerical scheme, fully automated to cater for Green's function singularities over arbitrarily-shaped contours or boundaries, is described in detail. Source singularities due to geometry — corners or edges — are treated by using a trial function of the appropriate form and order. An added flexibility is provided by the ability to tailor-design Gauss quadratures to obtain optimal precision with minimim sampling. Exemplary treatments to electrostatic, interface, and electromagnetic scattering problems are discussed. Qualitative and where possible, quantitative comparisons are made with the moment method (pulse expansion, point-matching) solution.

ACKNOWLEDGEMENTS

The author wishes to thank Professor A. Wexler, advisor and friend, for his counsel, guidance and encouragement over the course of this work.

Professor L. Shafai is thanked for many helpful discussions.

Special thanks and appreciation are due to the author's wife, Wei-Ping and son Chia-Wen for their unwavering support and encouragement over the recent trying times.

The author is grateful to Xerox Corporation for financial support. The staff at ADL, Palo Alto Research Centers, are thanked for many helpful discussions. In particular, Dr. Dan Bloomberg is thanked for his interest in this topic; his many stimulating talks; and finally, his friendship.

Mary-Ann Tyler is thanked for her consideration, diligence and splendid work in the typing of this manuscript.

Financial support from the Natural Sciences and Engineering Research Council of Canada is gratefully acknowledged.

TABLE OF CONTENTS

LIST OF FIGURES

LIST OF TABLES

I. INTRODUCTION

Integral formulations of static and time-harmonic boundary value problems involve a general class of linear Fredholm integrals with singular kernels. The mathematical conditions for existence of solutions to such equations are well documented in the literature (*e.g.*, Stakgold (1967) and Zabreyko *et al* (1975)). A Fredholm second kind integral is expressible as

$$\int_a^b k[x|x']\, f(x')dx' - \lambda f(x) = g(x) \qquad [1.1]$$

where f is defined everywhere on the interval $[a,b]$ which may be infinite, and $k[x|x']$ may be an unbounded function of x and x'. The first kind integral results when λ vanishes. Provided λ is not an eigenvalue, [1.1] will have a unique solution if the kernel $k[x|x']$ is square-integrable, *i.e.*,

$$\| k \|^2 = \int_a^b \int_a^b \left| k[x|x'] \right|^2 dxdx' < \infty \qquad [1.2]$$

thus signifying a bounded operator, and $g(x)$ has a finite norm

$$\| g \| = \left[\int_a^b |g(x)|^2 dx \right]^{\frac{1}{2}} < \infty \qquad [1.3]$$

Classical methods of solution to [1.1] include: variational, perturbation, complex variable, iterated kernels, and asymptotic techniques (Noble, 1971a), which attempted to generate closed-form solutions in terms of standard mathematical functions. The dependence of such solutions on problem geometry and boundary conditions necessarily limits their scope of application. With the introduction of the digital computer,

a class of numerical schemes broadly classified as moment methods (Harrington, 1968) rapidly gained significance. The theoretical concepts necessary for a discussion of numerical solution methodology include prior knowledge of linear function spaces and operators (*e.g.*, Stakgold (1979)). With a minimum of mathematical rigour, consider the general statement of an integral equation problem

$$Kf = g \qquad [1.4]$$

where K is a linear operator, f the unknown function that lies in its domain, and g the known excitation in its range. Allow f to be expressed as

$$f = \sum_n \alpha_n f_n \qquad [1.5]$$

such that α_n are linearly independent expansion functions, and f_n the collection of unknowns. A residual error term indicative of the accuracy of representation in [1.5] is given by

$$e = \sum_n [K\alpha_n] f_n - g \qquad [1.6]$$

using the linearity of K. A set of linearly independent weights w_m, also called testing functions, is now selected to produce a projection of the error term on its space as

$$< w_m, e > \equiv \sum_n < w_m, [K\alpha_n] > f_n - < w_m, g > \qquad [1.7]$$

where the angular brackets denote an inner product defined by

$$< u, v > = \int uv^* \, d\Omega \qquad [1.8]$$

and the asterisk signifies conjugate in the event u and v are complex.

By setting the left-hand side of [1.7] to zero, the physical significance is that the set w_m minimizes the error term and the moment method expression

$$\sum_n < w_m, [K\alpha_n] > f_n = < w_m, g > \qquad [1.9]$$

(Harrington, 1968) results. The choice of testing functions w_m is seen to indicate specializations of [1.9]. The Galerkin method ensues if $w_m = \alpha_m$, and the least-squares approximation if $w_m = K\alpha_n$ (Stakgold, 1967).

The most popular implementation of [1.9] involves sub-domain bases for subsectional collocation — pulse expansion and Dirac delta functions for testing (point-matching). This is without doubt the easiest to implement and economically the cheapest to use, since only one integration need be performed as the boundary conditions are relaxed so that they are now *matched* only at discrete *points* (the geometric centre of collocation sections). A similar version — the *method of subareas* was used by Reitan & Higgins (1951) for the calculation of capacitances. Early practitioners include Andreasen (1965), Oshiro & Su (1965), Harrington (1968) and Richmond (1969) in electromagnetics; and Noble (1971b) and Jaswon & Symm (1977) in electrostatics and potential theory. Quite remarkable precision has been reported especially by Burke & Poggio (1977) on NEC, an industrially available NUMERICAL ELECTROMAGNETIC CODE, notwithstanding the crude, discontinuous planar-patch approximation.

The numerical solution of integral equation field problems requires: (i) accurate representation of both geometry and sources; and (ii) precise approximation to the integral operation. With regard to the former, the earlier planar-patch schemes exhibit immediate geometrical

modelling error for surfaces with curvature. Increasing N, the number of planar patches, would only improve results to a point, after which, round-off error predominates and a rapidly vanishing determinant leads to matrix ill-conditioning. Furthermore, with the crude integration scheme used (as in NEC), the numerical solution will never approach the *exact* since off-diagonal entries are not exact in the limit of increasing N (Harrington, 1968). Cruse (1974) reported improved field solution on assigning linear variation of sources over planar patches. McDonald *et al* (1974) implemented the Rayleigh-Ritz variational formulation that converged in energy — a theoretical guarantee that was lacking in the traditional moment method solution, though at a cost of increased overhead for matrix fill. Lachat (1975) and later Lachat & Watson (1976) and Nedelec (1976) were the pioneers in the use of parametric representations for sources and geometry. Jeng (1977) used high-order Lagrange interpolation for both sources and geometry in conjunction with a variational method for solution. This isoparametric (both sources and geometry modelled to same degree) implementation was seen to produce either, better accuracy with the same number of variables, or comparable precision with a lesser number of variables when compared to the point-matching scheme, at least for static field problems. More importantly, the solution was observed to be less dependent on the disposition of sampling positions.

In the numerical approximation to the integral operation with Gauss quadratures, the integrand is expressed as a polynomial and treated in exact fashion. Due to inefficient use of quadrature formulas, it is not uncommon to have a major portion of CPU time devoted exclusively to this operation. The resort to analytical integration, partly as a measure for the reduction of overhead, but also for the attainment of

Cauchy principal values for the kernel singularity, is geometry dependent and restricts accuracy to planar surfaces. The work to be reported herein concerns the Boundary Element Method (BEM), an algorithmic package that has some basic similarities in solution methodology to that of Jeng (1977). Notable features incorporated into the code include an automated numerical scheme to handle Green's function singularities on arbitrarily shaped boundaries, and the facility to tailor-design quadratures to obtain optimal precision with minimal sampling.

Chapter II will involve a comprehensive account of the BEM algorithm. A detailed discussion on the crucial aspects of kernel singularities and their treatment by the BEM algorithm will be carried out in Chapter III. While the intent is to illustrate the viability of the BEM as a high-order, self-consistent numerical code for field problems, the attempt to discriminate between alternative formulations of the same problem is also stressed. The family of BEM codes include MANBEP-2DS (Lean & Wexler, 1980), MANBEP-3D (Lean & Wexler, 1979a) and other attendent versions designed to cater for electrostatic field, permeable media magnetic, and time-harmonic electromagnetic scattering problems which are the subject of discussion in Chapters IV, V and VI, respectively. In particular, the coverage of Chapters IV and V may be extended to include the dual problems of magnetostatic fields and electrostatic interfaces.

II. THE BEM ALGORITHM

The BEM has the capability to model arbitrary-shaped boundaries through a piecewise assembly of parametric, non-planar boundary elements (collocation sections). Sub-domain basis (expansion) functions of appropriate order are used in conjunction with specified node-point coordinates to attain very precise geometrical definition. Intra-element source variation is handled by the same type of basis functions so that use of the same order results in an *isoparametric* scheme. By extension, *superparametric* and *subparametric* would mean a higher fidelity in geometrical representation than source variation and vice versa (Wexler, 1980). Each element in n-dimensional *global* space is linked by a mapping to a standard simplex in *local* n - 1 space. This scheme leads to algorithmic simplicity and a consequent reduction in overhead since expansion functions and quadrature data need to be specified only once on the simplex.

Problem discretization is via the Rayleigh-Ritz procedure on the variational functional which can be shown to result in a form identical to Galerkin's method. In the accumulation of matrix entries, Gauss quadratures (Stroud & Secrest, 1966) of appropriate order and form are solicited for precise integration over each element. In particular, singularities introduced through the use of Green's functions and their derivatives are handled accurately by a fully automated numerical scheme. Source singularities due to geometry (*i.e.*, edges or corners) may be treated by attaching the form of the limiting behaviour to the Gauss quadrature weight function whereby the zeros of the resultant polynomial would take into account the discontinuity. By tailoring Gauss quadratures for the relevant application, required precision can be attained with

minimal sampling. A welcomed consequence of these innovative treatments is that matrix diagonal strength is enhanced, thus further ensuring the well-conditioning of the matrix.

The integral equation-generated matrix is usually dense thus precluding the use of sparse matrix routines at least in the present form. The chosen mode of matrix solution is triangularization which is of order N^3 but still three times more efficient than matrix inversion (Miller & Poggio, 1978). Depending on application — as in reanalysis — it may be more economical to store the matrix in inverted form. Solution through iteration is of order N^2 but requires total reanalysis whenever the excitation function is changed.

2.1 The Variational Functional

For the integral equation posed in [1.4], an energy product may be defined by $< f, g >$ which is assumed to conform to the axioms appertaining to the scalar product of functions. If operator K is real and self-adjoint, *i.e.*

$$< Ku, v > = < u, Kv > \qquad [2.1]$$

for all u, v in the domain of K, then the solution of [1.4] occurs at the stationary point of the quadratic functional

$$F(f) = < Kf, f > - 2 < f, g > \qquad [2.2]$$

and if K is also positive-definite, *i.e.*

$$< Kf, f > > 0 \qquad [2.3a]$$

for all $f \neq 0$ and vanishes only when $f = 0$, then the stationary point

corresponds to a minimum of F (Mikhlin, 1964). The requirement [2.1] means that the Fredholm kernel is symmetric and K is the Hilbert-Schmidt operator. The positive-definiteness of K implies uniqueness of solution. A physical interpretation of $\langle f,g \rangle$ the energy product, is that energy must be expended in giving a displacement f to the system. Furthermore, if operator K is also positive-bounded-below, *i.e.*

$$\langle Kf, f \rangle \geq \gamma^2 \| f \|^2 \qquad [2.3b]$$

where $\| f \|$ is the norm or scalar measure of displacement f, and γ is a positive constant, then this means convergence in the *mean* as well. This form of convergence implies that the norm of the difference between the nth term of the series approximation and the exact solution vanishes in the limit as $n \to \infty$.

The Rayleigh-Ritz procedure is a method of constructing a minimizing sequence that seeks a minimum for F. The sequence α_n has to satisfy two conditions: (i) it must be *complete* in energy; and (ii) it must be linearly independent. Condition (i) is satisfied if f can be approximated by a linear combination of a finite number of coordinate functions α_n (from [1.5]), to an arbitrary degree of precision. The second condition is met when $\alpha_1, \alpha_2, \ldots, \alpha_n$ are identically zero for $f = 0$. Rewriting [1.5] in matrix notation as

$$f = \underline{\alpha}^T \underline{f} = \underline{f}^T \underline{\alpha} \qquad [2.4]$$

where underlining bars denote column vector and T matrix transpose, the first derivative of [2.2] with respect to $\underline{f}$ is

$$\frac{\partial F}{\partial \underline{f}} = 2 \langle \underline{\alpha}, K\underline{\alpha}^T \rangle \underline{f} - 2 \langle \underline{\alpha}, g \rangle \qquad [2.5]$$

Since K is positive-definite (*i.e.*, $< Kf, f > > 0$), then $\underline{f}$ is a minimizing sequence that converges in *energy* to a minimum of F. The resulting system of Rayleigh-Ritz equations are obtained by enforcing stationarity of [2.5], thus

$$< \underline{\alpha}, K\underline{\alpha}^T > \underline{f} = < \underline{\alpha}, g > \qquad [2.6]$$

A direct application of Galerkin's method to [1.9] is seen to produce [2.6].

In the event that K is complex and non-self-adjoint (as in the Helmholtz wave operator), the same equivalence as above is shown to exist (Jeng & Wexler, 1978). Hence, the use of [2.6] is not restricted to the conditions of its derivation. From an application standpoint, it is easier to apply Galerkin's method directly rather than follow through with the preceeding derivation which would require definition of a scalar energy product of the form $< \bar{J} \cdot \bar{E} >$ or $< \bar{J} \cdot \bar{H} >$, recognised as a *reaction* or coupling between the source and the field (Thiele, 1973). In fact, Galerkin's method can also be applied when no variational principle is available (Stakgold, 1967).

The proof of convergence for Fredholm integral equations exists if [1.2] and [1.3] are augmented by f having a finite norm (as in [1.3]). Application of the Bubnov-Galerkin method (which is a generalization of the Rayleigh-Ritz method), which requires the expression $Kf - g = 0$ to be orthogonal to the set of coordinate functions α_n, will result in convergence in the *mean* (Mikhlin, 1964).

2.2 Parametric Representation of Surfaces and Sources

The BEM is capable of addressing both two- and three-dimensional field problems. As such, two sets of modelling strategies exist and should be discussed in parallel although they originated from the same basic philosophy. Boundary surfaces (or contours in two-dimensions) are represented parametrically by triangular (or line) elements which are referred to the standard element in *local* $\zeta - \eta$ (or ζ) space. Sub-domain expansion functions α_i are defined in *local* coordinates for intra-element interpolation of node-point values. The set α_i take on values

$$\alpha_i = \begin{cases} 1 & \text{at node } i \\ 0 & \text{at all other nodes} \end{cases} \qquad [2.7]$$

with i running over designated node numbers according to a *local* node numbering scheme (Figures 2.2 and 2.4). At all other locations within the simplex, the set of α_i's sum to unity. The functions defined by [2.7] originated from the use of Lagrange interpolation (Wexler, 1980). Beginning with the linear $(n = 1)$ interpolants: L_1, L_2 and L_3; expansion functions for higher degrees of approximation $(n > 1)$ are generated from their product forms subject to the constraint [2.7]. Tables 2.1 and 2.2 show the expressions for α_i for two- and three-dimensional applications, respectively. The degree n of approximation is related to the number m of interpolation nodes so that the two-dimensional expression is

$$m = n + 1 \qquad [2.8]$$

The corresponding relation in three-dimensions is

$$m = \frac{1}{2}(n + 1)(n + 2) \qquad [2.9]$$

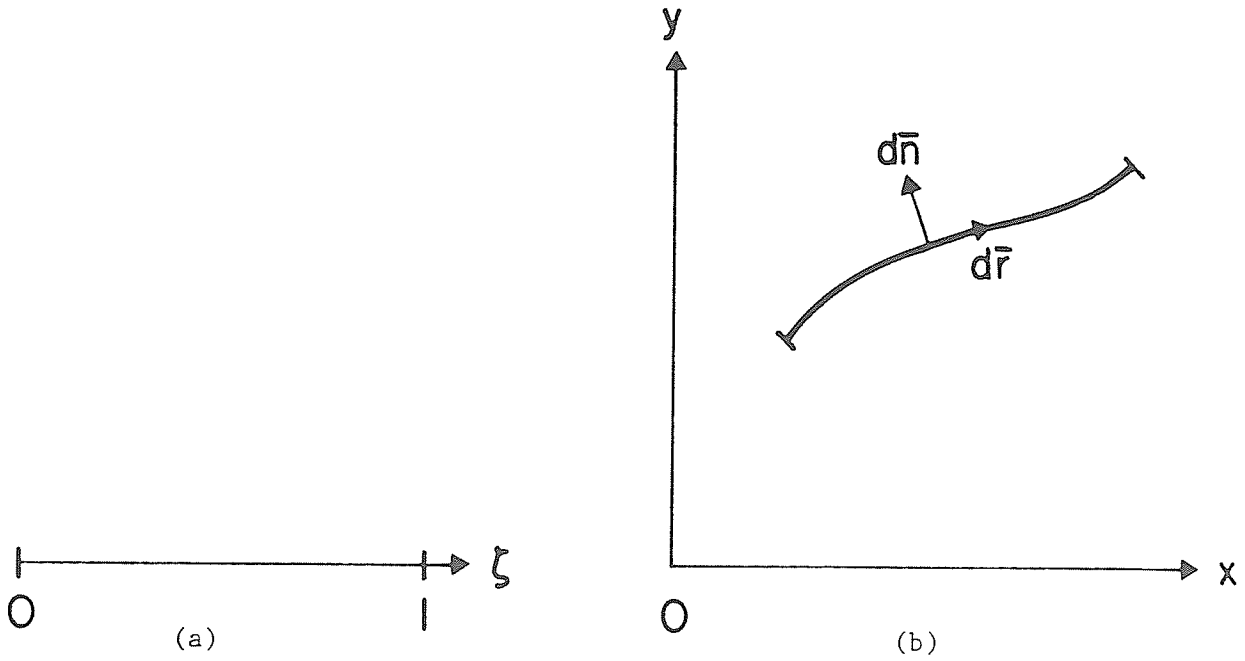

Fig. 2.1: The 1-dimensinal simplex
(a) *local* ζ space; and
(b) *global* x-y plane

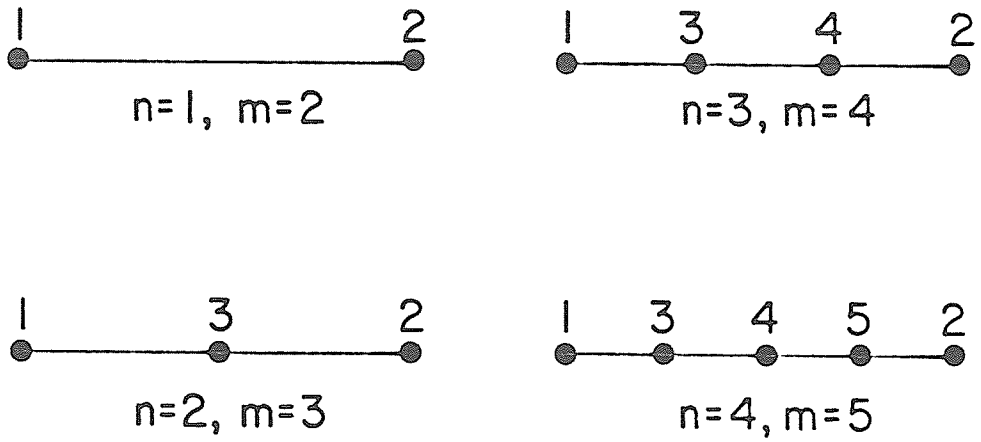

FIG. 2.2: Local node numbering scheme for 1-dimensional simplex

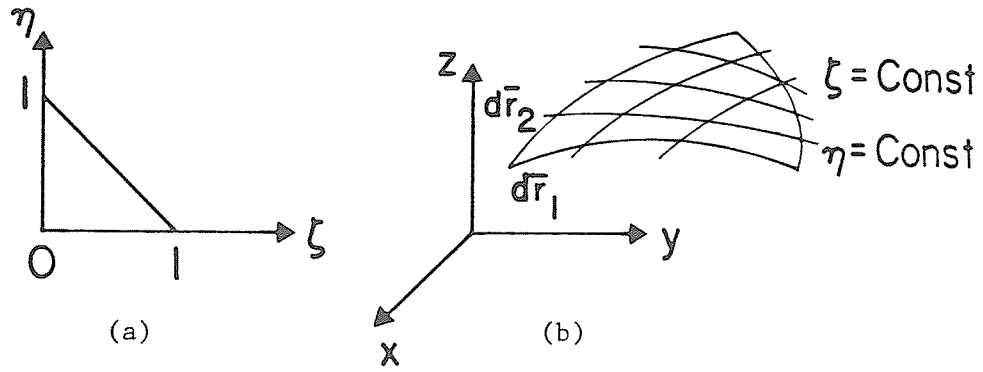

FIG. 2.3: The 2-dimensional simplex
(a) *local* ζ-η space; and
(b) *global* x-y-z space

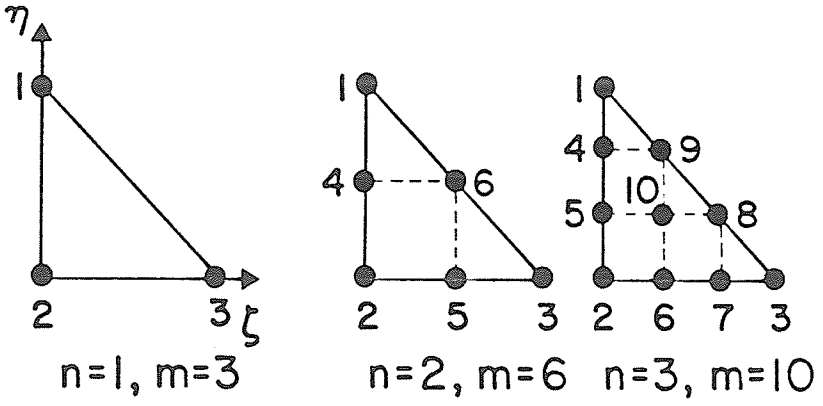

FIG. 2.4: Local node numbering scheme for 2-dimensional simplex

TABLE 2.1: Expansion functions $\alpha_i(\zeta)$

$L_1 = 1 - \zeta$; $L_2 = \zeta$

i	n = 1	n = 2	n = 3	n = 4
1	L_1	$L_1(2L_1 - 1)$	$\frac{1}{2} L_1(3L_1 - 1)(3L_1 - 2)$	$\frac{1}{6} L_1(4L_1 - 1)(4L_1 - 2)(4L_1 - 3)$
2	L_2	$L_2(2L_2 - 1)$	$\frac{1}{2} L_2(3L_2 - 1)(3L_2 - 2)$	$\frac{1}{6} L_2(4L_2 - 1)(4L_2 - 2)(4L_2 - 3)$
3		$4L_1L_2$	$\frac{9}{2} L_1L_2(3L_1 - 1)$	$\frac{8}{3} L_1L_2(4L_1 - 1)(4L_1 - 2)$
4			$\frac{9}{2} L_2L_1(3L_2 - 1)$	$4 L_1L_2(4L_1 - 1)(4L_2 - 1)$
5				$\frac{8}{3} L_2L_1(4L_2 - 1)(4L_2 - 2)$

TABLE 2.2: Expansion functions $\alpha_i(\zeta, \eta)$

$L_1 = \eta$; $L_2 = 1 - \zeta - \eta$; $L_3 = \zeta$

i	n = 1	n = 2	n = 3
1	L_1	$L_1(2L_1 - 1)$	$\frac{1}{2} L_1(3L_1 - 1)(3L_1 - 2)$
2	L_2	$L_2(2L_2 - 1)$	$\frac{1}{2} L_2(3L_2 - 1)(3L_2 - 2)$
3	L_3	$L_3(2L_3 - 1)$	$\frac{1}{2} L_3(3L_3 - 1)(3L_3 - 2)$
4		$4L_1L_2$	$\frac{9}{2} L_1L_2(3L_1 - 1)$
5		$4L_2L_3$	$\frac{9}{2} L_1L_2(3L_2 - 1)$
6		$4L_3L_1$	$\frac{9}{2} L_2L_3(3L_2 - 1)$
7			$\frac{9}{2} L_2L_3(3L_3 - 1)$
8			$\frac{9}{2} L_3L_1(3L_3 - 1)$
9			$\frac{9}{2} L_3L_1(3L_1 - 1)$
10			$27L_1L_2L_3$

where the m represents the number of bivariate polynomial coefficients a_i for the specified degree n. For example, the $n = 2$ bivariate polynomial representation for the independent variable f resembles

$$f(\zeta, \eta) = a_0 + a_1\zeta + a_2\eta + a_3\zeta^2 + a_4\zeta\eta + a_5\eta^2 \qquad [2.10]$$

One could proceed to enforce [2.10] at the indicated node positions in Figure 2.4 to obtain

$$\underline{f} = A\,\underline{a} \qquad [2.11]$$

where the column vector of f are the node-point values. Inversion of A would result in

$$\underline{a} = A^{-1}\,\underline{f} \qquad [2.12]$$

when the $\underline{a}$ can be individually expanded and substituted into [2.10]. A subsequent rearrangement would result in the form

$$f(\zeta, \eta) = \underline{\alpha}^T\underline{f} \qquad [2.13]$$

where

$$\underline{\alpha}^T = [1\ \zeta\ \eta\ \zeta^2\ \zeta\eta\ \eta^2]\,A^{-1} \qquad [2.14]$$

is as derived from Lagrange interpolation considerations. Equations [2.10] to [2.14] are only meant for illustration since expansion functions α_i are not generated in this manner because matrix A is of Vandermondé type and is unstable to invert.

Global positions (x, y, z) may now be expressed in terms of vertex node coordinates as

$$x = \sum_{i=1}^{m} \alpha_i(\zeta, \eta)\, x_i \quad ; \quad y = \sum_{i=1}^{m} \alpha_i(\zeta, \eta)\, y_i \quad ;$$

$$z = \sum_{i=1}^{m} \alpha_i(\zeta, \eta)\, z_i \qquad [2.15]$$

For the two-dimensional case, the z spatial dependence of α_i should be dropped. Each element in *global* space is the result of a mapping from the simplex. The Jacobian that defines this mapping is obtained from an expression for the differential area (or length). Figures 2.1 and 2.3 show the respective simplexes and their transformed positions. Differential changes in position due to corresponding changes within the simplex for the three-dimensional case results in

$$d\bar{r}_1(\zeta) = \frac{\partial x}{\partial \zeta} d\zeta\, \hat{i} + \frac{\partial y}{\partial \zeta} d\zeta\, \hat{j} + \frac{\partial z}{\partial \zeta} d\zeta\, \hat{k} \qquad [2.16]$$

and

$$d\bar{r}_2(\eta) = \frac{\partial x}{\partial \eta} d\eta\, \hat{i} + \frac{\partial y}{\partial \eta} d\eta\, \hat{j} + \frac{\partial z}{\partial \eta} d\eta\, \hat{k} \qquad [2.17]$$

so that the differential area on the parametric surface is given by

$$d\bar{s} = d\bar{r}_1 \times d\bar{r}_2 \qquad [2.18]$$

The Jacobian is then calculated from the preceeding equations as

$$J = \sqrt{M_{31}^2 + M_{32}^2 + M_{33}^2} \qquad [2.19]$$

where M_{ij} are the minors of

$$A_{ij} = \begin{bmatrix} \frac{\partial x}{\partial \zeta} & \frac{\partial y}{\partial \zeta} & \frac{\partial z}{\partial \zeta} \\ \frac{\partial x}{\partial \eta} & \frac{\partial y}{\partial \eta} & \frac{\partial z}{\partial \eta} \\ 1 & 1 & 1 \end{bmatrix} \qquad [2.20]$$

taken along the bottom row. In two-dimensions, the incremental vector in the x-y plane is

$$d\bar{r} = \frac{\partial x}{\partial \zeta} d\zeta \, \hat{i} + \frac{\partial y}{\partial \zeta} d\zeta \, \hat{j} \qquad [2.21]$$

with incremental length equal to the Jacobian, or

$$J = \sqrt{(\frac{\partial x}{\partial \zeta})^2 + (\frac{\partial y}{\partial \zeta})^2} \qquad [2.22]$$

2.3 Logistics of Matrix Fill

Equation [2.6] is restated in integral form over a surface as

$$\int \underline{\alpha}(s) \int k[s|s'] \, \underline{\alpha}^T(s') ds' ds \, \underline{f} = \int \underline{\alpha}(s) g \, ds \qquad [2.23]$$

to better appreciate the mechanism of evaluation of matrix entries. The left-hand side of [2.23] involves a double surface integral with the inner portion running over source coordinates. Remembering that the underlining bar denotes column vector, this term produces a square matrix S. Denoting the right-hand side term as $\underline{b}$, [2.23] can now be written in a more easily recognised form as

$$S \, \underline{f} = \underline{b} \qquad [2.24]$$

where S is commonly called the system matrix, $\underline{b}$ the excitation, and $\underline{f}$ the response.

In the BEM, Gauss quadratures generated from the product rule are used for integration. The quadrature data is defined over the standard simplex with sampling locations mapped into the *global* frame only for the explicit purpose of evaluating the kernel $k[s|s']$. Otherwise, all integrations are performed on the simplex thus eliminating the need for local operations on each element. Matrix accumulation is carried out on a *per element* basis so that the order of each subsystem matrix is m (from Section 2.2). The kernel is non-singular provided $s \neq s'$, *i.e.*, accumulation is not affected on the *self-element*. Hence, no special treatment is accorded this operation. For the case $s = s'$, Green's function singularity is reflected in the numerical algorithm as division by zero as the quadrature points coincide. McDonald (1975) and Jeng (1977) used an *addition-subtraction* technique whereby the kernel is re-written as the summation of two terms — one, a regularised form of the original kernel which is handled numerically, and the other, an extracted singularity which can be analytically integrated. Lean *et al* (1979b) improved on the technique by taking into account the limit of the first form as $s \rightarrow s'$, a step which was neglected by the two previous researchers probably due to an oversight. Specifically, the mean value theorem is invoked to allow s' to be expressed as

$$s' = s + \delta \qquad [2.25]$$

where δ represents an infinitesimal spatial shift along either the ζ or η directions, and

$$\frac{\alpha(s + \delta) - \alpha(s)}{\delta} \cong \left.\frac{\partial \alpha}{\partial s}\right|_{s,s'} \qquad [2.26]$$

In the limit as $s \to s'$, the form of the three-dimensional free-space Green's function $(4\pi\delta)^{-1}$ when used with the result of [2.26] produces the finite quantity

$$\int \frac{1}{4\pi} \frac{\partial \alpha}{\partial s}\bigg|_{s,s'} ds' \qquad [2.27]$$

as contribution.

Although this scheme is exact for flat surfaces, it requires care and deliberation for the manual (analytic) portion of the procedure. Also, the expressions so derived are dependent on the specific kernel treated. For curved surface application, the element is divided into a number of flattened inscribed sections over which the procedure is individually applied. From an engineering standpoint, this fragmentation scheme is intuitively acceptable and should improve the quality of results. Mathematically however, the question of convergence, if any, has yet to be answered. A novel method of confronting this problem is the subject of the next Chapter.

III. TREATMENT OF KERNEL SINGULARITIES

The main difficulty encountered in integral equation solution lies in the numerical approximation to the integration process for singular kernels. This singularity is a direct consequence of Green's function when $\bar{r} = \bar{r}'$, *i.e.*, where the observer and source locations coincide. In avoiding this difficulty by merely ignoring the discontinuity (*e.g.*, Oshiro & Su, 1965), matrix conditioning generally deteriorates due to a loss in diagonal strength. The use of a dodge whereby the integration is performed to within the near vicinity of the singularity, is ineffectual (Acton, 1970) compared to the algorithmic improvisations required. Furthermore, the effect of the singularity becomes increasingly pronounced as $\bar{r} \to \bar{r}'$ so that artificial truncation of the interval lacks in mathematical substantiation and finesse.

Conventional methods of addressing this crucial issue include complex variable transforms, analytic integration over *flat* intervals (Jeng, 1977), and the evaluation of Cauchy principal values (Lachat & Watson, 1976). Being analytic, these techniques are unavoidably problem geometry dependent, thus restricting their widespread application. With few exceptions, their usage entails tedious manipulations that contribute to both core length and overhead. Traditional ideas have shied away from a totally numerical approach and in fact have suggested low-order trapezoidal and Romberg rules as alternatives (Poggio & Miller, 1973) mainly because of the expected prohibitive cost of integration. The reason for this adverse reaction is clear if we consider the indiscriminate use of the Gauss-Legendre quadrature of weight function unity which is designed for the integration of regular functions. Theoretically,

this would require an infinite number of sampling points for acceptable precision. Also, for optimal solution compatibility, it is difficult to justify the use of a high-order integration scheme when collocation involves constant pulse patches. With the advent of high-order schemes, the numerical alternative should be viable, especially when Gauss quadratures can be tailored to obtain optimal precision with minimal sampling. Such a scheme will be discussed in the following subsection.

Field discontinuities due to geometry — edges or corners — where source densities go rapidly to infinity, is of secondary importance with respect to integral equation solution. However, the proper modelling of this behaviour will accelerate convergence besides improving the precision of computed near-field quantities. From an algorithmic standpoint, this measure will introduce another singularity into the kernel for elements adjacent to a re-entrant corner. The manner in which the BEM algorithm addresses this problem will be discussed at length in subsequent subsections.

3.1 Numerical Integration with Gauss Quadratures

The numerical approximation to a definite (or indefinite) integral takes the form

$$\int_a^b w(x)\, f(x)\, dx \cong \sum_{i=0}^{n} A_i\, f(x_i) \qquad [3.1]$$

where the choice of weight function $w(x)$ specifies a unique polynomial sequence defined by

$$P_n(x) = x^n + a_{n-1}\, x^{n-1} + ... + a_1 x + a_0 \qquad [3.2]$$

that satisfies the orthogonality condition

$$\int_a^b w(x)\, P_n(x)\, P_\ell(x)\, dx = 0 \quad ; \quad n \neq \ell \ , \ n > \ell \qquad [3.3]$$

Provided $w(x) \geq 0$ in the interval $[a, b]$, the roots of $P_n(x)$ are real and are the sampling locations x_i with corresponding weight coefficients A_i. The derivation of orthogonal polynomials may be carried out in a straightforward fashion. Consider the independent set

$$U_i = \{1, x, x^2, \ldots . x^{m-1}, x^m\} \qquad [3.4]$$

The quadrature formula has degree of precision or exactness m if it is exact whenever $f(x)$ in [3.1] is a polynomial of degree $\leq m$; and is not exact for $f(x) = x^{m+1}$ (Stroud & Secrest, 1966). Then n points and coefficients may be found to make [3.1] exact for all polynomials of degree $\leq 2n - 1$. From the independent set U_i, a set of orthogonal polynomials V_i is generated through the use of the Gram-Schmidt orthogonalization procedure where the qth polynomial is given by

$$V_q = U_q - \sum_{i=1}^{q-1} \frac{< V_i, U_q >}{< V_i, V_i >} V_i \qquad [3.5]$$

and inner product (or projection) is defined by

$$< V_i, U_q > = \int_a^b w(x)\, V_i\, U_q\, dx \qquad [3.6]$$

Orthogonal polynomials most frequently encountered include the Gauss-Legendre, Gauss-Chebyschev, Gauss-Hermite and Gauss-Laguerre types. Aside from the last two, the others belong to a broader classification — the Gauss-Jacobi family. The general expression for $w(x)$ is

$$w(x) = (1 - x)^\alpha (1 + x)^\beta \quad ; \quad \alpha, \beta > -1 \qquad [3.7]$$

where the choice $\alpha = \beta = 0$ identifies the Gauss-Legendre weight of $w(x) = 1$; and $\alpha = \beta = -\frac{1}{2}$, the Gauss-Chebyschev (first kind) weight of $w(x) = (1 - x^2)^{-\frac{1}{2}}$. This generalization of the weight is a definite advantage towards the systematic generation of quadrature formulas on an automatic basis.

The preponderance of weight functions as exemplified by the general nature of [3.7] has to signify specializations of quadrature forms to some degree. Undoubtedly, the use of certain weight functions may be preferred for certain integrands. This fact suggests that some guidelines should be established to help in the selection of an optimal quadrature scheme given a particular integrand. To begin with, one may broadly classify weight functions into two categories: the types that are regular in [a, b]; and those singular at end-points a and/or b. Returning to equation [3.1], the integrand can collectively be expressed as

$$F(x) = w(x)\, f(x) \qquad [3.8]$$

where $F(x)$ is the actual function to be integrated and $f(x)$, the modified form depending on the choice of $w(x)$. In the event $F(x)$ is inherently singular in [a, b], $w(x)$ ideally can be chosen to contain the form of the discontinuity thus leaving $f(x)$ to be regular. Figures 3.1, 3.2 and 3.3 illustrate the relative precision attainable for three different integrands using quadrature data generated from a few selections for weight functions. In particular, Figure 3.1 involves the integration of a logarithmic function identical to that of the two-dimensional Poisson Green's function. Figure 3.2 concerns a function that behaves as $r^{-\frac{1}{2}}$ at one end-point — identical to the edge singularity of a corner with a re-entrant angle of 2π. From a closer inspection, the following

inferences may be made:

(i) Depending on the form of $F(x)$, $w(x)$ should be chosen such that $f(x)$ remains regular in $[a, b]$ to obtain best accuracy with minimum sampling. Ideally, if $w(x)$ can be chosen to equal $F(x)$, then $f(x)$ would be independent of sampling location and the integration procedure is reduced to a summation of weights A_i thus eliminating one source of error.

(ii) If $F(x)$ is singular at one or both end-points, then $w(x)$ should be selected to contain the form of the singularity thus leaving $f(x)$ regular or at least more weakly singular. By extension, the case when $F(x)$ is singular within the region of integration can be handled by subsectioning followed by two repetitive applications of the quadrature whilst retaining the form of the singularity in each transformation.

(iii) Besides the general guidelines laid out in (i) and (ii), the form of $F(x)$ and $f(x)$ should always be visually checked for compatibility. In general, $f(x)$ should always be a *better* function to work with than $F(x)$. Figure 3.3 shows the degradation of results due to the unfortunate choice of $w(x) = 1 - x$ for $F(x) = 1$ thus fixing $f(x) = (1 - x)^{-1}$, a form worse off than $F(x)$.

(iv) In subsequent applications, the integrand $F(x)$ will include the Jacobian of transformation arising from any physical departure from the region over which the quadrature was defined. This alteration adds another degree of flexibility to the optimal selection of $w(x)$.

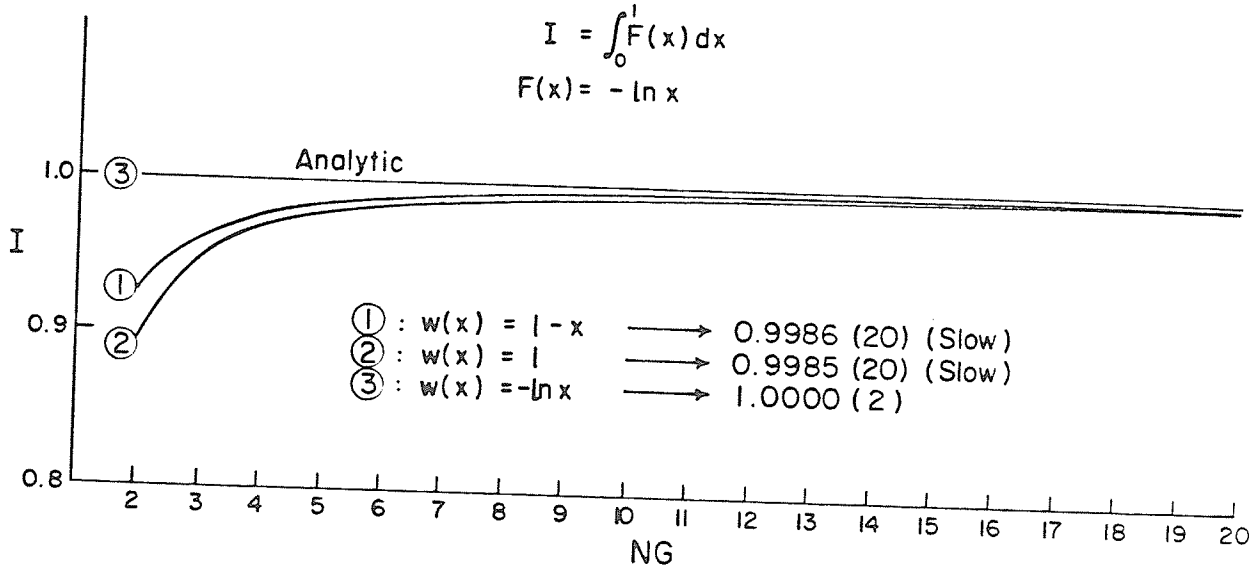

FIG. 3.1: Numerical integration of logarithmic singularity

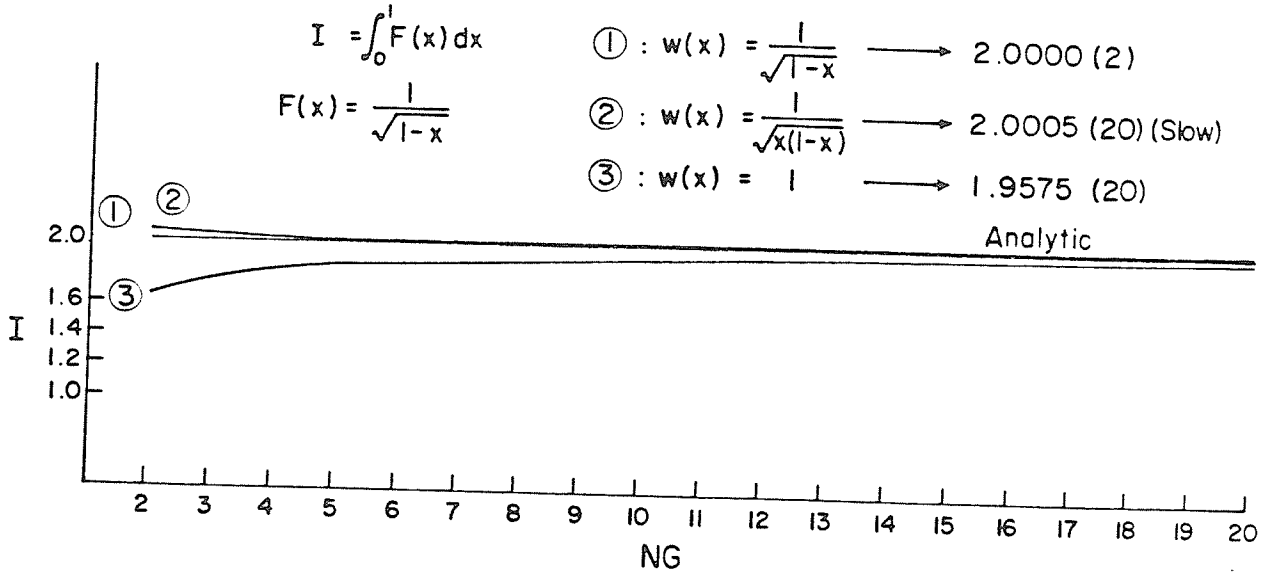

FIG. 3.2: Numerical integration of $r^{-1/2}$ singularity

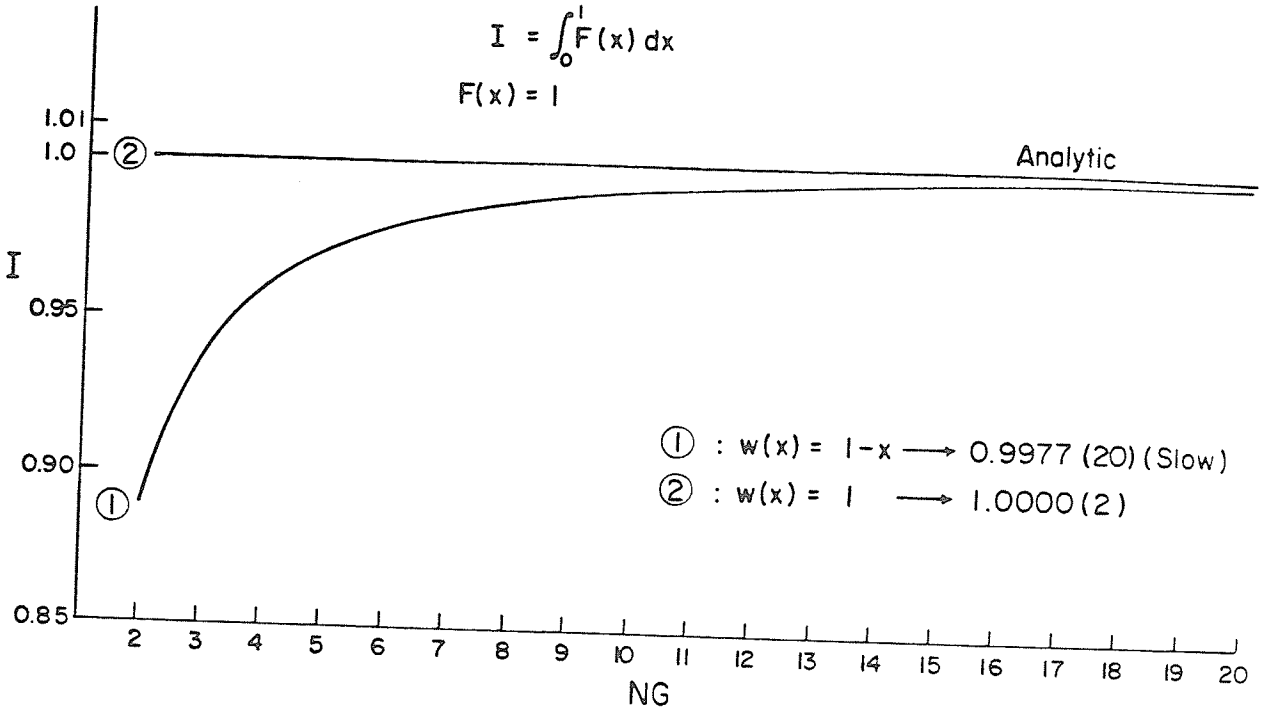

FIG. 3.3: Numerical integration of a regular function

3.2 Implementation for Green's Function Singularity

Singularities of Green's functions for static fields in two- and three-dimensions (logarithmic and r^{-1} behaviour), are treated by essentially the same sectioning philosophy. Denote the inner integral on the left-hand side of [2.23] as $H(s)$ so that the system matrix is given by

$$S = \int \underline{\alpha}(s)\, H(s)\, ds \qquad [3.9]$$

and $H(s)$ by

$$H(s) = \int k[s|s']\, \underline{\alpha}^T(s')\, ds' \qquad [3.10]$$

The Gauss-Legendre quadrature is selected for integration over the unprimed

variable. For accumulations of S other than on the *self-element*, $H(s)$ is regular and the same quadrature scheme is used for integration over the primed variable as well. Over the *self-element* the appropriate sectioning procedure applies.

3.2.1 Two-Dimensional Scheme

The *self-element* is sectioned into two about the singular location p_1 which is a collocation point of the outer (unprimed) integral in *local* ζ space (Figure 3.4). Since the form of the kernel singularity is logarithmic, a quadrature scheme with weight $w(\zeta) = -\ell n\zeta$ is chosen for this application based on the guidelines established in the previous section. The quadrature data thus generated is then operated on by two linear transformations T_1 and T_2, subject to the constraint that the behaviour of the weight function be preserved. Transformations T_1 and T_2 are given by

$$T_1 : m_1 = (1 - p_1)\zeta + p_1 \quad ; \quad m_1 \varepsilon [p_1, 1] \qquad [3.11]$$

and

$$T_2 : m_2 = p_1(1 - \zeta) \quad ; \quad m_2 \varepsilon [0, p_1] \qquad [3.12]$$

and in effect, they position the quadrature so that p_1 is approached on both sides logarithmically. The intervals $[0, p_1]$ and $[p_1, 1]$ spanned by m_2 and m_1, respectively, are then reassembled as shown in Figure 3.4 where the net result is the construction of a special set of quadrature data that will integrate a logarithmic singularity at p_1. The condition that the logarithmic form be retained in the limit of approaching p_1 is easily verified by observing the weighting functions

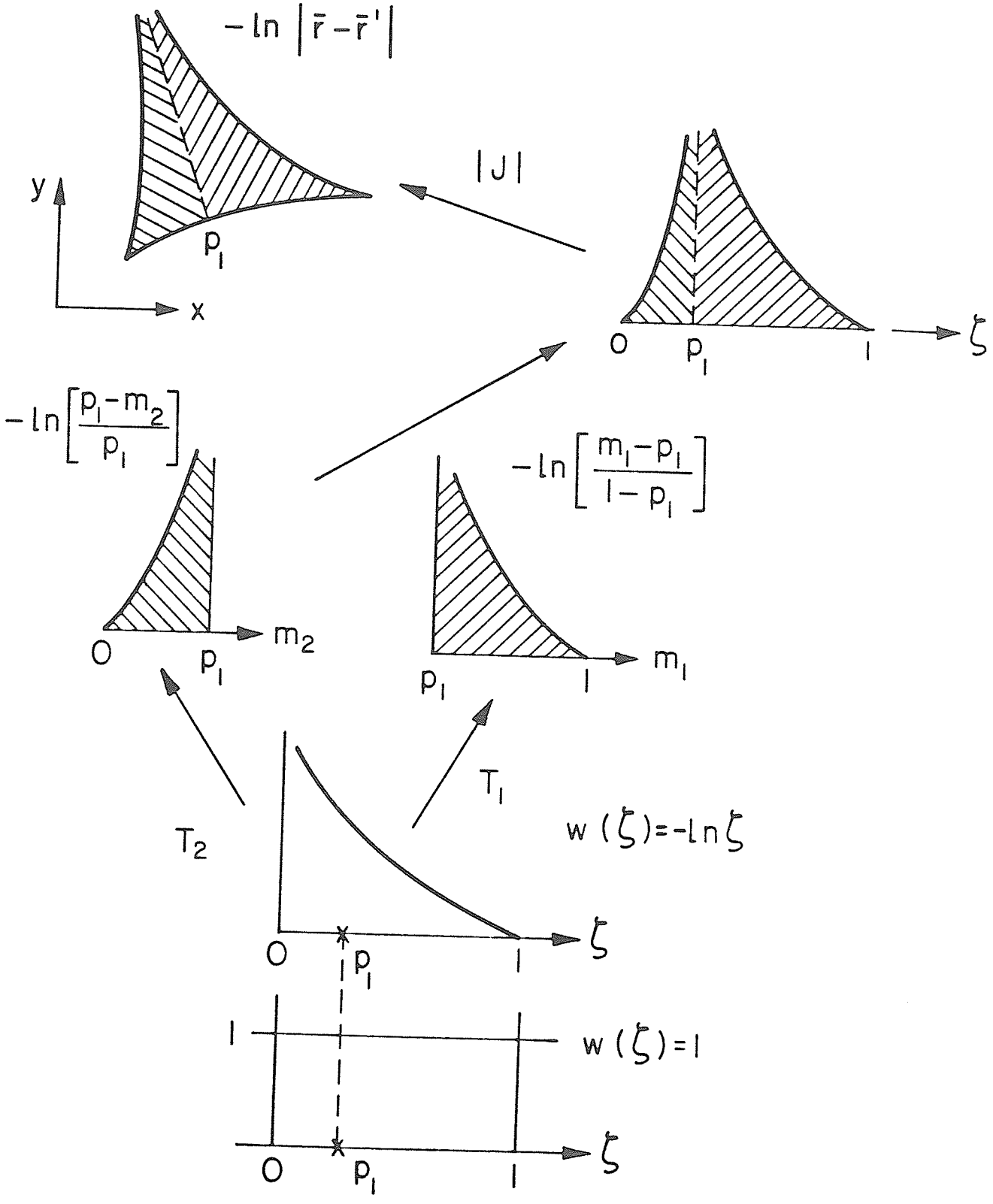

FIG. 3.4: BEM sectioning scheme for logarithmic singularity

$$w(m_1) = -\ell n \left[\frac{m_1 - p_1}{1 - p_1}\right] \qquad [3.13]$$

and

$$w(m_2) = -\ell n \left[\frac{p_1 - m_2}{p_1}\right] \qquad [3.14]$$

A consequence of the transformations is that the quadrature weights are now scaled by the factors $(1 - p_1)$ and p_1 $(0 < p_1 < 1)$ for T_1 and T_2, respectively.

The explicit expression for the kernel of [3.10] is $-\frac{1}{2\pi} \ell n|s - s'|$ assuming the integral operator is bounded. In the nomenclature of the preceeding section, $F(s')$ is now given by

$$F(s') = \underline{\alpha}^T(s') \left[-\frac{1}{2\pi} \ell n|s - s'|\right] \qquad [3.15]$$

so that for $m_1 \varepsilon [p_1, 1]$, the integrand is

$$f_1(s') = \frac{1}{w(m_1)} F(s') \qquad [3.16]$$

and for $m_2 \varepsilon [0, p_1]$,

$$f_2(s') = \frac{1}{w(m_2)} F(s') \qquad [3.17]$$

with the understanding that expansion functions α are evaluated at the transformed positions m_1 and m_2, and weights $w(m_1)$ and $w(m_2)$ given in [3.13] and [3.14] are evaluated at the same location. No mathematical cancellation is performed; rather $f_1(s')$ and $f_2(s')$ are *regularised* in the sense that both numerator and denominator have the same limiting behaviour. The disposition of the sampling positions generated from this particular weight function takes into account the expected singular behaviour.

The inherent merit of this scheme is that it is defined on the simplex so that the form of the singularity is preserved regardless of the actual size or shape of the *global* element. The built-in transformations T_1 and T_2 guarantee this invariance. Another point to be stressed is that good precision is usually attained with lower orders of quadrature than that for the unprimed variable. From experience, the optimal order is approximately given by

$$n_s = \frac{1}{2} n_g + 1 \qquad [3.18]$$

where n_g is the order for the Gauss-Legendre quadrature prescribed for the unprimed variable.

The corresponding time-harmonic Green's function is a Hankel function of zero order and second kind ($e^{j\omega t}$ time-dependence) which has the same logarithmic singularity of the imaginary component for vanishing arguments. To integrate this kernel, the same sectioning philosophy is applied. However, the argument is multiplied by the wave number k so that in using the polynomial expansions of Abramovitz & Stegun (1968), a frequency criteria is necessary. Gauss quadrature with weight function $w(\zeta) = -\ell n\zeta$ is used only when $k_t > 3$ where k_t is the transverse component of wave number. Otherwise, the Gauss-Legendre quadrature is applied. This measure ensures that the Hankel function expansion for small arguments ($k_t r > 3$) when used, will confine r within the interval $[0, 1]$ within which $w(\zeta)$ is defined.

Normal derivatives of the above functions are relatively well-behaved since the cosine of the angle included by outward normal $\hat{n}$, and spatial vector $(\bar{r} - \bar{r}')$ vanishes as $s \to s'$. This situation is

reminiscent of the discussion of [3.16] and [3.17]. Hence, the quadrature specified by $w(\zeta) = 1$ is appropriate. Even in this application, the sectioning methodology is effective in that the quadratures are oriented in the proper directions, *i.e.*, approaching p_1 in the prescribed manner.

3.2.2 Three-Dimensional Scheme

The success of the three-dimensional scheme is dependent on a Jacobian of transformation to provide the moderating effect for the r^{-1} singularity. Gauss quadrature for surface integration is conveniently generated by an application of the product rule. Consider the expression

$$\int_0^1 \int_0^1 w(x_1)\, w(x_2)\, f\, dx_1 dx_2 \qquad [3.19]$$

which represents the integration of a function f with quadrature generated from product forms of the one-dimensional rules defined on $[0, 1]$. Applying a transformation

$$\begin{aligned} \zeta &= x_1 \\ \eta &= x_2(1 - x_1) \end{aligned} \qquad [3.20]$$

to [3.19], and choosing $w(x_1) = w(x_2) = 1$ results in

$$\int_0^1 \int_0^{1-\zeta} f\, \frac{1}{(1 - \zeta)}\, d\eta d\zeta \qquad [3.21]$$

From [3.21] and [3.19], the integration of a function f on the simplex is given by

$$\int_0^1 \int_0^{1-\zeta} f\, d\eta d\zeta = \int_0^1 \int_0^1 f\, [1 - \zeta]\, dx_1 dx_2 \qquad [3.22]$$

where $[1 - \zeta]$ is the Jacobian of transformation. The vertex of $\zeta = 1$ is formed by collapsing the right edge of the unit-square over which the product rule is generated. As a consequence, the sampling positions within the simplex appear to be *fanning* from this vertex. The term $[1 - \zeta]$ vanishes as $\zeta \to 1$, a property that may be used to advantage.

Since the free-space Green's function has r^{-1} behaviour, the limiting effect of the Jacobian could be used as a moderating influence if the *fanning* point is aligned with the point at which r vanishes. Figure 3.5 shows a flat triangular element in space over which is simulated a function with r^{-1} singularity at the third vertex. The precision obtained using three sets of test rules are compared against the analytically obtained value of 1.177 in Figure 3.6. Test rules 1 and 2 correspond to Jeng (1977), and that advocated in [3.22], respectively. Comparing the number of sampling points (400 to 9) to obtain two-decimal precision, the superiority of the present technique is unquestionable. Test rule 3 is obtained from Stroud & Secrest (1966) and included as a matter of interest. As expected, it produces results intermediate between those of 1 and 2. The orientation dependence of this technique is verified in Figure 3.7.

The success of this technique is wholly dependent on the triangular geometry of the simplex. As sampling points are interior to it, three triangular subsections sharing a common *fanning* vertex at $(\zeta, \eta) \equiv (p, q)$ have to be addressed. The Gauss-Legendre quadrature scheme generated over the simplex, is mapped into each subsection by the transformations

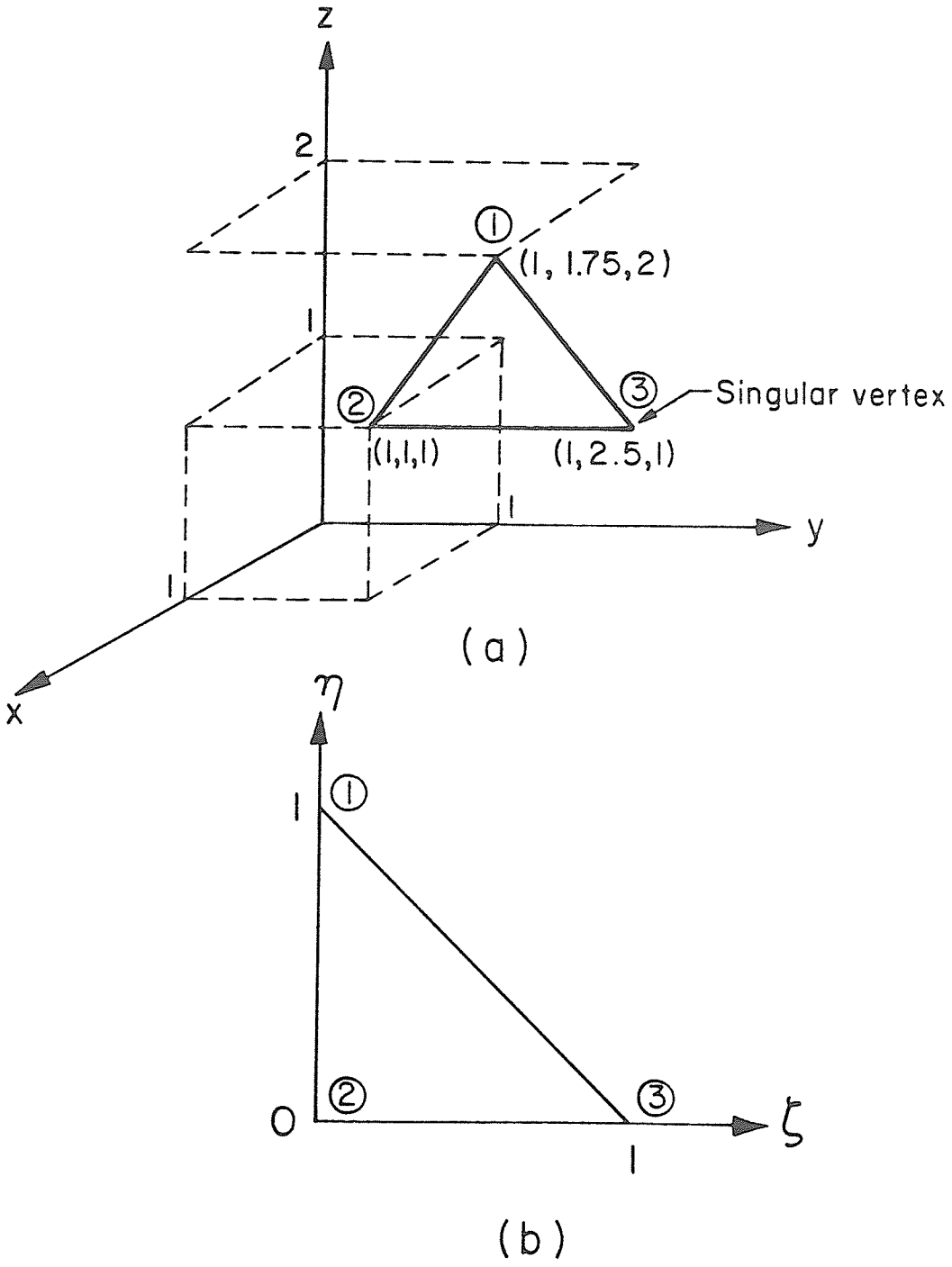

FIG. 3.5: The boundary element singular at vertex #3
(a) in *global* x-y-z space, and
(b) in *local* ζ-η space

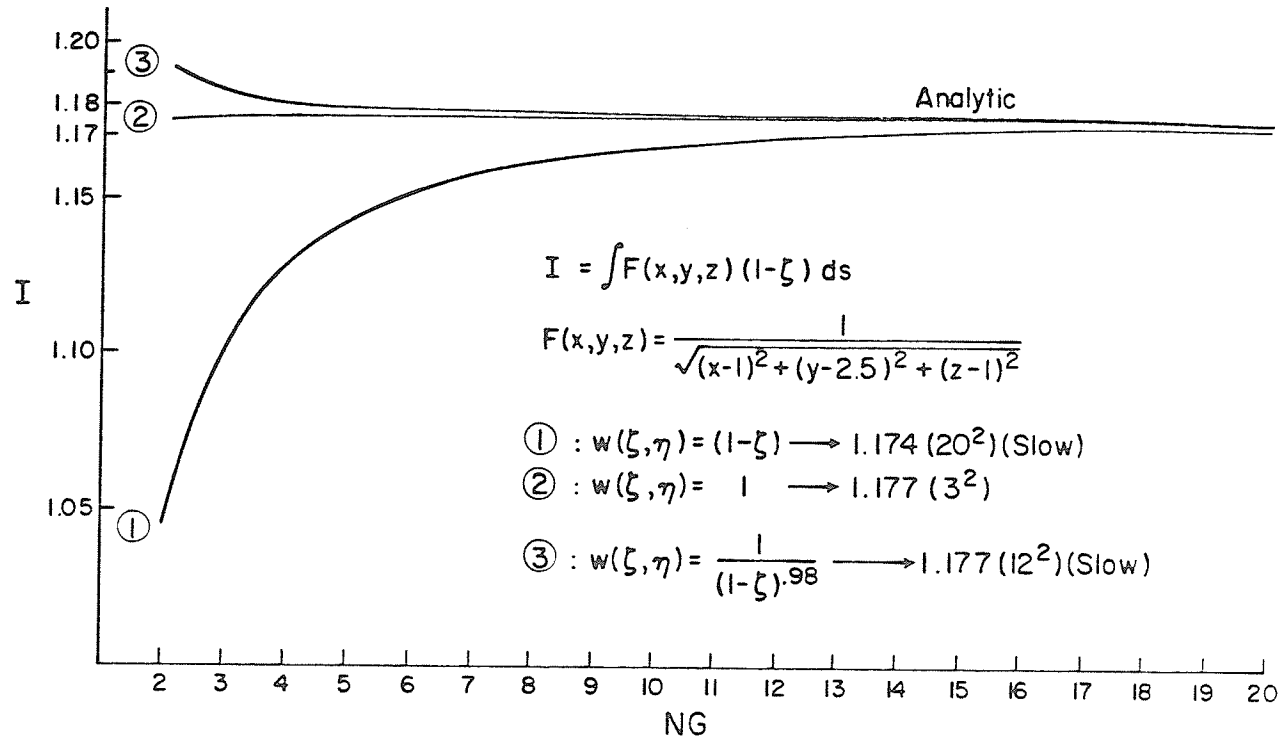

FIG. 3.6: Numerical integration of r^{-1} singularity

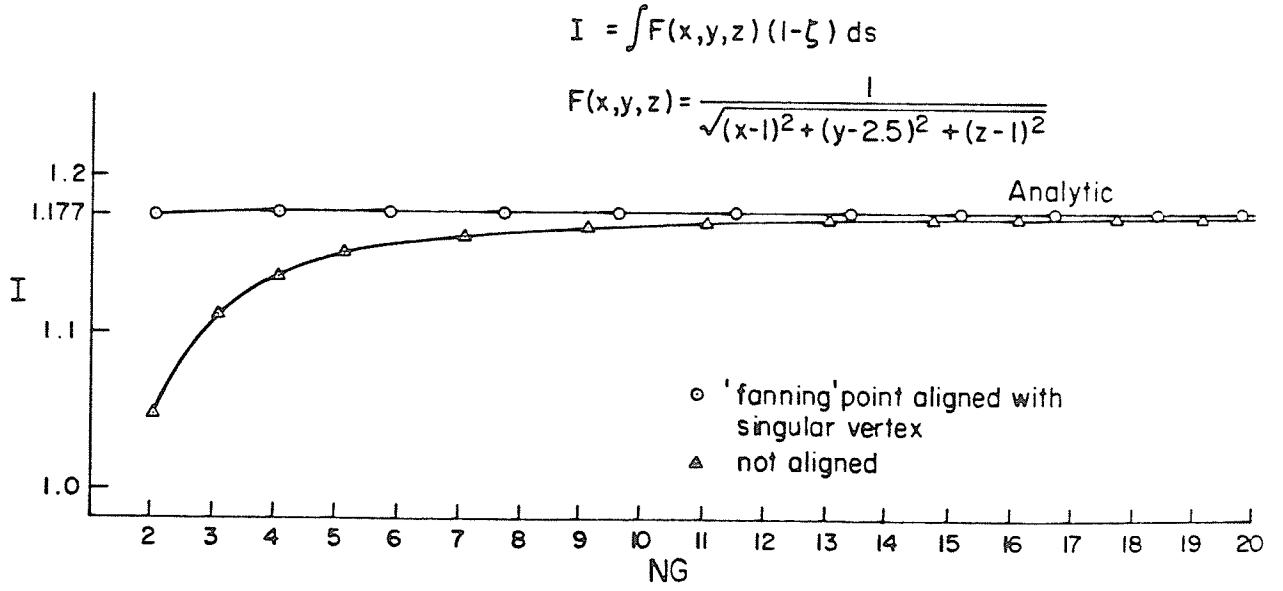

FIG. 3.7: Orientation dependence of quadrature scheme

$$T_1: \quad \eta_1 = \eta + q\zeta \qquad \zeta_1 = p\zeta \qquad [3.23]$$

$$T_2: \quad \eta_2 = q\zeta \qquad \zeta_2 = \zeta(p - 1) - \eta + 1 \qquad [3.24]$$

and

$$T_3: \quad \eta_3 = \zeta(q - 1) - \eta + 1 \qquad \zeta_3 = \eta + p\zeta \qquad [3.25]$$

which ensures that vertex (p, q) is the *fanning* location. The weights A_i are now scaled by p, q and (1 - p - q), respectively where $0 \leq p, q \leq 1$. The explicit expression for F(s') is now

$$F(s') = \underline{\alpha}^T(s') \frac{1}{4\pi|s - s'|} \qquad [3.26]$$

so that the integrand for the region tranformed by [3.23] is given as

$$f_1(s') = F(s') \left[1 - \frac{\zeta_1}{p}\right] \qquad [3.27]$$

that by [3.24] as

$$f_2(s') = F(s') \left[1 - \frac{\eta_2}{q}\right] \qquad [3.28]$$

and that by [3.25] as

$$f_3(s') = F(s') \left[\frac{(\zeta_3 + \eta_3) - (p + q)}{1 - (p + q)}\right] \qquad [3.29]$$

The general statements of the previous subsection are equally valid in this discussion. Figure 3.8 shows pictorially the BEM sectioning scheme outlined so far. Again, no mathematical cancellation is performed. Each

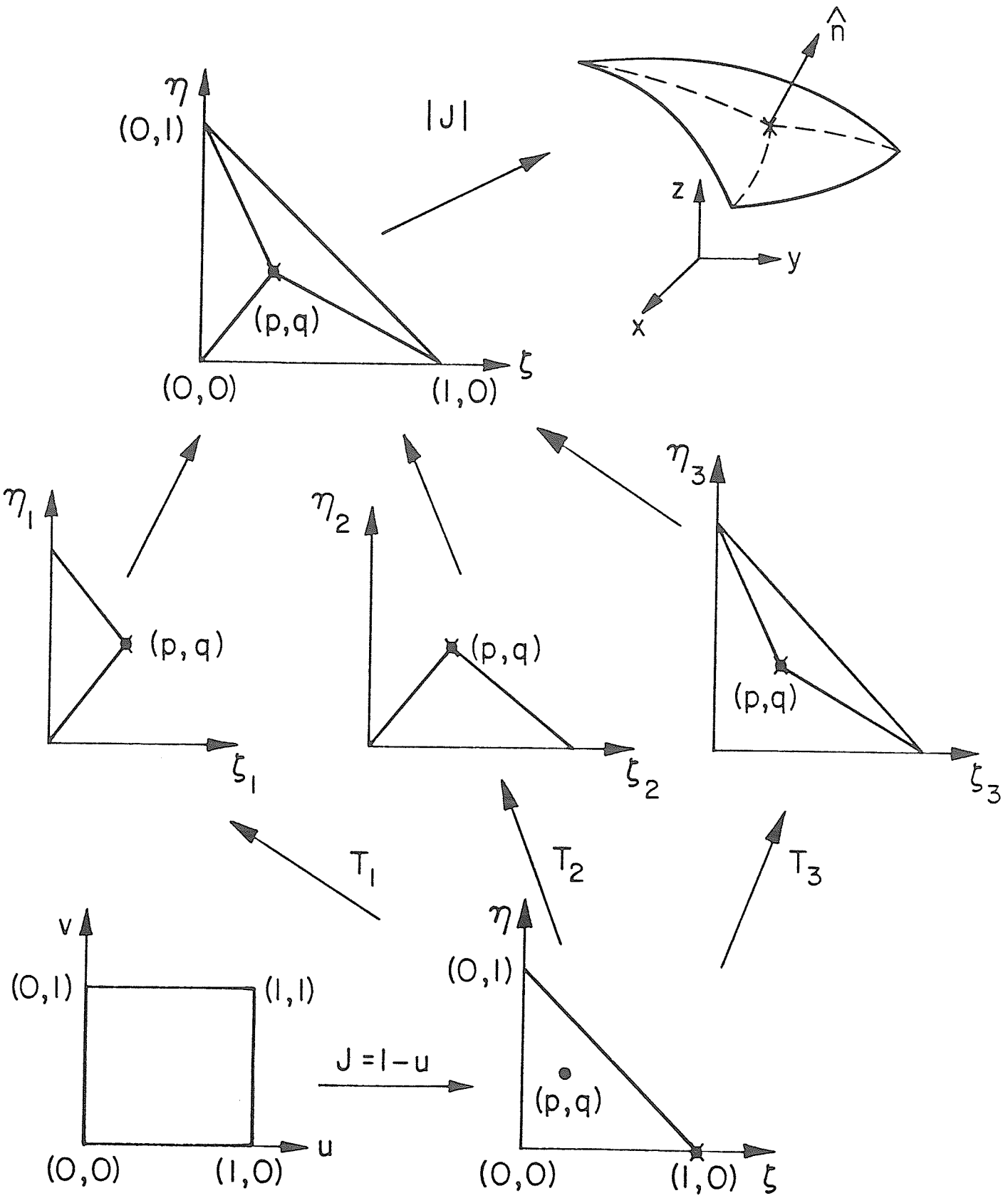

FIG. 3.8: BEM sectioning scheme for r^{-1} singularity

of equations [3.27], [3.28] and [3.29] is seen to be finite in the limit of vanishing r.

This scheme may be extended for use in the time-harmonic case since the term $\exp[-jk|\bar{r} - \bar{r}'|]$ tends to unity as $\bar{r} \to \bar{r}'$. Provided the kernel is not overly oscillatory, the Gauss-Legendre quadrature formula will give good precision. For high frequencies, special quadratures with cos kx and sin kx weights may be generated by the Gram-Schmidt procedure outlined in Section 3.1.

3.3 Implementation for Geometric Singularity

Other factors that contribute to aberrations in field solution include: incompatibility of boundary conditions at common edges or points; and abrupt changes in direction of boundary surfaces or contours that lead to infinite values of the derivative of the field. The latter form arises wholly from geometrical considerations and frequently causes a situation where the integrand is singular but the integral finite. Interpolatory polynomials, no matter how high their order, cannot be expected to represent the field in the vicinity of the singular point as accurately as desired — mathematically because the set of polynomial functions is not *complete* for this task. Hence, convergence is usually slow and at times even erratic depending on the degree of modelling and the method of solution. The prediction of singular behaviour is dependent on expansions of the solution near corners and jumps in boundary conditions. In general, to accelerate convergence, special functions are required to approximate the discontinuous behaviour of the field.

Explicit forms and orders of singularity are obtainable in closed form from two-dimensional analyses of geometries where separation of variables may be invoked. For the static field case with the Laplacian

operator $-\nabla^2$ acting on potential ϕ, the leading term of the infinite series expansion of normal derivative $\frac{\partial\phi}{\partial n}$ behaves as $r^{-\nu}$, with r being the distance from the corner and $\nu = (1 - \frac{\pi}{\delta})$ where δ is the re-entrant angle (Figure 3.9). This term is proportional to surface charge density σ which is singular as $r \to 0$ whenever $\pi < \delta \leq 2\pi$. Hence edges and right-angled corners would have orders $r^{-1/2}$ and $r^{-1/3}$, respectively.

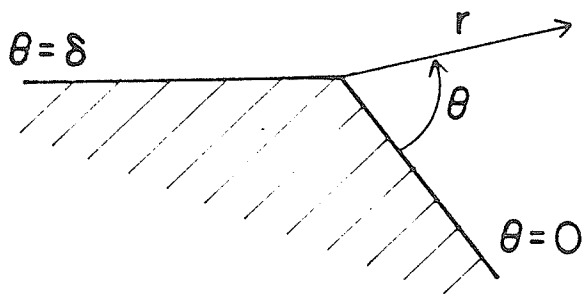

FIG. 3.9: Geometrical corner of re-entrant angle δ

Traditional practise has been to rely on conformal transformation to ameliorate the geometrical discontinuity. An improved numerical method is to introduce terms in $r^{-\nu}$ into the regular interpolatory polynomials either by addition or multiplication. The additive procedure

operates by adding a separate variational parameter that contains the form of the singularity, to the regular univariate polynomial currently used as a trial function, *i.e.*,

$$\sigma(\zeta) = \sum_{i=0}^{n} a_i \zeta^i + \frac{a_{n+1}}{(b - \zeta)^{\nu}} \qquad [3.30]$$

where $(b - \zeta)$ describes the distance from the corner, n the degree of approximation, ν the form of the singularity, and a_i the unknown coefficients of the trial function.

Another alternative is to multiply each term of the univariate polynomial by the form of the singularity to obtain

$$\sigma(\zeta) = \sum_{i=0}^{n} a_i \frac{\zeta^i}{(b - \zeta)^{\nu}} \qquad [3.31]$$

resulting in one less variable for the same degree of interpolation. Normalization of these trial functions in the context of the BEM, is achieved by defining the polynomic set over the unit interval $[0, 1]$ described by the spatial variable ζ. Each application of the scheme would require only a spatial transformation of quadrature points together with a sizing of the weights to suit the dimension b. In fact, for the scheme given by [3.31], a Gauss quadrature formula with weight function $(1 - \zeta)^{-\nu}$ could be generated to obtain optimal precision with minimal sampling. Hence, the remaining portion of the integrand is regular and may be computed in a straight-forward manner. Using these techniques, the different orders of singularity described over the range: $\pi < \delta \leq 2\pi$ may be accurately handled.

The same methodology may be extended for use over parametric surfaces where field discontinuities at any one or all edges may be handled by judicious choice of combinations of quadrature formulas to form the product rule. This tailoring of quadrature rules to cater for singularities to the integrand is a powerful tool that has yet to be exploited for field solution. A corresponding analysis on time-harmonic fields would result in asymptotic forms that resemble Bessel functions of non-integer order which could possibly be treated in like manner.

IV. ELECTROSTATIC FIELD PROBLEMS

Problems in this context include those that require the solution of Laplace's or Poisson's equation subject to Dirichlet and/or Neumann boundary conditions. Integral equation formulations in terms of boundary sources are compact, and particularly attractive for open-region problems. Included in this chapter is a discussion on the relative merits of certain formulations, and sample applications of the BEM to some classical problems in potential theory.

4.1 Integral Formulations

From scalar potential theory, harmonic functions ϕ may be represented by simple-layer or double-layer (dipole) potentials thus giving rise to the class of Fredholm integrals. A function is harmonic if it is continuous, differentiable to second order, and satisfies Laplace's equation everywhere (Jaswon & Symm, 1977). By definition, Green's function $G[\bar{r}|\bar{r}']$ is harmonic everywhere except at the source-point where $\bar{r} = \bar{r}'$ so that it formally satisfies the Poisson equation

$$-\nabla^2 G[\bar{r}|\bar{r}'] = \delta(\bar{r} - \bar{r}') \qquad [4.1]$$

Another alternative formulation may be obtained directly from Green's formula where the harmonic function is represented as a superposition of both the above source-types. The following discussion has particular relevance to the Dirichlet problem. Neumann and mixed boundary value problems are catered for by extension.

4.1.1 Simple-Layer Kernel

This potential ϕ is due to a distribution of simple charges σ on a surface S, not necessarily closed, such that

$$\phi(\bar{r}) = \frac{1}{\varepsilon_0} \int_S G[\bar{r}|s'] \, \sigma(s') \, ds' \quad ; \quad \bar{r} \in S + R \qquad [4.2]$$

where G is the appropriate Green's function that ensures a bounded solution for ϕ; $\bar{r}$ the observer location; ε_0 the permittivity of free-space; and s' the surface over which σ is distributed. From [4.2], potential ϕ is continuous across boundary S. However, normal derivatives (flux) are discontinuous by an amount proportional to the charge spread over it, *i.e.*

$$- \left. \frac{\partial \phi}{\partial n} \right|_S = \frac{\sigma(s)}{\varepsilon_0} \qquad [4.3]$$

The above relation is obtained from summing the normal derivatives of [4.2] taken in opposing directions. As a consequence, [4.2] may now be rewritten as

$$\phi(\bar{r}) = - \int_S G[\bar{r}|s'] \, \frac{\partial \phi(s')}{\partial n'} \, ds' \quad ; \quad \bar{r} \in S + R \qquad [4.4]$$

If S is closed, and a Dirichlet boundary condition $\phi(s) = g(s)$ prescribed, the exterior Dirichlet problem is posed as

$$\frac{1}{\varepsilon_0} \int_S G[\bar{r}|s'] \, \sigma(s') \, ds' = g(s) \qquad [4.5]$$

which is a Fredholm integral of the first kind. The variational/Galerkin formulation of [4.5] is given by

$$\int_S \underline{\alpha}(s)\, \frac{1}{\varepsilon_0} \int_S G[s|s']\, \underline{\alpha}^T(s')\, ds'ds\, \underline{\sigma} = \int_S \underline{\alpha}(s)\, g(s)\, ds \qquad [4.6]$$

which is solved for $\sigma(s')$. Potential ϕ everywhere is then computed from [4.2]. In the event that $g(s)$ is independent of position, then ϕ everywhere interior to S has the value $g(s)$ as well by the interior Dirichlet existence theorem.

4.1.2 Double-Layer Kernel

The potential ϕ due to a distribution of double-layer (dipole) charges μ on S is given by

$$\phi(\bar{r}) = \frac{1}{\varepsilon_0} \int_S \frac{\partial G[\bar{r}|s']}{\partial n'}\, \mu(s')\, ds' \qquad [4.7]$$

where the normal derivative of G with respect to the primed variable denotes the direction of dipole moment. For clarity, consider Figure 4.1 where two equal and opposing charges q of magnitude $|\frac{1}{h}|$ and separation h are made to straddle boundary S. The potential F resulting from this arrangement has to satisfy the Poisson equation

$$-\nabla^2 F = \frac{\delta(\bar{r} - \{\bar{r}' + h\hat{p}\}) - \delta(\bar{r} - \bar{r}')}{h} \qquad [4.8]$$

where F is defined along the lines of G.

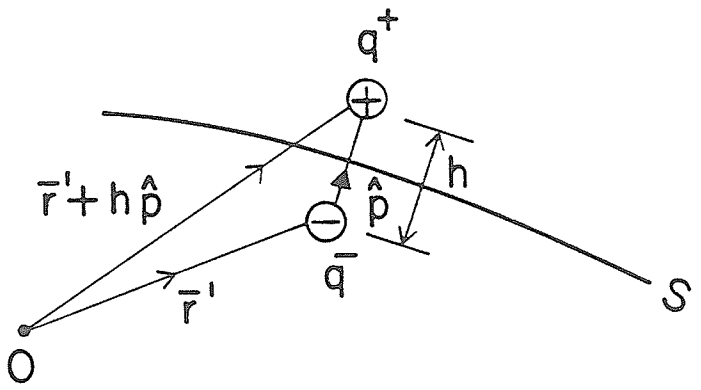

FIG. 4.1: Dipole configuration

In the limit as $h \to 0$, $|q| \to \infty$ so that $|qh| = 1$. Hence, the limiting configuration of [4.8] is that of a dipole of axis $\hat{p}$ oriented in the direction of $\hat{n}$ such that

$$-\nabla^2 F = \frac{d}{dn'} \delta(\bar{r} - \bar{r}') \qquad [4.9]$$

and F is seen to be the double-layer kernel of [4.7].

Potential ϕ is harmonic everywhere in R except on S where the integral jumps by an amount $\frac{\mu(s)}{2\varepsilon_0}$, *i.e.*,

$$\phi(s) = \frac{1}{\varepsilon_0} \int_S \frac{\partial G[s|s']}{\partial n'} \mu(s')\, ds' - \frac{\mu(s)}{2\varepsilon_0} \qquad [4.10]$$

which is a Fredholm second kind integral. From physical considerations, the relation

$$\phi(s) = -\frac{\mu(s)}{\varepsilon_0} \qquad [4.11]$$

can be established (Jaswon & Symm, 1977) to enable [4.7] to be rewritten as

$$\phi(\bar{r}) = -\int_S \frac{\partial G[\bar{r}|s']}{\partial n'} \phi(s')\, ds' \quad ; \quad \bar{r} \notin S \qquad [4.12]$$

a form that specifies ϕ everywhere with respect to potential on the boundary. The Galerkin formulation of [4.10] subject to the condition $\phi(s) = g(s)$, is

$$\int_S \underline{\alpha}(s) \frac{1}{\varepsilon_0} \int_S \frac{\partial G[s|s']}{\partial n'} \underline{\alpha}^T(s')\, ds'ds\ \underline{\mu} - \int_S \underline{\alpha}(s)\, \underline{\alpha}^T(s) \frac{1}{2\varepsilon_0} ds\ \underline{\mu} = \int_S \underline{\alpha}(s)\, g(s) ds \qquad [4.13]$$

which is solved for $\mu(s')$. Then ϕ everywhere is computed from [4.7]. For the explicit purpose of specifying ϕ in R, a shorter route is to use the expression [4.12] directly assuming $\phi(s')$ is known. For the special case $g(s)$ is constant on S, ϕ in the interior has the value $g(s)$ while in the exterior region, ϕ is identically zero. In crossing each layer of charges, ϕ jumps by $\frac{-\phi(s)}{2}$.

4.1.3 Green's Theorem Representation

Consider the two point-form equations that symbolize the electrostatic field problem

$$-\nabla^2 \phi = 0 \qquad [4.14]$$

and

$$-\nabla^2\, G[\bar{r}|\bar{r}'] = \delta(\bar{r} - \bar{r}') \qquad [4.15]$$

Application of the divergence theorem to the form resulting from the subtraction of scalar products G x [4.14] from ϕ x [4.15] results in

$$\phi(\bar{r}) = \gamma \int_S \{G[\bar{r}|s'] \frac{\partial\phi(s')}{\partial n'} - \phi(s') \frac{\partial G[\bar{r}|s']}{\partial n'}\} ds' \qquad [4.16]$$

where

$$\gamma = \begin{cases} 0 & \bar{r} \in R_i \\ -1 & \bar{r} \in R_e \\ -2 & \bar{r} \in S \end{cases} \qquad [4.17]$$

is as defined in Stakgold (1968). The negative signs in [4.17] are due to the assigned direction of surface normals — directed into R_e for the exterior problem. The physical implication of $\gamma = 0$ is that G in [4.15] is harmonic since $\bar{r}$ is outside the region of interest. Finally, the reason for $\gamma = -2$ in S is because the surface is assumed to obey a Liapunov condition (defined in the context of Zabreyko *et al* (1975) and Jaswon & Symm (1977)). Part of the requirements for this condition is that the surface be smooth and possess a tangent plane and normal (not necessarily a curvature), at each point. Thus for abrupt changes in boundary description, the actual value of γ (at that point) should be -2π (or -4π) divided by the re-entrant angle δ (or solid angle spanned by the re-entrant corner in three-dimensions). However, this requirement is usually relaxed in engineering practise with very little penalty to solution accuracy.

Equation [4.16] permits ϕ everywhere to be specified in terms of boundary data $\phi(s')$ and $\frac{\partial\phi(s')}{\partial n'}$, where one or the other is usually a known quantity. For the exterior Dirichlet problem under consideration, [4.16] with $\gamma = -2$ and $\phi(s) = g(s)$ gives

$$\int_S G[s|s'] \frac{\partial \phi(s')}{\partial n'} ds' = \int_S \frac{\partial G[s|s']}{\partial n'} g(s') ds' - \frac{g(s)}{2} \qquad [4.18]$$

with the accompanying Galerkin formulation

$$\int_S \underline{\alpha}(s) \int_S G[s|s'] \underline{\alpha}^T(s') ds' ds \frac{\partial \underline{\phi}}{\partial n'} = - \int_S \underline{\alpha}(s) \frac{g(s)}{2} ds + \int_S \underline{\alpha}(s) \int_S \frac{\partial G[s|s']}{\partial n'} \underline{\alpha}^T(s') ds' ds \, \underline{g} \qquad [4.19]$$

Once $\frac{\partial \phi}{\partial n'}$ is ascertained, [4.16] is used with the appropriate γ to compute ϕ everywhere. On examining equations [4.4] and [4.12] in conjunction with [4.16], it is clear that the potential ϕ in R_e given by the Green's Theorem representation, is identical to that obtained from a linear combination of the simple and double-layered potentials. Thus,

$$\phi(\bar{r}) = \phi_s(\bar{r}) - \phi_d(\bar{r}) \quad ; \quad \bar{r} \notin S \qquad [4.20]$$

where ϕ_s and ϕ_d represent the potentials obtained from [4.4] and [4.12], respectively.

The form utilizing the simple-layered potential is traditionally preferred mainly because its system matrix is more economical to generate. Furthermore, ϕ and its derivatives in R, may be computed without much regard to the singularity of G except when the point of evaluation is inordinately close to the boundary S. The double-layered potential formulation has the advantage of being a Fredholm second kind integral which is mathematically preferred due to its better-behaved kernel. Because of the additional term to be considered in matrix accumulation, thus constitutes an added expense when compared to the former

scheme. For the particular case of the constant Dirichlet boundary, this form is not practical for implementation due to its lack of field definition in R. In the case of the Green's Theorem formulation, more CPU time is required to compute not only the excitation function prior to solution, but also the potential ϕ in R. Precision attainable is comparable with that of the simple-layer formulation and thus does not indicate any advantage except for the situation when mixed boundary conditions need be considered. Also, equation [4.16] is a function of γ so that in ϕ computation, special verification software is required to ascertain if $\bar{r} \in S$ or R. As such, [4.16] is not as freely applicable as [4.2].

4.2 The Strip Capacitor Problem

Consider the capacitive arrangement of two identical infinitely-long, parallel conducting strips charged to a potential difference of 2 volts (Figure 4.2). Using quarter-plane symmetry, the problem is reduced to solving

$$\frac{1}{\varepsilon_0} \int_S G_m[s|s'] \, \sigma(s') \, ds' = 1 \qquad [4.21]$$

in the positive quadrant, where G_m is the modified form of the two-dimensional free-space Green's function and is given by

$$G_m[x,y|x',y'] = -\frac{1}{2\pi} \ln \left\{ \frac{[(x-x')^2 + (y-y')^2][(x+x')^2 + (y-y')^2]}{[(x+x')^2 + (y+y')^2][(x-x')^2 + (y+y')^2]} \right\}^{\frac{1}{2}} \qquad [4.22]$$

Charge density σ is singular at the open edge with an expected form $r^{-\frac{1}{2}}$. The capacitance and potential at the field point $(x,y) \equiv (\frac{40}{9}, 10)$ are respectively given as 18.72 pF/m (positive quadrant alone) and

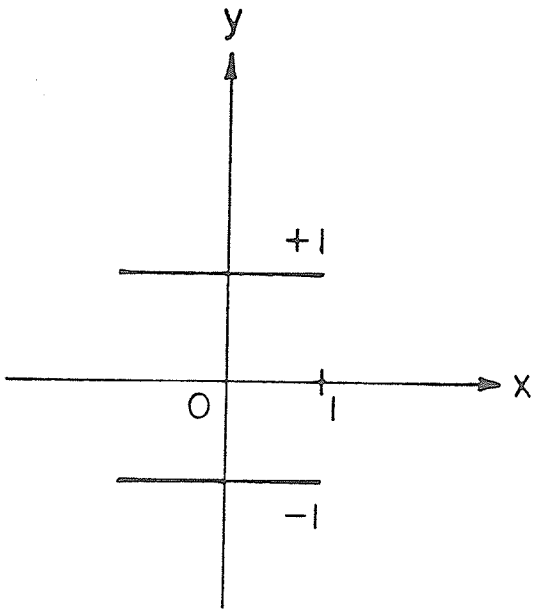

FIG. 4.2: Strip capacitor assembly

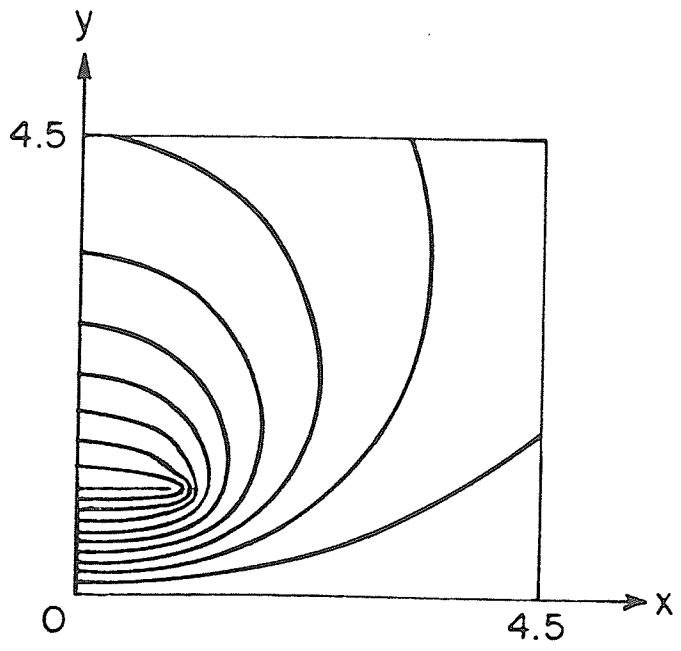

FIG. 4.3: Equipotentials around plate

0.1124 volts by McDonald *et al* (1974) from a rigorous analysis. The authors used singular trial functions to model charge behaviour, and an *addition-subtraction* technique to isolate four singular integrands arising from both the charge and Green's function singularities. Each of these singular integrands were then integrated analytically. The primary motivation in addressing this specific example now, is to test those numerical tools developed in Chapter III. Accordingly, the analysis is carried out with the following objectives in mind:

(i) solve the problem variationally, treating only Green's function singularity using the procedure outlined in Subsection 3.2.1. Charge behaviour is modelled by the univariate polynomial expansion

$$\sigma(x) = \sum_{i=0}^{N} a_i x^i \qquad [4.23]$$

(ii) as in (i), with the additional treatment of charge singularity by multiplying the form $(1 - x)^{-\frac{1}{2}}$ into the polynomial expansion for σ, *i.e.*,

$$\sigma(x) = \frac{1}{\sqrt{1 - x}} \sum_{i=0}^{N} a_i x^i \qquad [4.24]$$

so that every variational parameter is modulated; and,

(iii) as in (i) and (ii) but by adding in a term with the form $(1 - x)^{-\frac{1}{2}}$, *i.e.*,

$$\sigma(x) = \sum_{i=0}^{N} a_i x^i + \frac{a_{N+1}}{\sqrt{1 - x}} \qquad [4.25]$$

For each of [4.23] to [4.25], N represents the order of the approximating polynomial. In particular, for (ii), a quadrature formula with

$(1 - x)^{-\frac{1}{2}}$ as weight (*i.e.*, $\alpha = -\frac{1}{2}$, $\beta = 0$ for the Gauss-Jacobi weights of [3.7]) is used for integration with respect to the unprimed variable. Over the *self-element* the kernel is doubly-singular, and can only be treated analytically. In this numerical application, even with the benefit of a cosine substitution, the malady remained — the transformed weights being multiplied by a $(1 - x^2)^{-\frac{1}{2}}$ term. With the understanding that variationally, convergence in *energy* is guaranteed, only the logarithmic singularity is formally addressed in this analysis; the $r^{-\frac{1}{2}}$ singularity is compensated for only by an increase in quadrature order. With increasing quadrature the value of the functional should minimize to the expected solution. One justification for this choice is that unlike the Green's function which is singular everywhere on the strip, the $(1 - x)^{-\frac{1}{2}}$ form is singular only at the edge. Thus less emphasis may be placed on this localized effect.

The results of using [4.23] as trial functions are shown in Figure 4.4 and Table 4.1. In particular, the set of results for the single pulse (N = 0) case is superior to those of McDonald *et al* (1974) who obtained values of 17.72 pf/m and 0.1063 for capacitance and potential, respectively. It should be pointed out that the tabulated quantities are *converged* values meaning that no further improvement can be had after the specified quadrature order. The exact results are obtained with a quartic approximation though charge profile (Figure 4.4), is far from the expected behaviour. This is because capacitance is numerically equal to the magnitude of the functional, and hence shares the accuracy of the energy-convergent solution.

TABLE 4.1: Strip capacitor; $\sigma(x) = \sum_{i=0}^{N} a_i x^i$

order of polynomial	number of unknowns	order of quadrature	capacitance pF/m	$\phi(\frac{40}{9}, 10)$
0	1	2	18.03	.1083
1	2	2	18.51	.1111
2	3	3	18.70	.1122
3	4	5	18.71	.1123
4	5	8	18.72	.1124

TABLE 4.2: Strip capacitor; $\sigma(x) = \frac{a_0}{\sqrt{1 - x}}$

order of quadrature	weight function	capacitance pF/m	$\phi(\frac{40}{9}, 10)$
15	1	18.73	.1124
8	$\frac{1}{\sqrt{1 - x}}$	19.02	.1141

TABLE 4.3: Strip capacitor; $\sigma(x) = \sum_{i=0}^{N} a_i x^i + \frac{a_N + 1}{\sqrt{1 - x}}$

order of polynomial	number of unknowns	order of quadrature	capacitance pF/m	$\phi(\frac{40}{9}, 10)$
-	1	8	19.02	.1141
0	2	11	18.72	.1124
1	3	11	18.72	.1124
2	4	11	18.72	.1124
3	5	11	18.72	.1124
4	6	11	18.72	.1124

With the charge behaviour modelled as in [4.24], results show that the $N = 0$ approximation, *i.e.*

$$\sigma(x) = \frac{a_0}{\sqrt{1 - x}} \qquad [4.26]$$

produces the same accuracy as higher-ordered forms. In particular, two quadrature rules were implemented for integration with respect to the unprimed variable. Table 4.2 shows the computed values using the respective weight functions. The first set are for results closest to the expected values and the second, the converged values using a quadrature rule that takes into account the singular form $(1 - x)^{-\frac{1}{2}}$. This latter set is expected to be the more accurate since the quadrature is tailored explicitly for use. In fact, the functional for the first set is seen to converge beyond the tabulated quadrature order of 15, and in the limit, approach the value for the second set.

Finally, the results using [4.25] for charge distribution are shown in Table 4.3. The case indicating [4.26] corresponds to the first row and is meant for comparison purposes. The remaining rows, representing increasing orders of the polynomial, show identical *converged* results. Obviously, little improvement in precision is gained beyond the approximation which represents

$$\sigma(x) = a_0 + \frac{a_1}{\sqrt{1 - x}} \qquad [4.27]$$

It appears that the appropriate form of the approximating function for σ, should be that of [4.25] so that in the solution process, the variational parameters have the flexibility to attain values that would collectively produce the optimal field solution. Multiplying each

parameter by the expected form of the singularity, is probably functionally restrictive thus constraining the solution to converge on the erroneous value. Besides, the form of [4.24] may not be *complete* in the sense of being a proper trial function for this problem. To appreciate this point, consider the analytic solution of Laplace's equation in polar coordinates (Decretion, 1972)

$$r^2 \frac{\partial^2 \Phi}{\partial r^2} + r \frac{\partial \Phi}{\partial r} + \frac{\partial^2 \Phi}{\partial \theta^2} = 0 \qquad [4.28]$$

Equation [4.28] is separable into a system of Sturm-Liouville equations which may be solved for the general solution

$$\Phi(r, \theta) = \sum_{s=-\infty}^{\infty} [a_s r^s \sin s\theta + b_s r^s \cos s\theta] \qquad [4.29]$$

where the summation extends over values of s to be determined. The normal derivative along the edge of the corner is given by

$$\frac{\partial \Phi}{\partial n} = \frac{1}{r} \frac{\partial \Phi}{\partial \theta} = \frac{1}{r} \sum_{s=-\infty}^{\infty} [s a_s r^s \cos s\theta - s b_s r^s \sin s\theta] \qquad [4.30]$$

Enforcement of the boundary conditions that

$$\Phi(r, \theta = 0) = \Phi(r, \theta = \delta) = 1 \qquad [4.31]$$

in equation [4.29] results in the requirement

$$s = \frac{k}{\delta} \pi \qquad [4.32]$$

where k is an integer, and δ the re-entrant angle. Hence, the expression for charge resembles

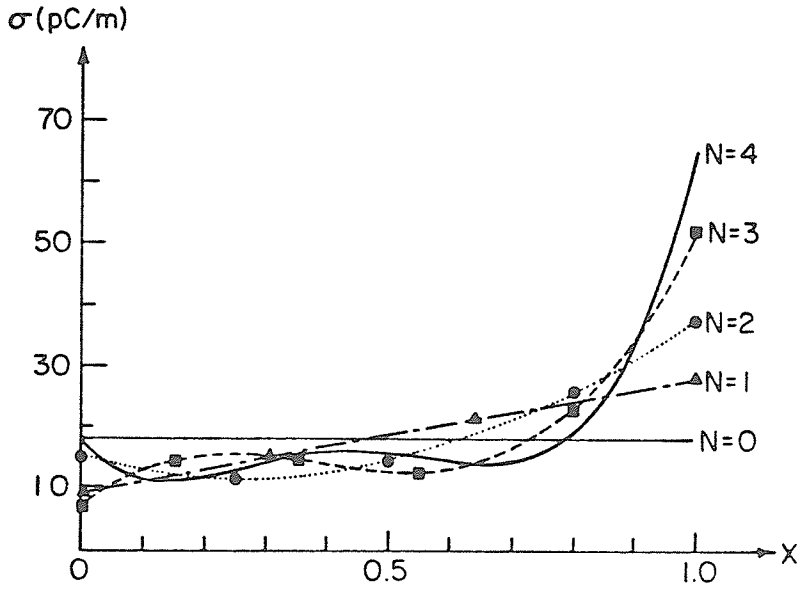

FIG. 4.4: Charge profile on strip capacitor - without singular term

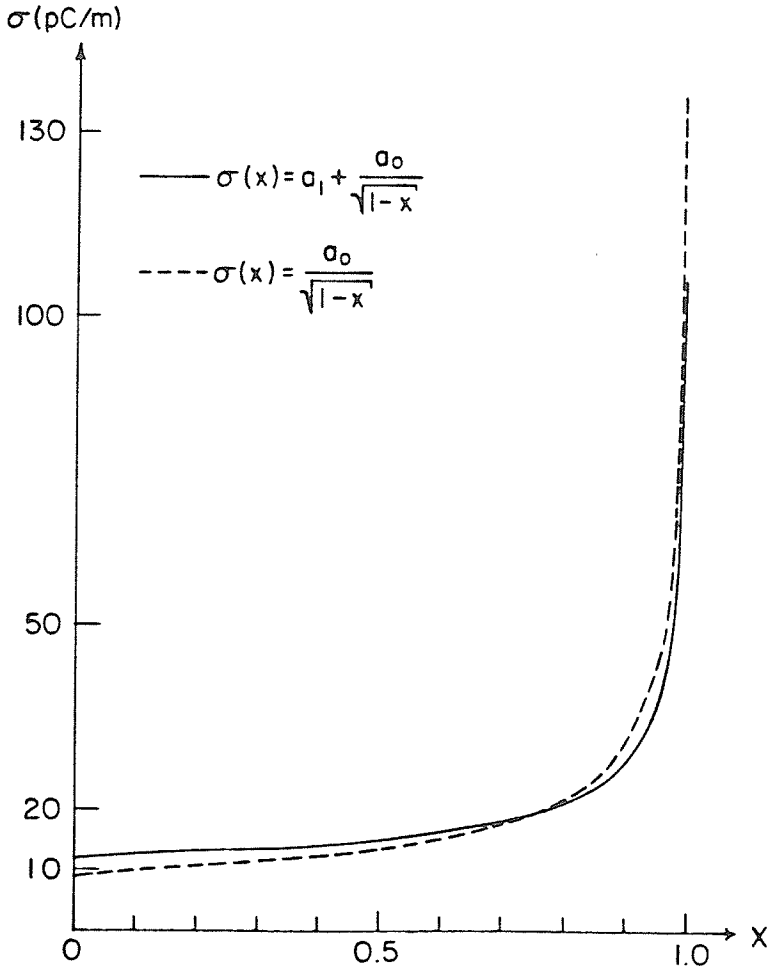

FIG. 4.5: Charge profile on strip capacitor - with singular term

$$\sigma = -\varepsilon_0 \frac{\partial \Phi}{\partial n} = \sum_{k=0}^{\infty} \varepsilon_0 \, b_k \left(k \frac{\pi}{\delta}\right) r^{\left(k \frac{\pi}{\delta} - 1\right)} \sin\left(k \frac{\pi}{\delta}\right)\theta \quad [4.33]$$

whose $k = 1$ term contains the form of the charge singularity if $\delta = 2\pi$. Higher order terms are regular in r thus indicating that the approximating form of [4.25] is more appropriate.

Charge profiles for both [4.26] and [4.27] requiring 1 and 2 unknowns respectively, are plotted in Figure 4.5 and should be compared against the $N = 4$ curve in Figure 4.4 which involves 5 unknowns. Obviously the latter should not be used if charge distribution data is required. For the same accuracy using pulse-expansion, McDonald *et al* (1974) required 50 unknowns. Thus two inferences become clear: —

(i) for the same accuracy with less unknowns, a fewer number of collocation sections with higher-order source interpolation is preferred to a large number of pulse expansion sections; and

(ii) if the form of the singularity is known, it should be added to the polynomial trial function as an extra term so that if the smooth portion of the function is not required, it may be duly penalized by the variational procedure.

4.3 The Exterior Dirichlet Problem

This example is intended to illustrate the equivalence of the three types of integral formulations derived in Section 4.1. In particular, consider the exterior problem posed by an equipotential circular boundary of radius a, charged to a potential of 1 volt. The two-dimensional free-space Green's function is given by

$$G[\bar{r}|r'] = -\frac{1}{2\pi} \ell n|\bar{r} - \bar{r}'| \qquad [4.34]$$

thus indicating a potential that goes to infinity as $|\bar{r} - \bar{r}'| \to \infty$. Mathematically, this situation arises because operator K is not positive definite. But K can be made so by adding to [4.34] a positive constant, *i.e.*

$$G[\bar{r}|\bar{r}'] = -\frac{1}{2\pi} \ell n|\bar{r} - \bar{r}'| + \frac{1}{2\pi} \ell n|\bar{r}_R - \bar{r}'| \qquad [4.35]$$

where the reference point $\bar{r}_R$ can be chosen quite far away to make the second term of [4.35] approximately constant. The physical effect of this manipulation is to regularize the potential behaviour so that it vanishes logarithmically as $|\bar{r}| \to |\bar{r}_R|$.

In the case of a circular cylinder of radius a, the exact values for the potentials are widely known and may be evaluated from the expression

$$\phi(r) = \begin{cases} \frac{\sigma_0 a}{\varepsilon_0} [-\ell n\ a + \ell n\ R] & ;\quad r \leq a \\ \\ \frac{\sigma_0 a}{\varepsilon_0} [-\ell n\ r + \ell n\ R] & ;\quad r \geq a \end{cases} \qquad [4.36]$$

where $R = |\bar{r}_R - \bar{r}'|$, and σ_0 is an assumed simple-layer, uniform charge distribution on the cylinder. Setting $r = a$ and enforcing $\phi(r = a) = 1$, [4.36] gives the relation

$$\frac{\sigma_0 a}{\varepsilon_0} = \frac{1}{\ell n\ R - \ell n\ a} \qquad [4.37]$$

or which when substituted into the right-hand side of [4.36], now gives

$$\phi(r) = \begin{cases} 1 & ; \quad r \leq a \\ \dfrac{\ell n\ R - \ell n\ r}{\ell n\ R - \ell n\ a} & ; \quad r \geq a \end{cases} \qquad [4.38]$$

For the purpose of numerical computation, the coordinates of $\bar{r}_R$ are chosen to be $(x_R, y_R) \equiv (10^3, 10^3)$, thus making $R = 10^3\sqrt{2}$. In particular, a is set at unity. Using quarter-plane symmetry, the modified Green's function [4.35] now resembles

$$G[x,y|x',y'] = -\frac{1}{2\pi} \ell n[(x \pm x')^2 + (y \pm y')^2]^{\frac{1}{2}} + \frac{1}{2\pi} \ell n[(x_R \pm x')^2 + (y_R \pm y')^2]^{\frac{1}{2}} \qquad [4.39]$$

which may be expanded into four terms, one for each quadrant. The BEM model is just one quartic element comprising 5 nodes. Denoting ϕ_1, ϕ_2 and ϕ_3 to be the respective potentials computed from the solutions of [4.6], [4.13] and [4.19], the numerically calculated values for different values of r are shown in Table 4.4. Incremental values of r are given by $\Delta r = .3278$.

TABLE 4.4: Potentials - Exterior Dirichlet Problem

r	ϕ_1	ϕ_2	ϕ_3	$\phi_1-\phi_2$	Exact ϕ
Δr	1.0003	1.0000	.0003	.0003	1.0
1.0	.9996	1.0000	.9992	-	1.0
$4\Delta r$	.9629	.0	.9629	.9629	.9627
$6\Delta r$	.9070	.0	.9070	.9070	.9068
$8\Delta r$	.8673	.0	.8673	.8673	.8671

Within the cylinder, the exact solution is best calculated from the double-layer (ϕ_2) kernel expression [4.7]. It is interesting to note that for ϕ_3, the condition that $\gamma = 0$ from [4.17] is not imposed but the computed value is seen to be vanishingly small and equal to a linear combination of ϕ_1 and ϕ_2 as defined in equation [4.20]. For the exterior potentials, very good correlation is evident from observation of the bottom three rows of columns 2, 4, 5 and 6.

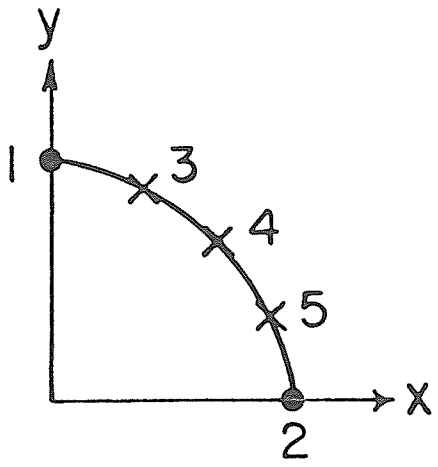

FIG. 4.6: BEM model of circular cylinder - positive quadrant

4.4 Capacitance of Conducting Solids

In the static field problem, the functional has special significance at the solution point. Consider equation [2.2] where the first term of the first scalar product, namely Kf, is the potential g on S. The product of potential and charge integrated over surface S, yields the potential energy of the system. Correspondingly, the second inner product yields twice the energy. From an energy point of view, this is the exact parallel of the variationally formulated partial differential equation functional (Wexler, 1980). Based on this energy concept, the electrostatic capacitance of the system may be readily obtained. In matrix notation, the functional

$$F = \underline{f}^T S\underline{f} - 2\underline{f}^T \underline{b} \qquad [4.40]$$

reduces to

$$F = -\underline{f}^T \underline{b} \qquad [4.41]$$

at the minimum. Thus evaluation of functional magnitude requires merely the multiplication of a row and a column matrix. For conducting bodies, this magnitude is twice the electrostatic energy so that with an equipotential boundary, the capacitance C of the system will be given directly by

$$C = \frac{|F|}{g^2} \qquad [4.42]$$

The capacitances of a sphere, prolate spheroid, and cube are calculated using equation [4.42]. With one-eighth symmetry, the respective BEM models need be developed only in the positive octant. The

modified Green's function is given by

$$G[x,y,z|x',y',z'] = \frac{1}{4\pi}\{\frac{1}{[(x \pm x')^2 + (y \pm y')^2 + (z \pm z')^2]^{\frac{1}{2}}}\} \qquad [4.43]$$

where the right-hand side incorporates eight terms to account for image symmetry. With the exception of the cube, exact values for capacitance are available for the two conic surfaces. In particular, for a unit sphere, the value is $4\pi\varepsilon_0$ or 111.26 pF whilst the expression for the prolate spheroid is

$$C = \frac{8\pi\varepsilon_0(a^2 - b^2)^{\frac{1}{2}}}{\ell n[\frac{a + (a^2 - b^2)^{\frac{1}{2}}}{a - (a^2 - b^2)^{\frac{1}{2}}}]} \qquad [4.44]$$

from Van Bladel (1964) where a and b are the semi-major and semi-minor axes. With $a = 2$ and $b = 1$, equation [4.44] returns a value of 146.33 pF. Table 4.5 shows some results obtained using a few BEM models.

TABLE 4.5: Capacitances of Spheroids

	degree of interpolation	number of elements	number of nodes	order of quadrature	capacitance pF
sphere	3	1	10	4	111.21
	2	4	15	4	112.07*
prolate spheroid	3	1	10	4	145.14
	2	14	39	3	146.34*

The asterisk * represents results previously published in Lean et al (1979b). An *addition-subtraction* method was used to cater for Green's function singularity. Thus, the analytic integration was performed on

four *flattened* patches representing each curved element. This *ad hoc* procedure caused the minimum of the functional to overshoot, hence, producing values of capacitance larger than the exact. Since the number of operations for matrix fill goes up as the square of the number of elements, the difference between computation times for rows 1 and 3 (also 2 and 4) is considerable. The present BEM model for the sphere uses a cubic element that allows two-digit accuracy in geometrical representation. Also, the new scheme for handling Green's function singularity is implemented to obtain less than .05% error in calculated capacitance. The prolate spheroid shows .8% error; considerably more than the sphere. This is because with the cubic interpolation scheme, there exists some arbitrariness in the positioning of the interior node (Mitchell & Wait, 1977). This flexibility can be used to advantage — by shifting this node towards the elongated region or *nose* in order to obtain better surface description. Thus, this value of capacitance can no doubt be improved.

Of special interest is the capacitance for a unit cube which was originally computed by Reitan & Higgins (1951) using their *method of subareas* — a method very similar to the pulse-expansion point-matching technique. Their value of .6555 e.s.u. is well within their predicted upper and lower bounds, *i.e.*, $.6221 < C < .7106$ e.s.u. Table 4.6 shows some results using a few BEM models.

TABLE 4.6: Capacitances of a Cube

* previously published in Lean *et al* (1979b)

degree of interpolation	number of elements	number of nodes	Order of quadrature	Capacitance pF	esu
1	6	7	4	72.94	.6556
2	6	19	5	73.00	.6561
3	6	37	5	73.13	.6573
1	12	10	4	73.12	.6572
2	12	31	4	73.19	.6578
2	12	31	4	73.03*	.6564

The first three rows of Table 4.6 show a monotonic improvement in computed capacitance in going to higher-order interpolation. Rows 5 and 6 are for a refined BEM model involving 12 elements. In comparing rows 3 and 4, it is obvious that 12 linear elements involving 10 unknowns have almost the same precision as 6 cubic elements with 37 unknowns. This means that a model with fewer high-order elements may not necessarily be better than another with more lower-order elements if the source discontinuities due to geometry — edges and corners — are not formally addressed. In any event the surface charge behaviour will not be accurate.

4.5 Sensitivity Study of a Metallic Body in a Finite Conducting Media

The physical problem configuration consists of a metallic body submerged in the ground, with a pair of injection-withdrawal electrodes at which electrical currents are caused to flow. The motivation for this simulation stems from the desire to monitor air-earth interface

potentials due to an arbitrarily positioned electrode-pair. Resulting changes in surface potentials caused by the presence; and subsequently, orientation, size and depth of the object, all contribute sensitivity information that may be used as *a priori* data for any subsequent computational stage.

To simulate this problem on a computer, the chosen model is that of a prolate spheroid with 8 cubic elements. An array of electrodes are located on the surface of the earth, assumed to be homogeneous with finite conductivity κ (Figure 4.7). Using half-plane symmetry (about x-z plane), where d is the depth of the origin below the surface, the Green's function is given by

$$G_m[x,y,z|x',y',z'] = \frac{1}{4\pi[(x-x')^2 + (y-y')^2 + (z-z')^2]^{\frac{1}{2}}} + \frac{1}{4\pi[(x-x')^2 + (y+y'-2d)^2 + (z-z')^2]^{\frac{1}{2}}} \qquad [4.45]$$

At the air-earth interface, two boundary conditions must hold — except at current injection and withdrawal sites, potential ϕ is continuous, and its derivative $\frac{\partial\phi}{\partial n}$, zero everywhere. Assuming only the static or low frequency case, the effects of displacement currents can be neglected. Also, the metallic body is very highly conducting in comparison to the surrounding media so that it may be assumed to be an equipotential surface. Thus, one need consider only the dual electrostatic problem posed by a constant Dirichlet boundary under the influence of two point charges As a result, the actual expression that needs to be solved, is

$$\frac{1}{\kappa}\int_S G_m[s|s']\,\sigma(s')ds' = g - \frac{2q}{\kappa}\{G[s|\bar{r}_1] - G[s|\bar{r}_2]\} \qquad [4.46]$$

where σ represents the surface charges and q, the magnitude of the point charges located at $\bar{r}_1$ and $\bar{r}_2$. The accompanying factor of 2

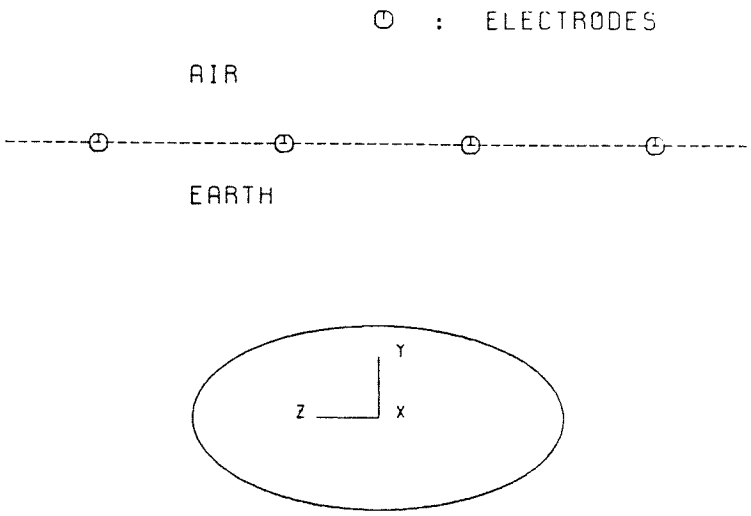

FIG. 4.7: Simulation problem geometry

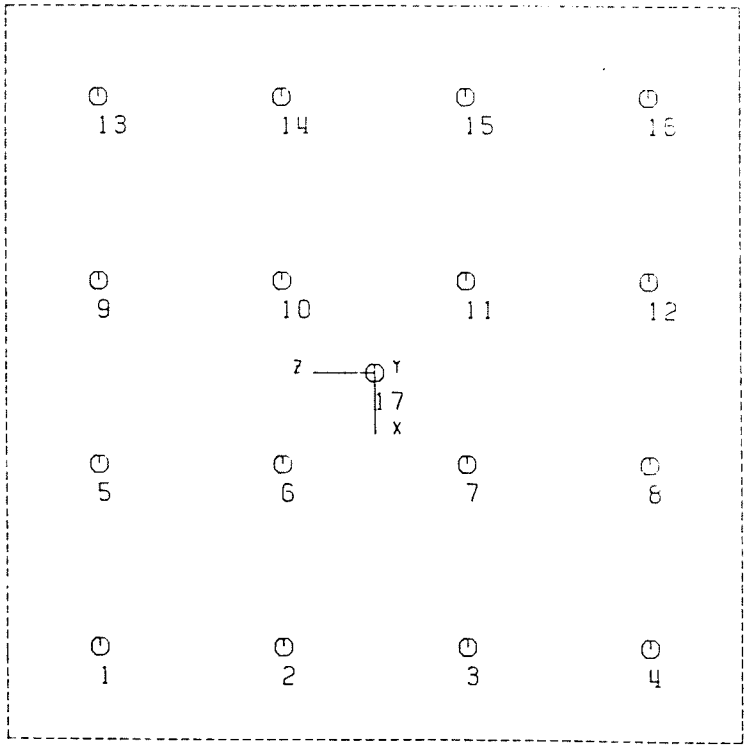

FIG. 4.8: Surface electrode grid

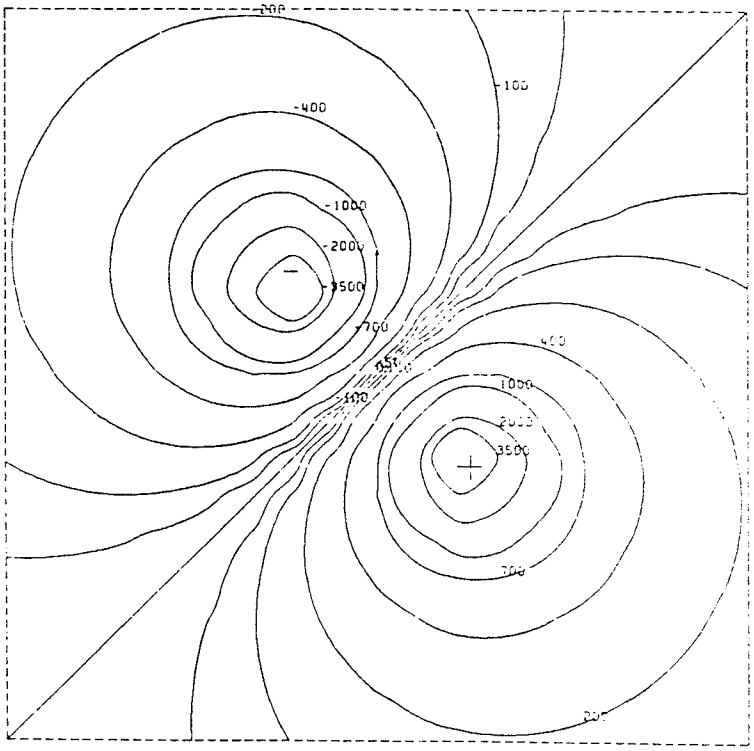

FIG. 4.9: Surface potentials - without object

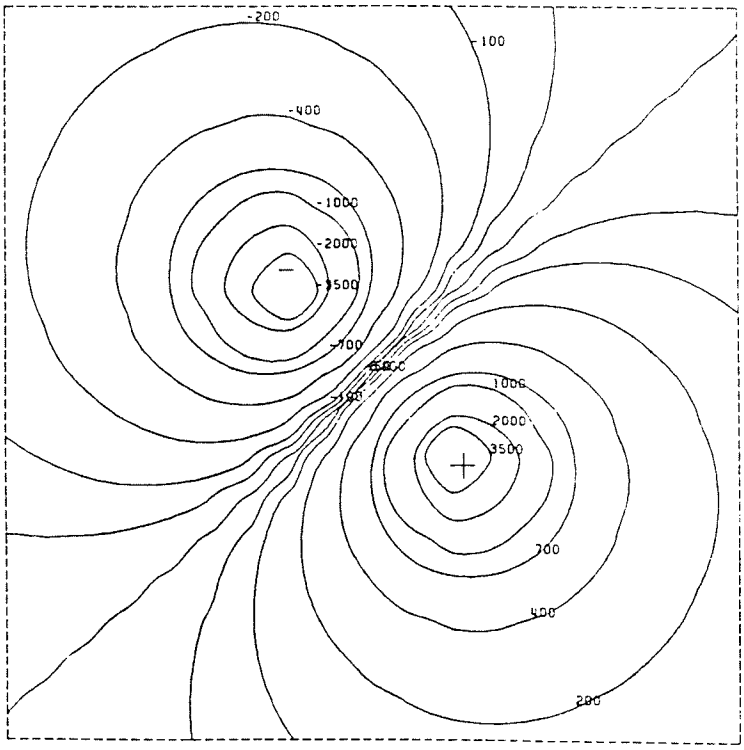

FIG. 4.10: Surface potentials - with object

accounts for half-plane symmetry. Parameter κ may then be interpreted as a scaling factor. Equation [4.46] is derived from the simple-layer formulation of [4.2]. The value of g corresponds to a Dirichlet boundary on the metallic object which may be conveniently set to zero since any non-zero value may be seen as a constant off-set. A polynomial (cubic) expansion, point-matching method is used for the solution of [4.46]. In matching only at element vertices, the Green's function singularity is not directly addressed. The surface potential maps of Figures 4.9 and 4.10 are for κ = .001 mhos/m and are reminiscent of those obtained using resistivity methods in geophysics (*e.g.*, Telford *et al* (1976)). Figure 4.8 shows a 4 x 4 electrode-grid placed at the interface at which potentials are evaluated and referenced to electrode 17. In particular, the injection and withdrawl sites are marked + and -, respectively. Figure 4.9 corresponds to a pure-dipole field due to the absence of the buried object. With the prolate spheroid centered in the grid and oriented length-wise horizontally across the page, the resultant inclination of the equipotentials in Figure 4.10 is produced. The waviness of the plots are a consequence of the coarse grid used for graphical interpolation. Although this application is an idealization of the physical problem, nevertheless it provided relevant quantitative data that gave an indication of the relative potential changes to be expected.

V. INTERFACE PROBLEMS IN MAGNETOSTATICS

A typical example of such a problem is that of the perturbation of a uniform magnetostatic field by a permeable body (Figure 5.1). Let $\hat{n}_i$ and $\hat{n}_e$ be unit normals directed into and out of the permeable body. Also, let material constants be μ_1 and μ_2 for the interior and exterior regions, respectively. From linearity of Maxwell's equations, one may consider an equivalent problem posed by the superposition of the applied field in R_e, and the perturbation field due to a polarization source distribution on S. This source distribution is a direct consequence of the interface condition and vanishes when $\mu_1 = \mu_2$. Thus, signifying $\bar{H}$, $\bar{H}_a$ and $\bar{H}_m$ to be the total, applied and perturbation fields respectively, then

$$\bar{H} = \bar{H}_a + \bar{H}_m \qquad [5.1]$$

and in particular if ϕ_a and ϕ_m are Laplacian in all R, then the total potential $\tilde{\phi}$ will be given by the algebraic summation of the corresponding scalar potentials, or

$$\tilde{\phi}(\bar{r}) = \phi_a(\bar{r}) + \phi_m(\bar{r}) \qquad [5.2]$$

where $\bar{H}$ is given by

$$\bar{H} = -\nabla \tilde{\phi} \qquad [5.3]$$

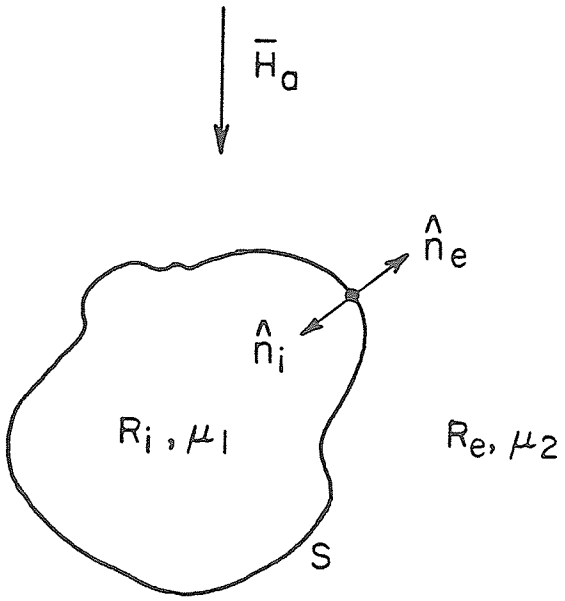

FIG. 5.1: Interface problem geometry

5.1 Integral Formulations for Scalar Potentials

The wide selection of boundary sources to suit the problem gives rise to at least three formulations that may be used. The following subsections discuss their origins and relative merits when $\mu_2 = \mu_0$ for free-space, and $\mu_1 = \mu\mu_0$ where μ is the relative permeability.

5.1.1 Simple-Layer Kernel

This formulation is derived from the use of a distribution of simple-layer polarization charges $\sigma(s)$ on S. The perturbation potential ϕ_m everywhere in R is given by

$$\phi_m(\bar{r}) = \frac{1}{\mu_0} \int_S G[\bar{r}|s'] \, \sigma(s')ds' \qquad [5.4]$$

where G is singular on S and requires special handling. The boundary conditions on S require that both

$$\tilde{\phi}_1 = \tilde{\phi}_2 \qquad [5.5]$$

and

$$\mu_1 \frac{\partial \tilde{\phi}_1}{\partial n_i} + \mu_2 \frac{\partial \tilde{\phi}_2}{\partial n_e} = 0 \qquad [5.6]$$

be satisfied. Since ϕ_m is harmonic in R and continuous across S, condition [5.5] is satisfied when $\phi_{a_1} = \phi_{a_2}$ on S (which is obvious). For flux continuity, consider the Neumann formulations of [5.4] taken along $\hat{n}_i$ and $\hat{n}_e$ such that

$$\frac{\partial \phi_{m_1}(s)}{\partial n_i} = \frac{1}{\mu_0} \int_S \frac{\partial G[s|s']}{\partial n_i} \sigma(s')ds' - \frac{\sigma(s)}{2\mu_0} \qquad [5.7]$$

and

$$\frac{\partial \phi_{m_2}(s)}{\partial n_e} = \frac{1}{\mu_0} \int_S \frac{\partial G[s|s']}{\partial n_e} \sigma(s')ds' - \frac{\sigma(s)}{2\mu_0} \qquad [5.8]$$

on S where the last term of each of the above expressions represents the jump in flux in crossing the boundary. Expanding [5.6] into component form, dividing throughout by μ_0, and recognizing that the normal derivative of ϕ_{a_1} and ϕ_{a_2} are identical, the result is the simplified interface condition

$$\mu \frac{\partial \phi_{m_1}}{\partial n_i} + \frac{\partial \phi_{m_2}}{\partial n_e} = (\mu - 1) \frac{\partial \phi_a}{\partial n_e} \qquad [5.9]$$

Substituting equations [5.7] and [5.8] into [5.9] and noting that the normal derivative of G in the $\hat{n}_i$ and $\hat{n}_e$ directions sum to zero, the following expression in terms of σ on S

$$\frac{1}{\mu_0}\int_S \frac{\partial G[s|s']}{\partial n}\,\sigma(s')ds' + \frac{(\mu + 1)}{(\mu - 1)}\,\frac{\sigma(s)}{2\mu_0} = H_{an} \qquad [5.10]$$

is obtained where subscripts have been dropped with the understanding that normals are directed along $\hat{n}_e$. The right-hand side of [5.10] represents the normal component of the applied field and is computed from

$$H_{an} = -\hat{n}\cdot\nabla\phi_a = -\frac{\partial\phi_a}{\partial n} \qquad [5.11]$$

This formulation is seen to be well-behaved even when $\mu \to \infty$. Once $\sigma(s)$ is known, ϕ_m everywhere may be computed from [5.4] and $\tilde{\phi}$ from [5.2].

5.1.2 Double-Layer Kernel in Terms of Partial Interface Potentials

This formulation expresses perturbation potential ϕ_m everywhere in R as a function of its values on S. Equations [4.16] and [4.17] may be used to obtain the following two equations

$$\phi_{m_1}(\bar{r}) = \int_S \{G[\bar{r}|s']\,\frac{\partial\phi_{m_1}}{\partial n'} - \phi_{m_1}\,\frac{\partial G[\bar{r}|s']}{\partial n'}\}\,ds' \quad ; \quad \bar{r}\in R_i \qquad [5.12]$$

$$\phi_{m_2}(\bar{r}) = -\int_S \{G[\bar{r}|s']\,\frac{\partial\phi_{m_2}}{\partial n'} - \phi_{m_2}\,\frac{\partial G[\bar{r}|s']}{\partial n'}\}\,ds' \quad ; \quad \bar{r}\in R_e \qquad [5.13]$$

the negative sign in the latter being due to the assigned normal being directed into R_e. With $\bar{r}\in S$ (*i.e.*, $|\gamma| = 2$), adding [5.13] to the product of μ and [5.12] gives

$$\frac{1}{2}[\mu\phi_{m_1}(s) + \phi_{m_2}(s)] = \int_S [\mu \frac{\partial\phi_{m_1}}{\partial n'} - \frac{\partial\phi_{m_2}}{\partial n'}] G[s|s']ds' - \int_S [\mu\phi_{m_1} - \phi_{m_2}] \frac{\partial G[s|s']}{\partial n'} ds'$$

[5.14]

Interface conditions demand that $\phi_{m_1} = \phi_{m_2}$ on S and [5.9] must hold. Therefore, [5.14] simplifies to

$$\int_S \frac{\partial G[s|s']}{\partial n'} \phi_m(s')ds' + \frac{(\mu + 1)}{(\mu - 1)} \frac{\phi_m(s)}{2} = \int_S G[s|s']H_{an}ds'$$

[5.15]

which retains the form of [5.10] except for the right-hand side which is considerably more involved. Computation of ϕ_m using equations [5.12] and [5.13] requires determination of $\frac{\partial\phi_m}{\partial n}$ on S. This requirement could be removed by eliminating the flux term, a procedure justified by the fact that $\phi_m(s)$ alone is sufficient to define ϕ_m everywhere in R. The steps in elimination involve writing [5.12] and [5.13] in each region and massaging them into a form that allows [5.9] to be invoked for simplification. The end result is given by

$$\phi_{m_1}(\bar{r}) = \frac{(\mu - 1)}{\mu} \int_S \{G[\bar{r}|s']H_{an}(s') - \phi_m(s') \frac{\partial G[r|s']}{\partial n'}\} ds' \quad ; \quad \bar{r} \in R_i$$

[5.16]

and

$$\phi_{m_2}(\bar{r}) = (\mu - 1) \int_S \{G[\bar{r}|s']H_{an}(s') - \phi_m(s') \frac{\partial G[\bar{r}|s']}{\partial n'}\} ds' \quad ; \quad \bar{r} \in R_e$$

[5.17]

two equations differing by a factor μ^{-1}! Denoting $\phi'_m(\bar{r})$ as

$$\phi'_m(\bar{r}) = (\mu - 1) \int_S \{G[\bar{r}|s']H_{an}(s') - \phi_m(s') \frac{\partial G[\bar{r}|s']}{\partial n'}\}ds' \quad ; \quad \bar{r} \in R_i + R_e, \quad \bar{r} \notin S$$

[5.18]

the total potential $\tilde{\phi}$ everywhere is given by

$$\tilde{\phi}(\bar{r}) = \begin{cases} \phi_a(\bar{r}) + \phi'_m(\bar{r}) & ; \quad \bar{r} \in R_e \\ \phi_a(s) + \phi_m(s) & ; \quad \bar{r} \in S \\ \phi_a(\bar{r}) + \frac{1}{\mu}\phi'_m(s) & ; \quad \bar{r} \in R_i \end{cases} \qquad [5.19]$$

5.1.3 Double-Layer Kernel in Terms of Total Interface Potentials

This formulation in terms of $\tilde{\phi}$ leads to a more compact expression than the previous. Consider ϕ_a which is harmonic in R_i and specifically satisfies Laplace's equation (since ϕ_a originates in R_e). Then Green's Theorem may be invoked to write

$$\frac{\phi_a(s)}{2} = \int_S \{G[s|s'] \frac{\partial \phi_a(s')}{\partial n'} - \phi_a(s') \frac{\partial G[s|s']}{\partial n'}\} ds' \qquad [5.20]$$

on S. Multiplying [5.20] by $(\mu - 1)$ and rearranging it into a form comparable with [5.15], the result is

$$(\mu - 1) \int_S \frac{\partial G[s|s']}{\partial n'} \phi_a(s') ds' + \frac{(\mu - 1)}{2} \phi_a(s) = -(\mu - 1) \int_S G[s|s'] H_{an} ds' \qquad [5.21]$$

Adding [5.15] to [5.21] and rearranging, the resultant expression

$$\int_S \frac{\partial G[s|s']}{\partial n'} \tilde{\phi}(s') ds' + \frac{(\mu + 1)}{(\mu - 1)} \frac{\tilde{\phi}(s)}{2} = \frac{1}{(\mu - 1)} \phi_a(s) \qquad [5.22]$$

is the formulation in terms of total potentials $\tilde{\phi}$ on S. Once $\tilde{\phi}$ is ascertained, equation [5.20] written in R_i or R_e could be used in conjunction with [5.16] or [5.17] to obtain the compact expression

$$\tilde{\phi}(\bar{r}) = \begin{cases} \phi_a(\bar{r}) + \phi'_m(\bar{r}) & ; \quad \bar{r} \in R_e \\ \frac{1}{\mu}\phi_a(\bar{r}) + \frac{1}{\mu}\phi'_m(\bar{r}) & ; \quad \bar{r} \in R_i \end{cases} \qquad [5.23]$$

where

$$\phi'_m(\bar{r}) = -(\mu - 1)\int_S \frac{\partial G[\bar{r}|s']}{\partial n'}\tilde{\phi}(s')ds' \quad ; \quad \bar{r} \in R_e + R_i \quad \bar{r} \notin S \qquad [5.24]$$

The equations derived in [5.10], [5.15] and [5.22] are three formulations of the same problem in terms of second kind Fredholm integrals with fairly well-behaved kernels. By replacing $\frac{\sigma}{\mu_0}$ by M_n, the normal component of equivalent magnetization sources, the matrix of [5.10] is seen to be the transpose of [5.15] and [5.22]. The most noticeable difference is in the excitation function where [5.10] and [5.22] are simple and compact. In the case of [5.15] a double-surface integral has to be evaluated. Besides additional time in matrix fill, the kernel also requires special treatment since G is singular on S. Consequently, this formulation is not a viable alternative. The main difference between [5.10] and [5.22] lies in the computation of $\tilde{\phi}$ once the equations have been solved for boundary sources. With the former, the expression for ϕ_m is valid everywhere without reservation but the same cannot be said for the latter. As such, numerical inconsistencies with respect to sign changes may arise for $\bar{r}$ close to the interface. The formulation in terms of ϕ_m on S has another disadvantage when it comes to field determination. From inspection of [5.18], $\phi_m(\bar{r})$ is dependent on the product of μ with the difference between two small values (Jeng, 1977). In the limit as $\mu \to \infty$, the error in ϕ_m

computation is magnified especially for the exterior fields. The interior expression is more stable due to the added factor of μ^{-1}.

The choice of which of [5.10] or [5.22] to implement depends on the parameter of interest. If interface potentials are important, then [5.22] would be preferred since $\tilde{\phi}$ is the independent variable. But if field definition within R is paramount, then [5.10] would be a better choice due to the continuity of ϕ across S.

5.2 Permeable Square Cylinder in a Uniform $\bar{H}$-Field

This example entails a two-dimensional analysis of a square, permeable cylinder oriented as shown in Figure 5.2. The uniform $\bar{H}_a$-field is directed along the positive y-axis by setting $\phi_a = -y$. Using quarter-plane symmetry, only the fourth quadrant need to be addressed. However, to take advantage of the symmetric Green's function of [4.22], the problem is actually solved in the positive quadrant. The desired results are then obtained with a change in polarity.

Galerkin's method is applied individually to equations [5.10], [5.15] and [5.22] to solve this problem. Each of these equations is seen to be of the second kind with a well-behaved kernel. In particular, the normal derivative of Green's function is

$$\frac{\partial G}{\partial n} = \hat{n} \cdot \nabla G = -\frac{1}{2\pi} \frac{\cos(\hat{n}, \bar{r} - r')}{|\bar{r} - \bar{r}'|} \qquad [5.25]$$

which is finite in the limit as $\bar{r} \to \bar{r}'$ since the argument of the cosine function tends to $\frac{\pi}{2}$. As a result, only the Gauss-Legendre weight need be used for integration over the primed variable.

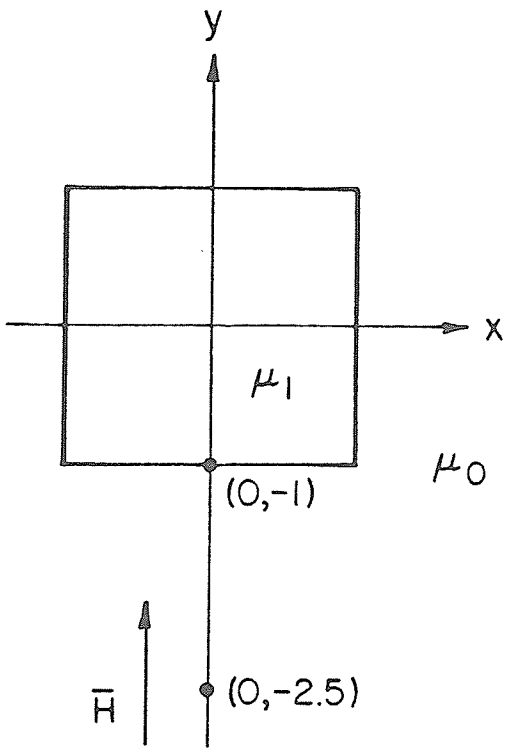

FIG. 5.2: Square permeable cylinder in uniform $\bar{H}$-field

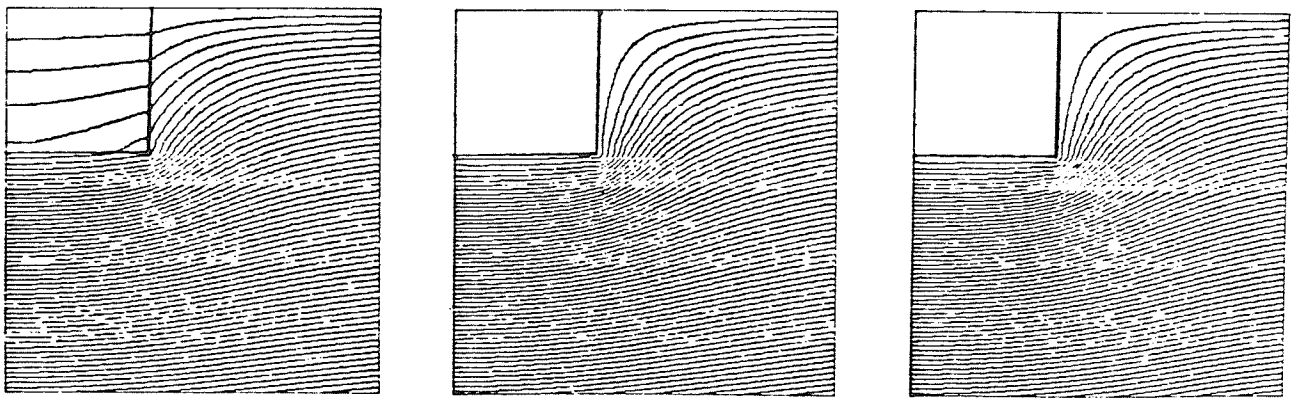

(a) (b) (c)

FIG. 5.3: Potential contours in uniform magnetic field
(a) μ = 10;
(b) μ = 100;
(c) μ = 1000

The BEM model consists of 4 cubic elements involving 13 unknowns. Denoting the formulations of [5.10], [5.15] and [5.22] by F_1, F_2 and F_3 respectively, the potential $\tilde{\phi}$ computed at coordinate positions $(0, -1)$ and $(0, -2.5)$, are compared in Table 5.1 for different values of μ.

TABLE 5.1: Computed potentials $\tilde{\phi}$

	$-\tilde{\phi}(0, -1)$			$-\tilde{\phi}(0, -2.5)$		
μ	F_1	F_2	F_3	F_1	F_2	F_3
1	1.0	1.0	1.0	2.5	2.5	2.5
2	.649	.649	.648	2.332	2.332	2.332
10	.175	.174	.173	2.074	2.070	2.074
10^2	$.208 \times 10^{-1}$	$.199 \times 10^{-1}$	$.188 \times 10^{-1}$	1.979	1.929	1.979
10^3	$.383 \times 10^{-2}$	$.293 \times 10^{-2}$	$.190 \times 10^{-2}$	1.968	1.457	1.968

For the situation $\mu = 1$, the interface does not exist, *i.e.*, F_1 and F_2 have only the trivial solution for M_n and ϕ_m, respectively. F_3 has the solution $\tilde{\phi} = \phi_a$ as expected. Therefore, the exact values of $\tilde{\phi}(0, -1)$ and $\tilde{\phi}(0, -2.5)$ are returned in the first row. As μ is increased, the results for F_2 in the exterior region, deteriorate in comparison to F_1 and F_3. Also, $\tilde{\phi}$ computed close to the boundary S have negative signs especially for large μ. This discrepancy is due to the formulation [5.18] used to recover ϕ_m. As $\mu \to \infty$, the $\bar{H}$-field in the cylinder tends to zero so that for [5.18] to hold true, very precise field cancellation is required between the applied and polarization components.

Potentials on the surface are more aptly computed by F_3 since $\tilde{\phi}$ is the independent variable. F_2 requires the summation of ϕ_m and ϕ_a on S. The difference in the results of F_2 and F_3 is attributed to the inaccuracy of solution of ϕ_m — the errors being introduced in the computation of the excitation vector. Of the three, F_1 is the least accurate in terms of surface potentials due to the crude recovery scheme used. Theoretically [5.4] is singular on S, so that a sectioning philosophy in line with that described in Chapter III is required to ensure that the observation point in question is approached in the proper manner. However, the usefulness of such a scheme is difficult to justify especially when F_3 could be used so effectively. In comparing the accuracy of computed exterior $\tilde{\phi}$, no difference can be detected between F_1 and F_3. Thus, this observation reiterates the theoretical claim that F_1 is more viable in terms of computational economy. No special software is needed to determine the location of the observation point since [5.4] is freely applicable everywhere except on S. Equipotential plots of $\tilde{\phi}$ computed using F_1 and 7-point quadrature are shown in Figure 5.3 previously reported in Lean & Wexler (1981b).

5.3 A Two-Dimensional Formulation for Vector Potentials

A vector formulated problem is posed by a current coil radiating through a permeable body into free-space. In the case of a magnetic recording head where the length is much greater than cross-section dimensions, a two-dimensional analysis is preferred. Coupled with the fact that head geometry and configuration frequently facilitate usage of rotational symmetry, most practical problems in this context are adequately handled with a two-dimensional analysis. As such, the following

derivation is for the z-component of magnetic vector potential A_z and its field effects.

Again citing linearity of Maxwell's equations, the effect of a current coil radiating through a permeable body into air, may be simulated by the superposition of (a) the current coil alone radiating in air; and (b) a distribution of magnetic sources that hugs the geometry of the body. The component of vector potential $\bar{A}$ due to a z-directed current density is given by

$$A_z^J(\bar{r}) = \mu_0 \int_{R'} G[\bar{r}|R'] \, J_z(R')dR' \quad ; \quad \bar{r} \in R_1 + R_2 \qquad [5.26]$$

where R', R_1 and R_2 denote conductor cross-section, head cross-section and free space, respectively. Using a simple-layer kernel formulation for the sources, the following equation may be written separately for R_1 and R_2

$$A_z^M(\bar{r}) = \int_S G[\bar{r}|s'] \, M_t(s')ds' \qquad [5.27]$$

where M_t denotes the tangential component of the magnetization on S caused by B_{tan} due to the current source. The total potential $\tilde{A}_z$ is then given by

$$\tilde{A}_z(\bar{r}) = A_z^J(\bar{r}) + A_z^M(\bar{r}) \qquad [5.28]$$

Interface conditions on S require continuity of normal component of $\bar{B}$ ($= \nabla \times \bar{A}$) and tangential component of $\bar{H}$ ($= \frac{1}{\mu} \bar{B}$), or

$$\tilde{A}_{z_1} = \tilde{A}_{z_2} \qquad [5.29]$$

and $$\frac{1}{\mu_1}\frac{\partial \tilde{A}_{z_1}}{\partial n} = \frac{1}{\mu_2}\frac{\partial \tilde{A}_{z_2}}{\partial n} \qquad [5.30]$$

Enforcement of [5.30] with $\mu = \frac{\mu_1}{\mu_2}$ leads to the reduced interface condition

$$\frac{\partial A^M_{z_1}}{\partial n_i} + \mu \frac{\partial A^M_{z_2}}{\partial n_e} = (\mu - 1)\frac{\partial A^J_z}{\partial n_e} \qquad [5.31]$$

where subscripts denote directions of normals. Substituting the appropriate normal derivatives of [5.27] into the above and rearranging, the result is

$$\int_S \frac{\partial G[s|s']}{\partial n} M_t(s')ds' + \frac{(1+\mu)}{(1-\mu)}\frac{M_t(s)}{2} = -\frac{\partial A^J_z(s)}{\partial n} \qquad [5.32]$$

a second kind Fredholm integral in terms of $M_t(s)$. The excitation is provided by the current coil and is computed from

$$\frac{\partial A^J_z(s)}{\partial n} = \mu_0 \int_{R'} \frac{\partial G[s|R']}{\partial n} J_z(R')dR' \quad ; \quad s \in S \qquad [5.33]$$

Once [5.32] is solved, $\tilde{A}_z$ everywhere is calculated from [5.26], [5.27] and [5.28]. In practice, the parameters of interest to engineers are the downtrack (B_x) and vertical (B_y) fields since they are intimately linked to magnetic recording processes. B_x and $-B_y$ are in turn, the derivatives of [5.28] with respect to the y and x variables. In particular, B_x and B_y are given by

$$B_x(\bar{r}) = \frac{\partial A^M_z(\bar{r})}{\partial y} + \frac{\partial A^M_z(\bar{r})}{\partial y} \qquad [5.34]$$

and $$B_y(\bar{r}) = -\frac{\partial A^M_z(\bar{r})}{\partial x} - \frac{\partial A^J_z(\bar{r})}{\partial x} \qquad [5.35]$$

These derivatives may be carried within the integral since they are with respect to the unprimed variables. As a consequence, the algorithm is neat and compact when compared to a partial differential equation solution where node interpolation is necessary.

5.4 The Magnetic Recording Head Problem

Equation [5.32] is solved using Galerkin's method for the magnetization sources M_t. The Green's function used is given by

$$G[\bar{r}|\bar{r}'] = -\frac{1}{2\pi} \ell n|\bar{r} - \bar{r}'| + \frac{1}{2\pi} \ell n|\bar{r}_R - \bar{r}'| \qquad [5.36]$$

where the last term on the right-hand side is included for the same reason as in Section 4.3. The BEM models of the conductor and head cross-section are shown in Figure 5.4. A constant current density of $.03A/micron^2$ flows in the conductor which is modelled by 4 linear triangular elements. The vector potentials due to the conductor are computed using 16-point quadrature over each element. A basic configuration for the head cross-section is the 8 element model of Figure 5.4(c), with the facility to increase the degree of interpolation from a linear (8 nodes) to a quartic (32 nodes) approximation. Figures 5.5 and 5.6 show the calculated vertical and downtrack fields at distances of .5, 1, 2, and 4 microns beneath the head. The bumps in each curve at approximately $|x| \simeq 2$ micron are not observed until a cubic approximation is used. This is expected due to the rapid undulation of the field.

In the calculation of vector potential due to magnetization sources using [5.27], a logarithmic singularity is evident on the head boundary. However, in this analysis, no special scheme is specially used to acknowledge the singularity. Three-dimensional representations of

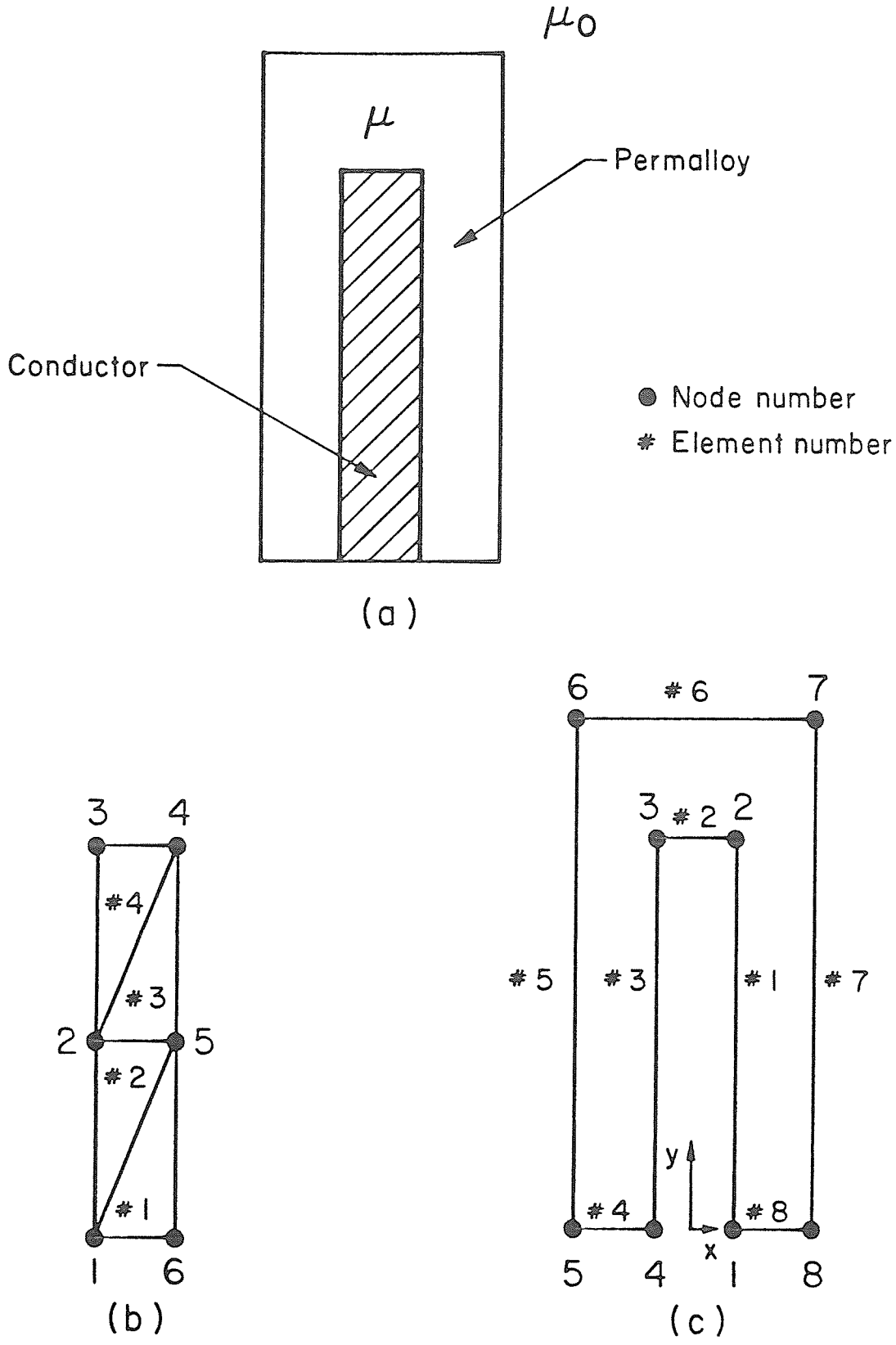

FIG. 5.4: Magnetic recording head:
(a) cross-section;
(b) BEM model of conductor; and
(c) BEM model of head cross-section

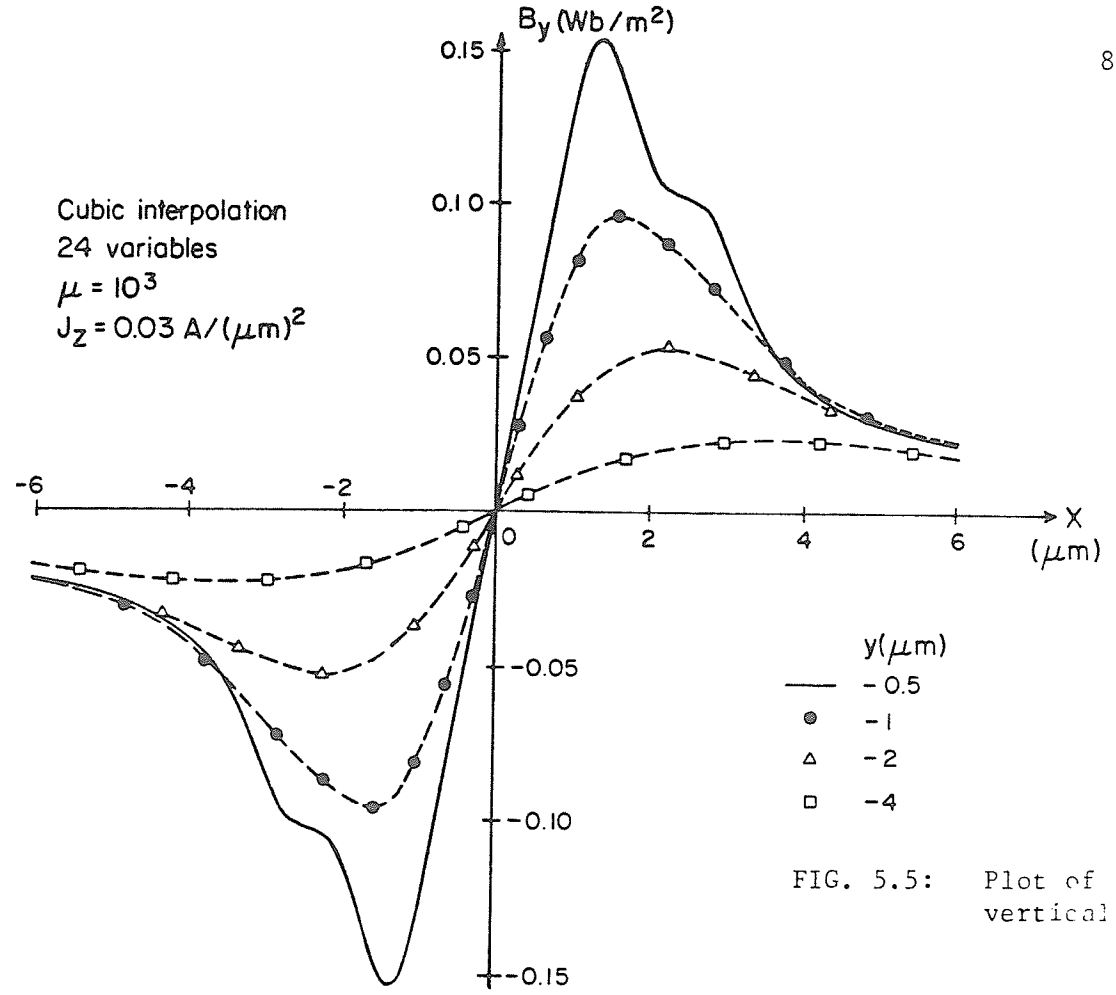

FIG. 5.5: Plot of vertical field

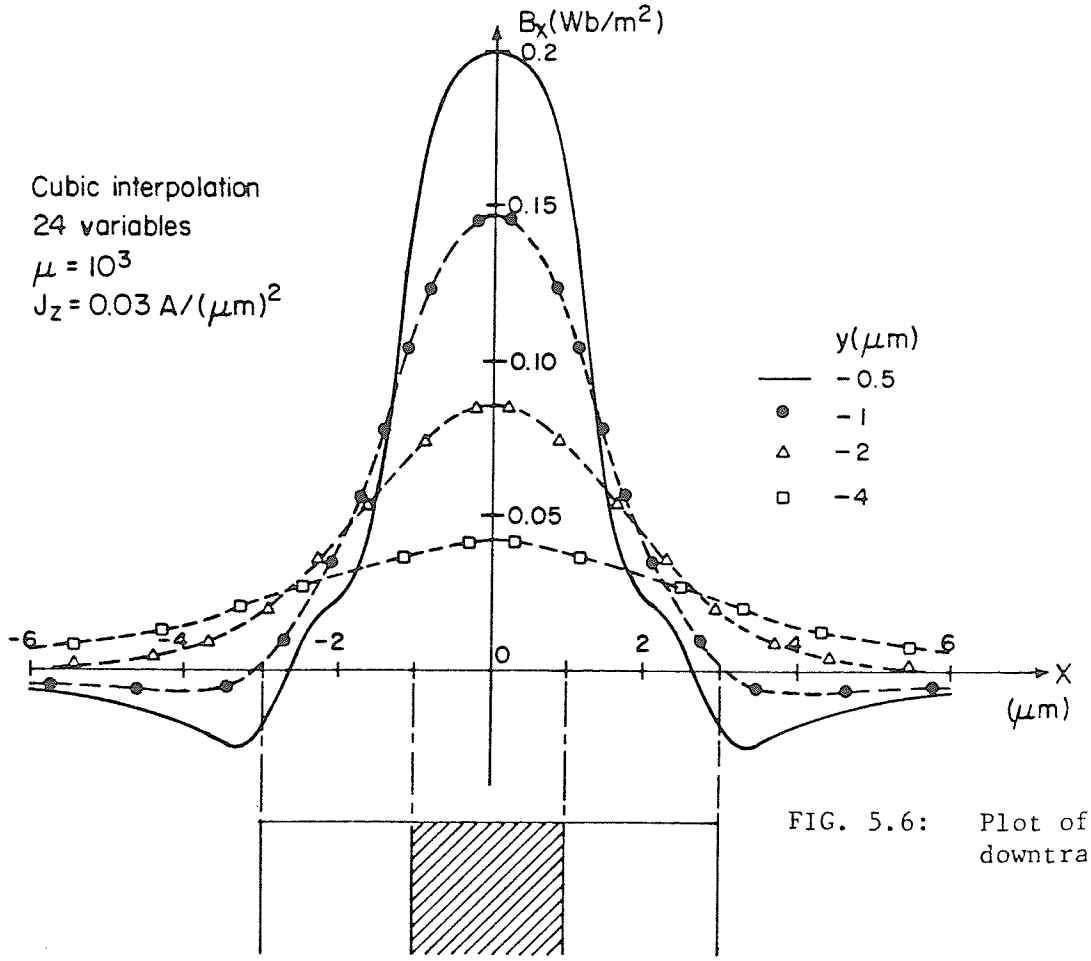

FIG. 5.6: Plot of downtrack field

FIG. 5.7: Three-dimensional representation of vector potential A_z:

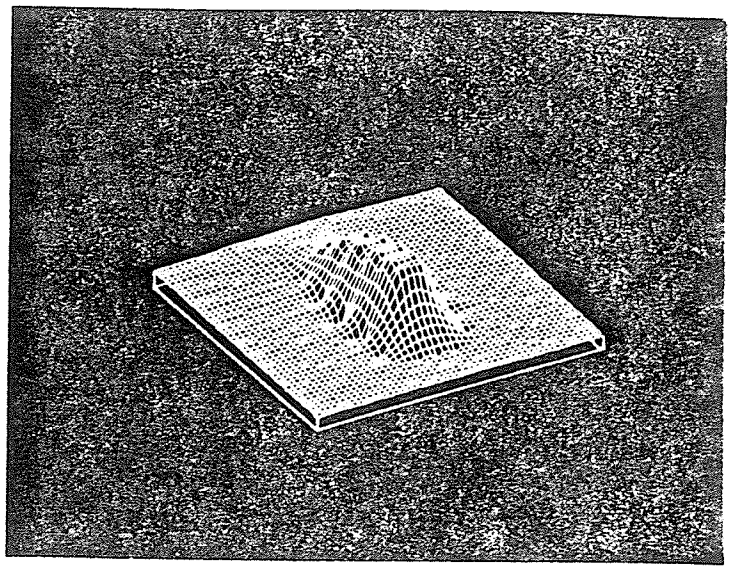

(a) due to magnetization source

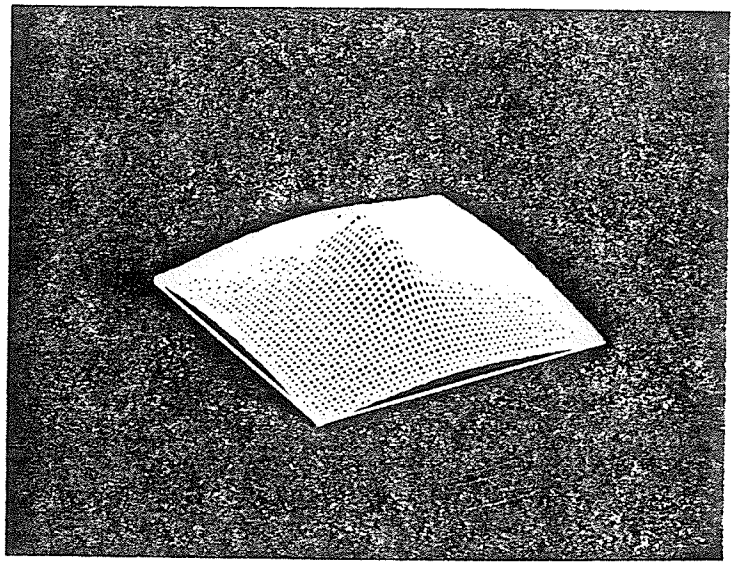

(b) due to current conductor

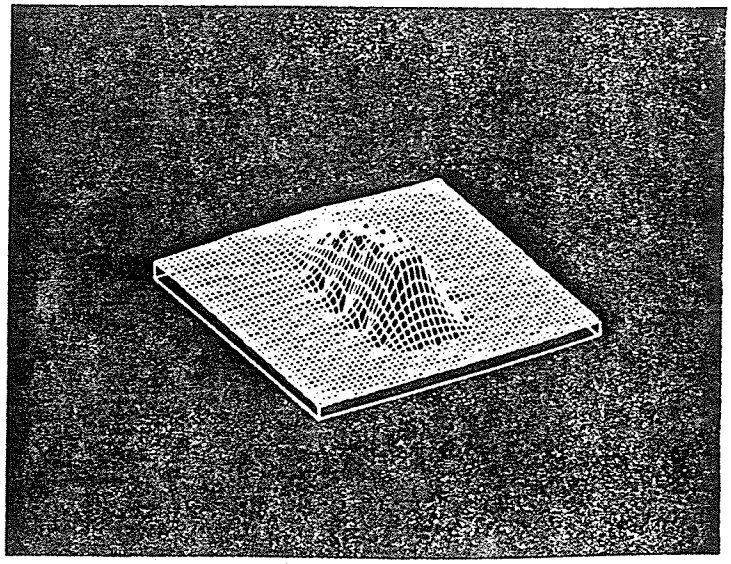

(c) due to sum of (a) and (b)

the vector potentials are shown in Figure 5.7. The isometric view pertains to the head oriented with the open-end facing inwards. In Figure 5.7(a), the undulations observed correspond to the periphery of the head. It appears that the crude recovery scheme used for A_z^M on the head lead to the imprecision alluded to in a previous example (Section 5.2). Increasing the quadrature order is seen to ameliorate the problem though not handling it explicitly. Since B_x and B_y fields, which are independent of the companion term in [5.36], are of primary interest, this scheme will be the most economical and versatile to use. A suitable formulation can be derived using the concept of Section 5.1.3 if A_z on the head boundary is to be determined accurately.

Figures 5.7(b) and (c) show the vector potentials due to the current coil alone, and the resultant total potentials due to both (a) and (b). The features of Figure 5.7(a) are retained in (c) because of the observed order of magnitude difference in their values. Each of the plots are done separately, each with a different scaling factor built into an interpolation algorithm that confines the plot within the screen of the Tektronix 4013 DVST. Thus, this essentially makes it difficult to visually sum (a) and (b) to obtain (c).

VI. ELECTROMAGNETIC SCATTERING PROBLEMS

The time-harmonic response of electromagnetic waves in the presence of a scatterer depends on the configuration and material constitution of the object; the propagation frequency, polarization, and angle of incidence of the impinging field; and the far-field observation angle. Classical solutions involving expansions of cylindrical (two-dimensional), spherical and spheroidal wave functions, exist only for a limited class of geometries where separation of variables may be practiced. In the low-frequency or *Rayleigh region*, analytic solutions are obtained in the form of convergent power series expansions (Kleinman, 1965). At high-frequencies, asymptotic techniques such as Ray or Physical Optics (PO), Geometrical Optics (GO) (Koujoumjian, 1966), and the Geometrical Theory of Diffraction (GTD) (Keller, 1962), are necessary. Corresponding techniques for the transition or *resonance* range include modal expansion (*e.g.*, Garbacz, 1965), and conformal transforms (Shafai, 1969).

With the advent of the digital computer came the numerical modes of solution (Mei & Van Bladel, 1963) — based on moment methods (Harrington, 1968) with modelling strategy tackled on two fronts: wire-grid and solid-surface techniques. Undoubtedly, the modelling of antenna configurations as wire-like radiating structures precipitated the use of the wire-grid approximation (Richmond, 1966). Its application to solid-surface geometries seem a natural extension and does work well at sufficiently low frequencies when grid-length is short compared to the wavelength (Lin & Richmond, 1975). The other alternative was initially introduced as patch collocation.

Traditional preference has been to use the electric field integral equation (EFIE) for wire structures and the magnetic field integral equation (MFIE) for solid surfaces. Part of the reason for the first preference is because the MFIE kernel has a term involving the vector product of surface current $\bar{J}_s$ with the gradient of the Green's function $\nabla'G$ so that difficulties arise when the included angle becomes small. The EFIE is ideally suited since the axial currents are assumed and constrained to flow along the wire. However, the strongly singular kernel has been a deterent to many practitioners in this area. The MFIE has a better-behaved kernel but is prone to internal resonance problems and deteriorates as a viable alternative for scatterers of vanishing volume due to geometrical factors in the integrand. One technique for coping with the interior resonance problem is to apply the extended boundary condition (EBC) of Waterman (1965, 1973) involving vector eigenfunction expansions of the Helmholtz equation. Other recent contributions and improvements to the EBC include Al-Badwaihy & Yen (1975), and Morita (1979). A second method involves the coupling of the MFIE to the EFIE (Mitzner, 1968) to effectively suppress the resonance effect. Another alternative is the artificial suppression of interior resonances by setting some points in the interior to have vanishing fields, thus constraining the system of linear equations to have the trivial solution within. One disadvantage is in the arbitrarities of such a constraint — the null locations must coincide in position with a non-zero value of the resonating mode in order for the technique to work. Thus, prior knowledge of modal locations are necessary in this application. A final method involves the method of modal expansions previously alluded to.

The size of the integral equation-generated matrix that can be accomodated on a computer, limits the dimension of the scatterer in terms of the wavelength of the illuminating field. This core limitation dictates the number of variables that can be effectively handled at any frequency. Hybrid techniques that incorporate the GTD with traditional moment methods (Burnside et al, 1975; Thiele & Newhouse, 1975) have met with some success. Any scheme that leads to economy with respect to the number of variables, will be a definite asset. This study will be concerned with the scattering of electromagnetic waves from perfectly conducting boundaries.

6.1 Two-Dimensional Integral Formulations

Maxwell's equations in space-time domain may be restated in the space-frequency domain with suppressed $e^{j\omega t}$ time dependence. The $\bar{E}$ and $\bar{H}$ field wave equations for a source-free media

$$\begin{aligned} \nabla \times \nabla \times \bar{E} - k^2\bar{E} &= 0 \\ \nabla \times \nabla \times \bar{H} - k^2\bar{H} &= 0 \end{aligned} \qquad [6.1]$$

reduce to

$$\begin{aligned} (\nabla^2 + k^2)\,\bar{E} &= 0 \\ (\nabla^2 + k^2)\,\bar{H} &= 0 \end{aligned} \qquad [6.2]$$

for a divergenceless region with wave number $k = \omega\sqrt{\mu\varepsilon} = 2\pi\sqrt{\lambda}$. Defining in general terms $\psi(\bar{r})$ and $G[\bar{r}|\bar{r}']$ to be two potential functions in R that satisfy the wave equations

$$(\nabla^2 + k^2)\ \psi(\bar{r}) \;=\; 0 \qquad [6.3]$$

where $\psi(\bar{r}) \to 0$ as $|\bar{r}| \to \infty$

and $$(\nabla^2 + k^2)\ G[\bar{r}|\bar{r}'] \;=\; -\delta(\bar{r} - \bar{r}') \qquad [6.4]$$

where $G[\bar{r}|\bar{r}'] \to 0$ as $|\bar{r} - \bar{r}'| \to \infty$

subject to the boundary condition

$$\lim_{r \to \infty} r\left[\frac{\partial \psi}{\partial r} + jk\psi\right] \;=\; 0 \qquad [6.5]$$

the scalar form of Green's Theorem may be invoked to obtain

$$\psi(\bar{r}) \;=\; \gamma \int_{S + S_\infty} \{G[\bar{r}|s'] \frac{\partial \psi(s')}{\partial n'} - \psi(s') \frac{\partial G[\bar{r}|s']}{\partial n'}\} ds' \qquad [6.6]$$

given that γ is the factor defined in [4.17]. From the radiation (Sommerfeld) condition, the incident field ψ^i (plane wave in the classical radar problem) is the accumulated effect on the boundary at infinity S_∞. Since total field $\psi(\bar{r}) = \psi^i(\bar{r}) + \psi^s(\bar{r})$, the scattered field is given by

$$\psi^s(\bar{r}) \;=\; -\int_S \{G[\bar{r}|s'] \frac{\partial \psi(s')}{\partial n'} - \psi(s') \frac{\partial G[\bar{r}|s']}{\partial n'}\} ds' \;;\; \bar{r} \in R \qquad [6.7]$$

The remaining portion of this section will be concerned with the two-dimensional problem where the z-component of the field is invariant in that direction. For oblique plane wave incidence, the incident field is given by

$$\psi^i(x,y,z) = A_0 \sin\theta \, e^{jk\sin\theta(x\cos\phi_0 + y\sin\phi_0)} \, e^{jk\cos\theta z} \qquad [6.8]$$

where θ and ϕ_0 are the elevation and azimuthal angles, respectively (Figure 6.1). Denoting the transverse component of the wave number as $k_t = k \sin\theta = \sqrt{k^2 - k_z^2}$ where $k_z = k \cos\theta$, and evaluating on the $z = 0$ plane, [6.8] reduces to

$$\psi^i(x,y,0) = A_0 \sin\theta \, e^{jk_t(x\cos\phi_0 + y\sin\phi_0)} \qquad [6.9]$$

6.1.1 TM Wave Incidence

This case is obtained by setting $\psi(\bar{r}) = E_z(\bar{r})$ in equations [6.6] and [6.7]. Thus

$$E_z(\bar{r}) = -\gamma\{E_z^i(\bar{r}) - \int_S [G[\bar{r}|s'] \frac{\partial E_z}{\partial n'} - E_z \frac{\partial G[\bar{r}|s']}{\partial n'}]ds'\} \qquad [6.10]$$

Enforcing the boundary condition that E_{tan} vanish on S and setting

$$\left.\frac{\partial E_z}{\partial n'}\right|_S = j\omega\mu_0 J_z = \left. j\omega\mu_0 H_\phi\right|_S \qquad [6.11]$$

results in the Fredholm integral of the first kind

$$\frac{k_t}{4} \int_S H_0^{(2)} (k_t|\bar{r} - \bar{r}'|) \, J_z(s') \, ds' = E_z^i(s) \qquad [6.12]$$

in J_z, the longitudinal component of current density. Implicit in [6.12] is the Green's function defined by

$$G[\bar{r}|\bar{r}'] = \frac{-j}{4} H_0^{(2)} (k_t|\bar{r} - \bar{r}'|) \qquad [6.13]$$

and the normalization of E_z^i to unity with respect to free-space impedance η. Once J_z is known, the scattered field is obtained from

$$E_z^s(\bar{r}) = -\frac{k_t}{4}\int_S H_0^{(2)}(k_t|\bar{r}-s'|)\, J_z(s')\, ds' \qquad [6.14]$$

and hence the total field E_z by the expression

$$E_z(\bar{r}) = E_z^i(\bar{r}) + E_z^s(\bar{r}) \qquad [6.15]$$

An alternative form of [6.12] can be obtained by starting from the normal derivative of [6.10] on S thereby resulting in

$$-\frac{k_t^2}{4}\int_S H_1^{(2)}(k_t|\bar{r}-\bar{r}'|)\cos(\hat{n},\ \bar{r}-\bar{r}')\, J_z(s')ds' + \frac{1}{2}jk_t\, J_z(s) = \frac{\partial E_z^i(s)}{\partial n} \qquad [6.16]$$

with a better behaved kernel (Bolomey & Tabbara, 1973). Far-field quantities are computed using the asymptotic expansion of the Hankel function

$$H_0^{(2)}(k_t r) \xrightarrow[k_t r \to \infty]{} \sqrt{\frac{2j}{\pi k_t r}}\; e^{-jk_t r} \cdot e^{jk_t\, \hat{r}\cdot\bar{r}'} \qquad [6.17]$$

In particular, the radar cross-section (RCS) denoted by σ_{TM} is defined as

$$\sigma_{TM}(\phi) = \lim_{r\to\infty} 2\pi r \frac{|E_z^s(\bar{r})|^2}{|E_z^i(\bar{r})|^2} \qquad [6.18]$$

so that using [6.17] for the kernel of [6.14], the eventual form is

$$\sigma_{TM}(\phi) = \frac{k_t}{4\sin^2\theta}\left[\int_S e^{jk_t\, \hat{r}\cdot\bar{r}'}\, J_z(s')ds'\right]^2 \qquad [6.19]$$

dependent only on bistatic angle ϕ.

6.1.2 TE Wave Incidence

This mode of incidence corresponds to setting $\psi(\bar{r}) = H_z(\bar{r})$ in equations [6.6] and [6.7], *i.e.*

$$H_z(\bar{r}) = -\gamma\{H_z^i(\bar{r}) - \int_S [G[\bar{r}|s'] \frac{\partial H_z}{\partial n'} - H_z \frac{\partial G[\bar{r}|s']}{\partial n'}]ds'\} \quad [6.20]$$

Enforcing the boundary condition that $\frac{\partial H_z}{\partial n} = -j\omega\varepsilon_0 E_\phi = 0$ on S, and setting $J_\phi = -H_z(s)$, [6.20] simplifies to

$$\frac{jk_t}{4}\int_S H_1^{(2)}(k_t|\bar{r} - \bar{r}'|)\cos(\hat{n}, \bar{r} - \bar{r}')\, J_\phi(s')ds' + \frac{1}{2} J_\phi(s) = -H_z^i(s) \quad [6.21]$$

a Fredholm integral of the second kind for J_ϕ, the transverse component of current density. Once J_ϕ is ascertained, the scattered field is calculated from

$$H_z^s(\bar{r}) = \frac{jk_t}{4}\int_S H_1^{(2)}(k_t|\bar{r} - s'|)\cos(\hat{n}, \bar{r} - s')\, J_\phi(s')ds' \quad [6.22]$$

and hence total field H_z from

$$H_z(\bar{r}) = H_z^i(\bar{r}) + H_z^s(\bar{r}) \quad ; \quad \bar{r} \in R \quad [6.23]$$

except on S where H_z is given by

$$H_z(s) = 2[H_z^i(s) + H_z^s(s)] \quad [6.24]$$

Using the asymptotic form of the first order Hankel function

$$H_1^{(2)}(k_t r) \xrightarrow[k_t r \to \infty]{} \sqrt{\frac{2j}{\pi k_t r}}\, j^{-jk_t r} \cdot e^{jk_t \hat{r} \cdot \bar{r}'} \quad [6.25]$$

the scattering cross-section defined as

$$\sigma_{TE}(\phi) = \lim_{r \to \infty} 2\pi r \frac{|H_z^s(\bar{r})|^2}{|H_z^i(\bar{r})|^2} \qquad [6.26]$$

is now expressible as

$$\sigma_{TE}(\phi) = \frac{k_t}{4\sin^2\theta} \left[\int_S e^{jk_t \hat{r} \cdot \bar{r}'} (\hat{n}' \cdot \hat{r}) J_\phi(s')ds'\right]^2 \qquad [6.27]$$

6.2 Scattering from the Perfectly Conducting Circular Cylinder

The integral formulations given in equations [6.12] and [6.21] representing TM and TE incidences respectively, are solved using Galerkin's method for a circular cylinder of radius a. The kernel of [6.12] has a logarithmic singularity of the imaginary component and is treated in the manner described in Subsection 3.2.1. As for that of [6.21], the kernel is finite in the limit as $s \to s'$ so that a Gauss-Legendre quadrature is used for integration with respect to the present variable. Portions of the results that follow have previously been published in Lean & Wexler (1981a).

The BEM model used is shown in Figure 6.2 and consists of 4 quartic elements totalling 16 unknowns. With source symmetry, this problem can actually be solved with 9 variables. Figures 6.3 and 6.4 show the induced surface currents and radar cross-sections for both TE and TM normal ($\theta = 90°$) incidences at $ka = 1.6$ using 6-point quadrature. They exhibit almost no deviation from the results published by Oshiro & Su (1965). For the explicit purpose of output-data verification, special attention is paid to the issues pertaining to: (i) low-frequency performance; (ii) upper-frequency limitation; and (iii) near and far-field computation.

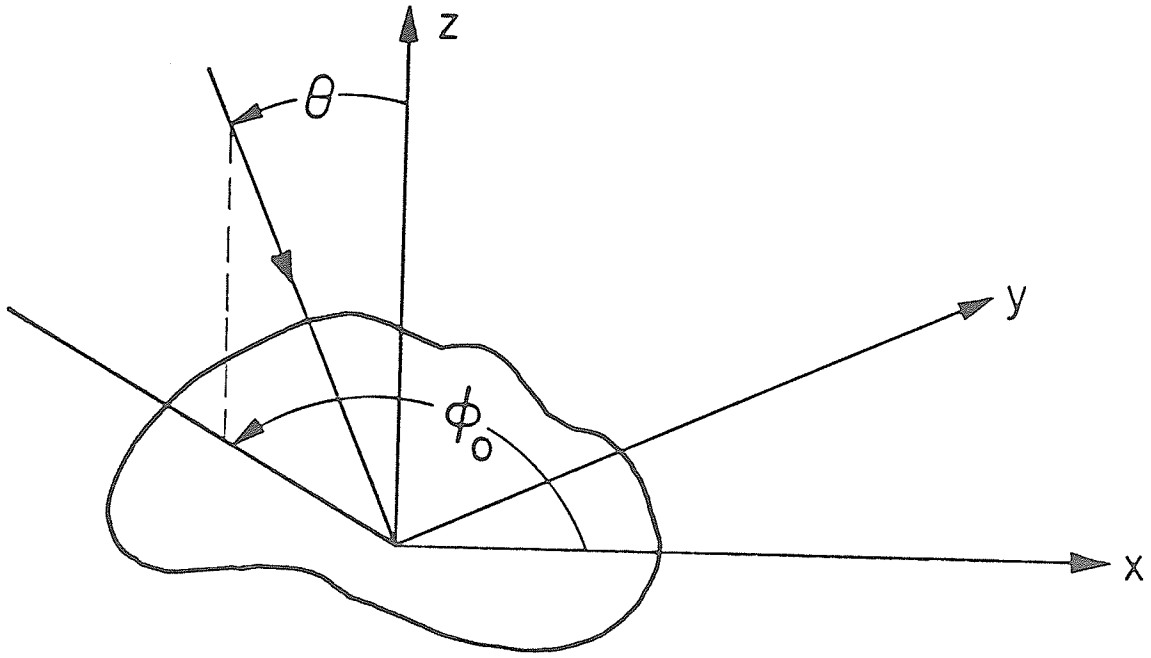

FIG. 6.1: Scatterer problem geometry

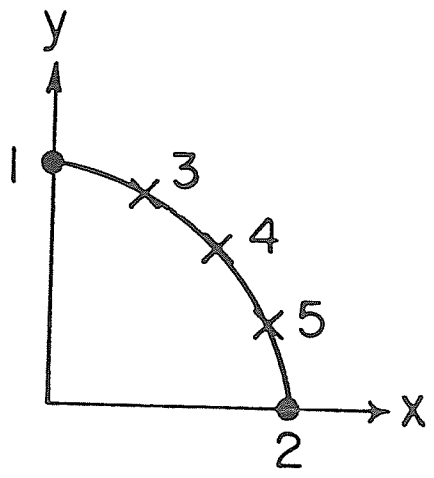

4 quartic elements
16 nodes

FIG. 6.2: BEM model of cylinder - first quadrant

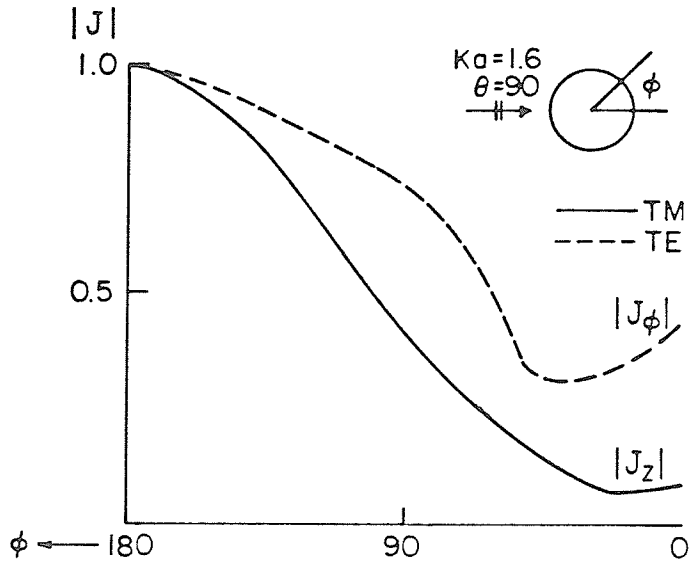

FIG. 6.3: Induced surface currents

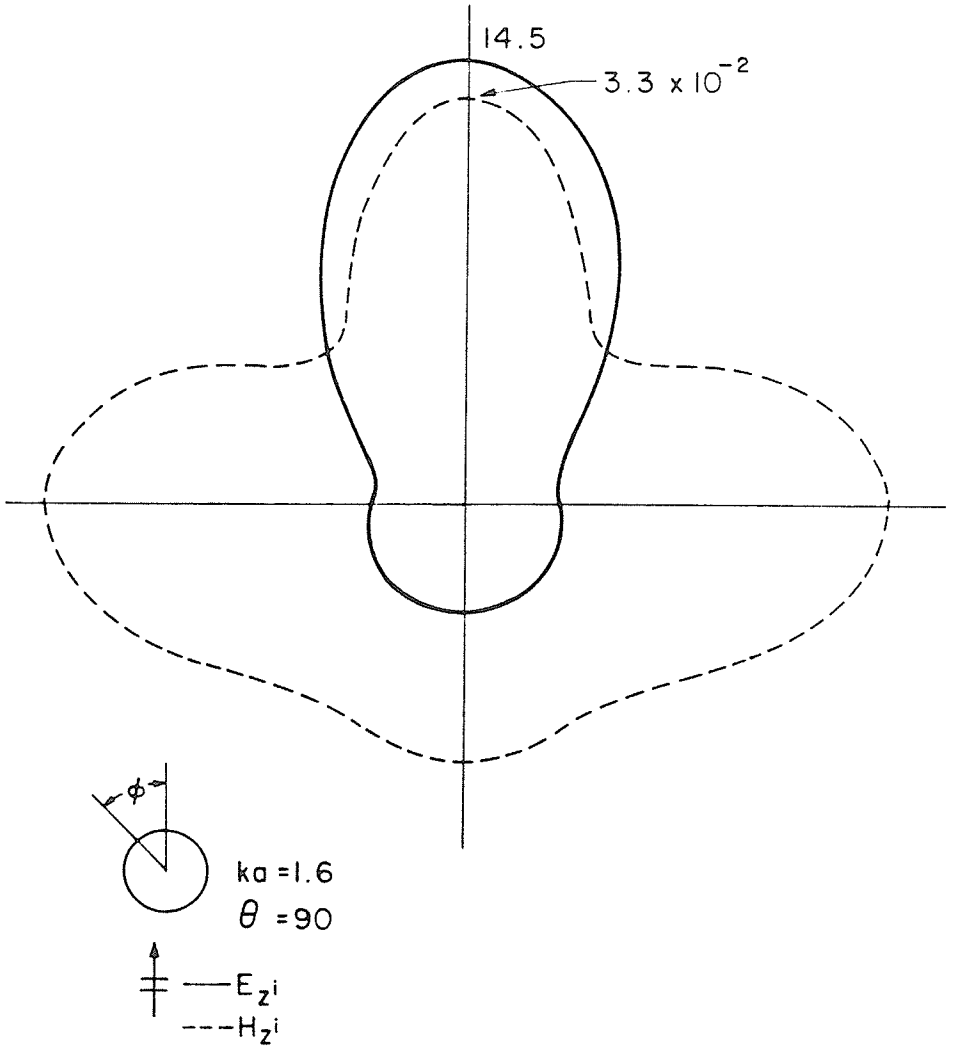

FIG. 6.4: Polar plot of bistatic cross-section

(i) Low-frequency performance

Analytic expressions for radar cross-sections of circular cylinders, obtained analytically from small argument series expansion, are given by Mullin *et al* (1965) as

$$\sigma_{TE}(\phi) = \frac{\pi^2 k^3 a^4}{4} [1 + 2\cos\phi]^2 \qquad [6.28]$$

and

$$\sigma_{TM}(\phi) = \frac{\pi^2}{k} \left[\frac{1}{\gamma^2 + \frac{\pi^2}{4} + 2\gamma \ell n[\frac{ka}{2}] + \{\ell n[\frac{ka}{2}]\}^2}\right] \qquad [6.29]$$

where $\gamma = 0.5772$ is Euler's constant, ϕ the bistatic angle, and a the radius. Table 6.1 shows the monostatic ($\phi = \pi$) and forward ($\phi = 0$) scattering cross-sections for ka between .005 and .2 (250 KHz - 10 MHz).

TABLE 6.1: Monostatic $\sigma(\pi)$ and forward $\sigma(0)$ scattering cross-sections for TE and TM mode incidences

ka	ANALYTIC			NUMERICAL			
	σ_{TM}	$\sigma_{TE}(0)$	$\sigma_{TE}(\pi)$	$\sigma_{TM}(0)$	$\sigma_{TM}(\pi)$	$\sigma_{TE}(0)$	$\sigma_{TE}(\pi)$
.005	62.109	$.2776 \times 10^{-5}$	$.3084 \times 10^{-6}$	62.173	62.207	$.2776 \times 10^{-5}$	$.3086 \times 10^{-6}$
.05	16.247	$.2776 \times 10^{-2}$	$.3084 \times 10^{-3}$	16.031	16.539	$.2775 \times 10^{-2}$	$.3147 \times 10^{-3}$
.1	11.867	$.2221 \times 10^{-1}$	$.2468 \times 10^{-2}$	11.349	12.495	$.2211 \times 10^{-1}$	$.2618 \times 10^{-2}$
.2	9.064	.1777	$.1974 \times 10^{-1}$	7.989	10.459	.1728	$.2293 \times 10^{-1}$

As expected, at lower frequencies, the analytical and numerical results compare exceptionally well, especially for the TE case. The expression [6.29] is independent of aspect angle so that at low frequencies, it

resembles a line source radiating evenly in all directions. Inspection of columns 2, 5 and 6 shows correspondence to almost one decimal-place at ka = .005. In fact, towards lower frequencies, the trend indicates diminishing differences between the analytic and computed results. The probable cause for this behaviour is the singularity of the first kind kernel. Hence, the alternative formulation of [6.16] should produce a better match.

(ii) Upper frequency limitation

The maximum frequency that this particular model can effectively handle, is ascertained by monitoring the behaviour of output observables with increasing ka. These observables are: matrix condition number and determinant; surface current profile; interior fields; and surface fields (TM case). In particular, a total-pivoting strategy is implemented for linear equation solution so that the condition number is estimated from the ratio of the largest to the smallest pivot. From experience, the Galerkin-generated matrix is well-conditioned so that this quantity is quite invariant over the frequency range of operation except at eigenfrequencies of the interior problem. Any departure from the predicted behaviour other than at resonance is checked for overall solution compatibility. For this model, maximum ka $\simeq$ 6.4 or a BEM element size of 1.6λ and a sampling interval of $.4\lambda$. Figures 6.5 and 6.6 represent the variation of normalized monostatic and forward scattering cross-sections with ka. The results of Figure 6.6 correspond almost exactly with those of Bowman *et al* (1969). Aberrations in the TE plot in Figure 6.5 occur at the TM propagation mode frequencies of the circular waveguide and is seen to worsen at the upper portion of the frequency band. This observation is not predicted by the analytic results of Mullin *et*

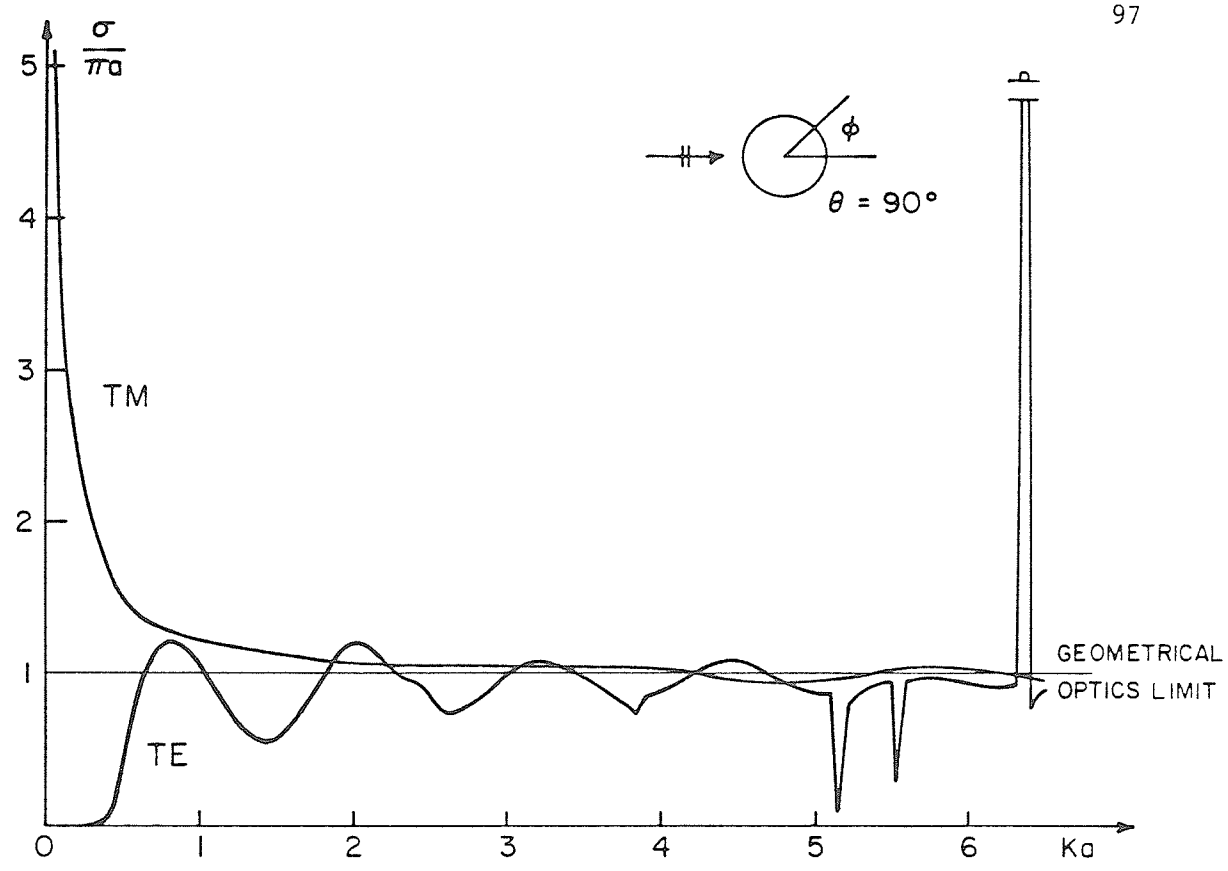

FIG. 6.5: Normalized monostatic cross-section/unit length

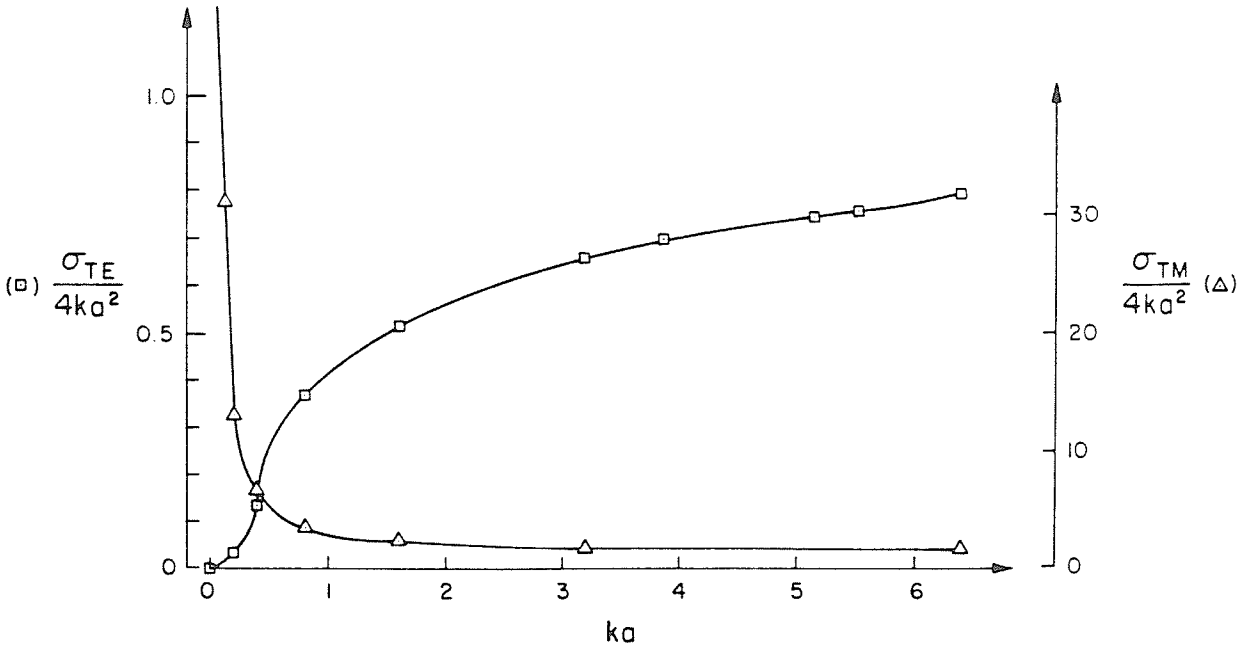

FIG. 6.6: Normalized forward scattering cross-section/unit length

al (1965), and serves as an indication that the integral $\bar{H}$-field solution is prone to interior resonances. At higher frequencies, both TE and TM results are seen to approach the GO limit as predicted by theory.

(iii) Near and far-field computation

Any departures of surface current distribution from the exact, would be manifested in the computation of scattered near-fields. Hence, near-field quantities offer a good gauge as to the precision of solution of the independent variable. For purposes of comparison, equation [6.16] which is the second kind integral for TM incidence, is solved by Galerkin's method. Figures 6.7(a) and 6.7(b) show the total fields evaluated on the wave trajectory that bisects the circular cylinder at ka = 3.832 representing the TM_{11}/TE_{01} mode degeneracies of the circular waveguide. The solid lines indicate the BEM solution whose exterior fields coincide with the exact. The dashed lines are results obtained by Bolomey & Tabbara (1973) using a pulse-expansion, point-matching technique and involving approximately 40 variables. Clearly, the BEM calculated interior fields are closer to theory in that they are relatively smaller in magnitude. Although not explicitly shown, the surface current distributions computed from two matrix solution strategies by Bolomey & Tabbara (1973), are quite different from those shown in Figure 6.7. The BEM calculated currents are in fact, in quite close agreement with the exact. It does appear that the BEM may be a better technique for near-field computation.

Far-fields are usually less affected due to spatial separation and the fact that integration is inherently a *smoothing* operation. Computed RCS patterns in Figure 6.4 and also Figures 6.5 and 6.6, bear this out.

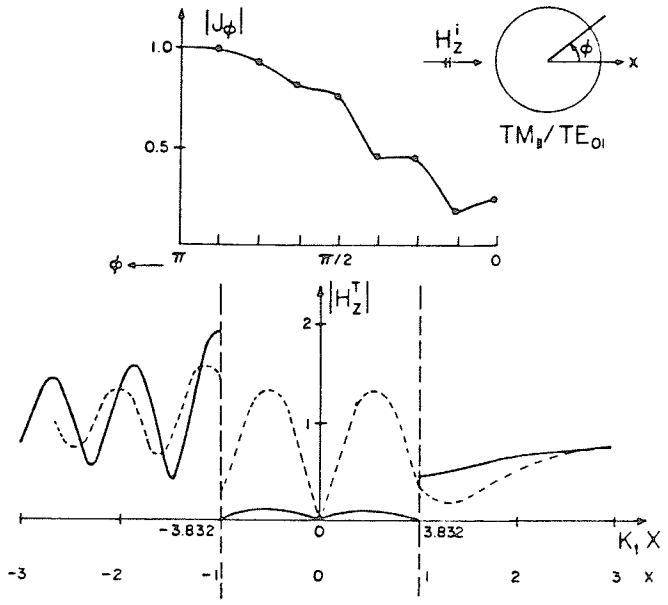

(a)

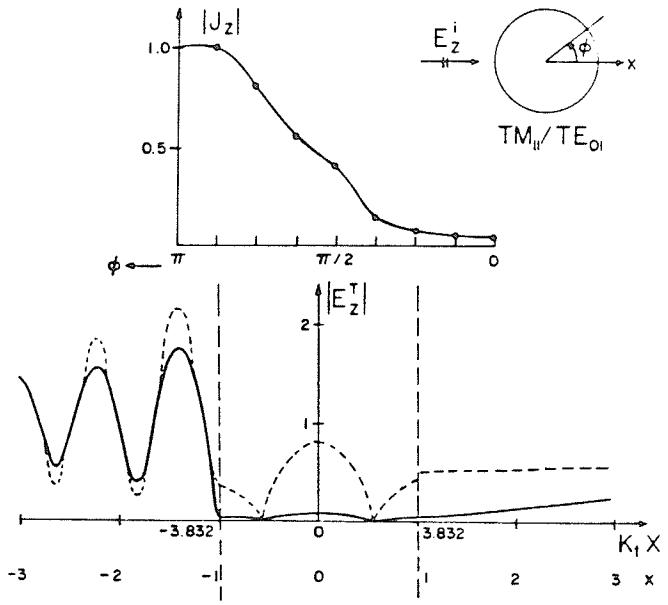

(b)

FIG. 6.7: Surface currents and near-field for:
(a) TE incidence;
(b) TM incidence

One important question at this juncture, pertains to the effectiveness of this particular BEM model and its adequacy to handle source variation. Figure 6.8 shows the transverse currents induced on the cylinder circumference for the cases: 4 quadratic elements; 4 cubic elements; 4 quartic elements (the present model); and 8 quartic elements. In comparing the curves for the last two models, it is clear that not much is gained in the way of accuracy in going from 16 to 32 variables. Therefore, the extra 220% more CPU time (1.5 seconds to 3.3 seconds) for the latter case, is difficult to justify. One interesting point to note is that this doubling of the number of unknowns lead to a doubling in the upper-frequency limit as well.

The precision in operator approximation, is usually reflected in the requirement of quadrature data. Good approximations quite often lead to good accuracy with minimum orders of quadrature. Figure 6.9 illustrates the dependence of the variational functional, matrix condition number and determinant on quadrature order for TM (first kind integral) and TE cases, respectively. Each functional is the magnitude of the *reaction* between the surface currents and the incident field, *i.e.*, $< J_z, E_z^i >$ and $< J_\phi, H_z^i >$ (Harrington, 1961) so that they have units of energy or power. Essentially, they behave as in electrostatic problems in regard to convergence. Two points of interest are obvious from inspection of the curves: (i) 6-point quadrature is sufficient to integrate a quartic expansion of sources (including the kernel); and (ii) the $\bar{H}$-field formulation is better conditioned than the first kind integral as is evidenced from the behaviour of matrix condition number and determinant with quadrature.

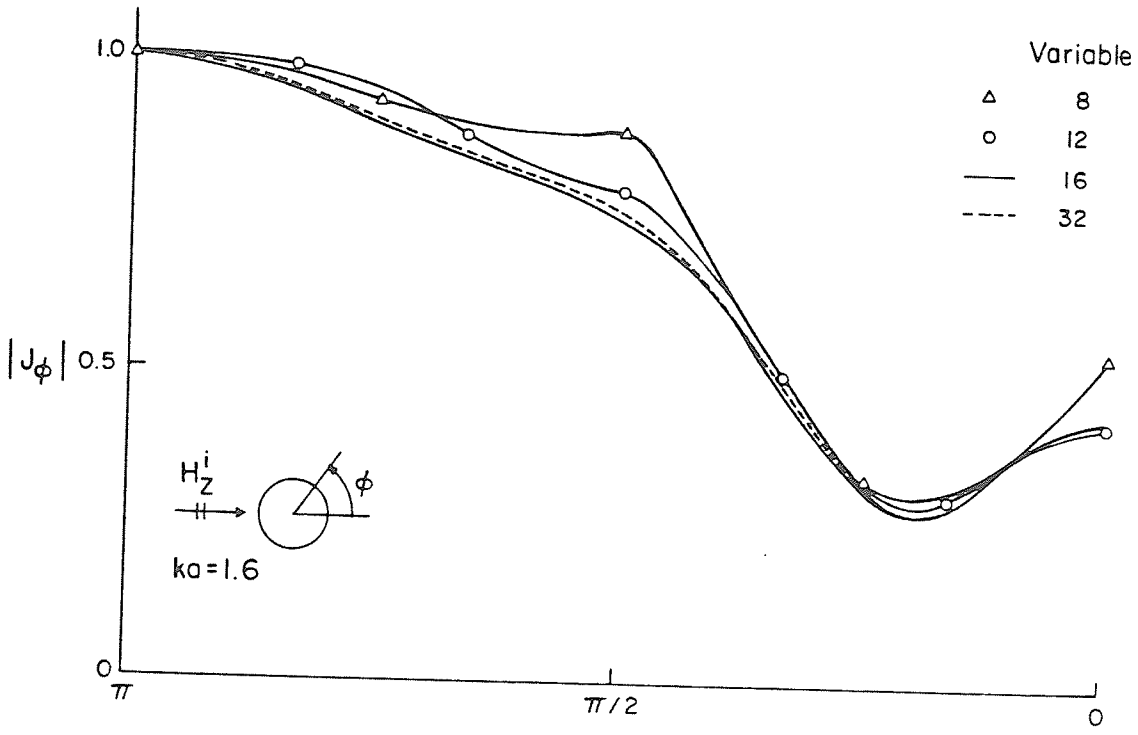

FIG. 6.8: Transverse currents for TE incidence

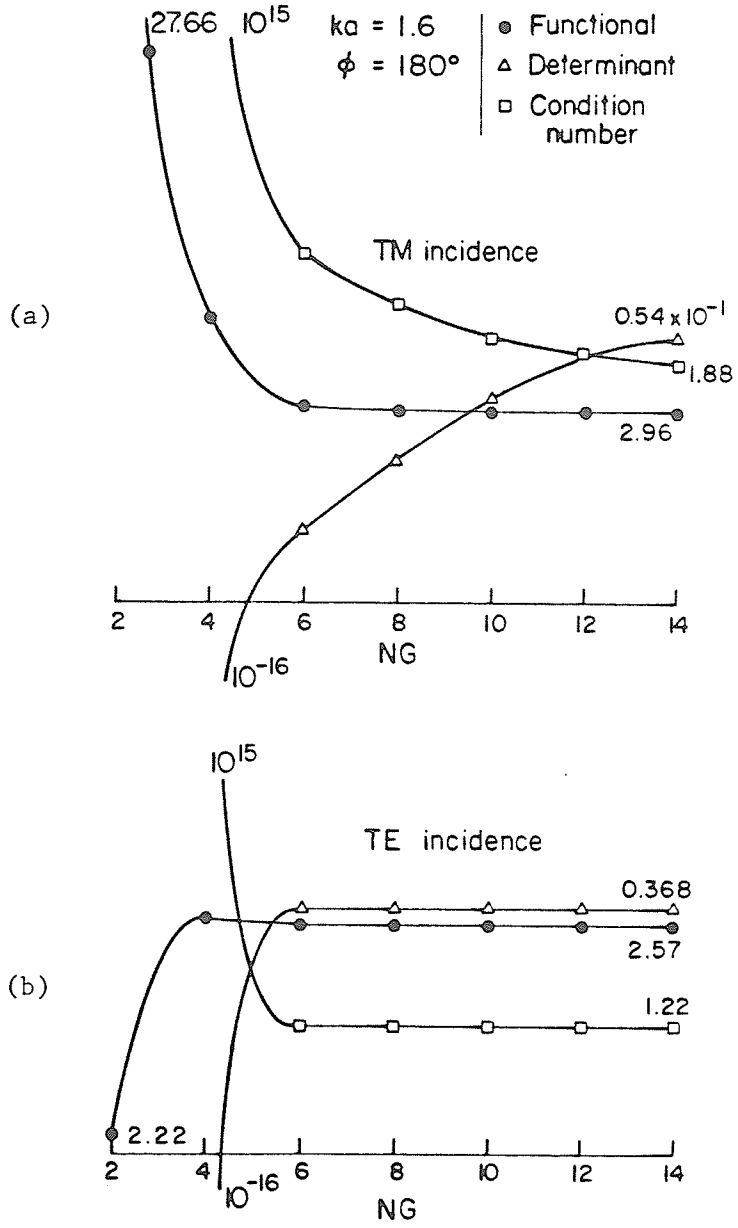

FIG. 6.9: Variation of functional and matrix condition number and determinant with quadrature order (NG) for:
(a) TM incidence;
(b) TE incidence

With regard to matrix conditioning, Figures 6.10 and 6.11 are plots of the same three parameters with increasing ka. Again, the better-behaved second kind kernel giving rise to a better-conditioned matrix is evident. Except at frequencies that correspond to the indicated propagating modes of the circular waveguide, the matrix is well-conditioned over the range of workable frequencies. The very narrow peak indicating a large condition number and a corresponding vanishing determinant, is a good indication of the accuracy of the algorithm. In comparison, the pulse-expansion, point matching technique exhibits no such information. From the low-end of the frequency range to the high, condition number is seen to decrease monotonically whilst matrix determinant increases in the same manner. Their behaviour is quite insensitive to the eigen frequencies for the interior problem.

The minimum sampling rate of this technique is of the order of 5 times per wavelength (Poggio & Miller, 1973). This means that collocation section size is $.2\lambda$. For the BEM model, ka = 6.4 with 16 nodes implies a node separation of $.4\lambda$ or one-half the number of variables compared to the former. In terms of the number of operations for matrix fill where each operation is a point-to-point accumulation, one would require $n_s^2\, n_g^2$ and $n_p^2\, n_g$ for the BEM and the pulse expansion techniques respectively — n_s, n_p and n_g being in order, the number of BEM elements (4), the number of collocation sections ($\simeq$32), and the order of quadrature integration (6 for the BEM). Since the number of pulse-sections is approximately 8 times that of the BEM model, even if $n_g = 1$ for the former and $n_g = 6$ for the latter, it would still require more operations to fill the pulse expansion-generated matrix.

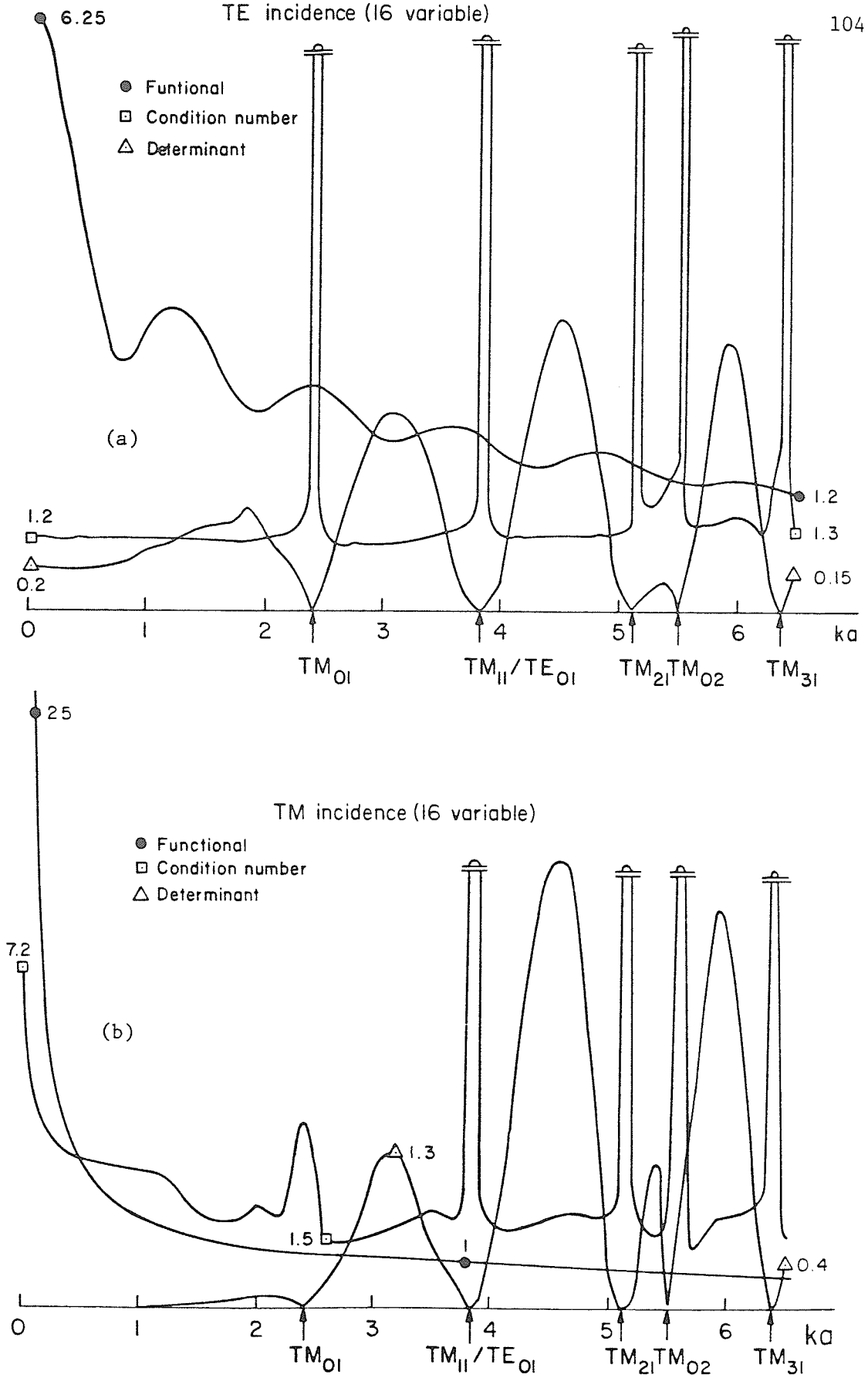

FIG. 6.10: Variation of functional and matrix condition number and determinant with ka for:
(a) TE incidence;
(b) TM incidence

6.3 Three-Dimensional Integral Formulations

A vector formulation in three-dimensions, can be obtained from utilization of the equations in [6.2] in conjunction with a scalar free-space Green's function given by

$$G[\bar{r}|\bar{r}'] = \frac{e^{-jk|\bar{r} - \bar{r}'|}}{4\pi|\bar{r} - \bar{r}'|} \qquad [6.30]$$

where [6.30] satisfies the inhomogeneous Helmholtz equation

$$\nabla \times \nabla \times G[\bar{r}|\bar{r}']\ \hat{a} - k^2 G[\bar{r}|\bar{r}']\ \hat{a} = -\delta(\bar{r} - \bar{r}')\ \hat{a} \qquad [6.31]$$

given that $\hat{a}$ is an arbitrary unit vector. Applying the vector form of Green's Theorem, and simplifying, the result is

$$\bar{\psi} \cdot \hat{a} = \gamma \int_{S + S_\infty} \{\bar{\psi}(s') \times \nabla \times G[\bar{r}|s']\hat{a} - G[\bar{r}|s']\hat{a} \times \nabla \times \bar{\psi}(s')\} \cdot \hat{n}\ ds \qquad [6.32]$$

where $\bar{\psi}(\bar{r})$ is either $\bar{H}(\bar{r})$ or $\bar{E}(\bar{r})$.

6.3.1 Magnetic Field Integral Equation (MFIE)

This formulation of the vector integral equation, is specified by setting $\bar{\psi}(\bar{r}) = \bar{H}(\bar{r})$. Enforcing the boundary conditions that normal magnetic and tangential electric fields vanish on S, *i.e.*

$$\begin{aligned} \hat{n} \cdot \bar{H}\ (\bar{r} \in S) &= 0 \\ \hat{n} \times \bar{E}\ (\bar{r} \in S') &= 0 \end{aligned} \qquad [6.33]$$

and using $\gamma = -2$ on S, equation [6.32] is simplified to

$$\hat{n} \times \int_S \bar{J}(s') \times \nabla' G[s|s']ds' - \frac{\bar{J}(s)}{2} = - \hat{n} \times \bar{H}^i(s) \qquad [6.34]$$

where the equivalent source notation

$$\bar{J} = \hat{n} \times \bar{H} \qquad [6.35]$$

has been incorporated into the simplification. The expression $\nabla' G$ is the gradient of Green's function in source coordinates and is given by

$$\nabla' G = (\bar{r} - \bar{r}') \frac{e^{-jk|\bar{r} - \bar{r}'|}}{4\pi|\bar{r} - \bar{r}'|^3} (1 + jk|\bar{r} - \bar{r}'|) \qquad [6.36]$$

Equation [6.35] is a vector second kind integral that may be solved for surface currents $\bar{J}$. The scattered field $\bar{H}^s(\bar{r})$ is then evaluated from

$$\bar{H}^s(\bar{r}) = \int_S \bar{J}(s') \times \nabla' G[\bar{r}|s']ds' \qquad [6.37]$$

and the total field expressed as

$$\bar{H}(\bar{r}) = \bar{H}^i(\bar{r}) + \bar{H}^s(\bar{r}) \qquad [6.38]$$

For the computation of far-field quantities, the asymptotic form of $\nabla' G$ is obtained by neglecting phase factors. Thus,

$$\nabla' G[\bar{r}|\bar{r}'] \xrightarrow[|\bar{r} - \bar{r}'| \to \infty]{} \hat{r} \frac{jk}{4\pi} \frac{e^{-jkr}}{r} e^{jk \hat{r} \cdot \bar{r}'} \qquad [6.39]$$

retaining only terms in r^{-1}. This equation when substituted in [6.37] gives the scattered far-field

$$\bar{H}^s(\bar{r})\Big|_{r\to\infty} = \frac{e^{-jkr}}{4\pi r}\int_S \{jk\ \bar{J}(s)\ x\ \hat{r}\}\ e^{jk\ \hat{r}\ \cdot\ \bar{r}'} \qquad [6.40]$$

The RCS is dependent on elevation and azimuthal angles θ and ϕ respectively (Figure 6.11), and is given by the expression

$$\sigma(\theta,\ \phi) = \lim_{r\to\infty}\ 4\pi r^2\ \frac{|\bar{H}^s|^2}{|\bar{H}^i|^2} \qquad [6.41]$$

which simplifies to the form

$$\sigma(\theta,\ \phi) = \frac{1}{4\pi}\left[\int_S \{jk\ \bar{J}(s')\ x\ \hat{r}\}\ e^{jk\ \hat{r}\ \cdot\ \bar{r}'}\ ds'\right]^2 \qquad [6.42]$$

In particular, the E- and H-plane RCS are obtained by specifying $\phi = 0$ (x-z plane) and $\theta = \frac{\pi}{2}$ (y-z plane), respectively.

6.3.2 Electric Field Integral Equation (EFIE)

The electric field equivalent of [6.34] is specified by setting $\bar{\psi}(\bar{r}) = \bar{E}(\bar{r})$. Again, enforcing the conditions of [6.33] on S, the resultant EFIE expression simplifies to

$$\frac{1}{j\omega\varepsilon}\ \hat{n}\ x\int_S \{-k^2\bar{J}(s')\ G[s|s'] + \nabla'_s\ \cdot\ \bar{J}(s')\ \nabla' G[s|s']\}ds' = \hat{n}\ x\ \bar{E}^i(s) \qquad [6.43]$$

where ∇'_s is a surface divergence operator in source coordinates. Equation [6.43] is a vector first kind integral in $\bar{J}$. The scattered field $\bar{E}^s(\bar{r})$ is computed from

$$\bar{E}^s(\bar{r}) = -\int_S \{j\omega\mu\ \bar{J}(s') - \frac{j}{\omega\varepsilon}\ \nabla'_s\ \cdot\ \bar{J}(s')\ \nabla' G[\bar{r}|s']\}ds' \qquad [6.44]$$

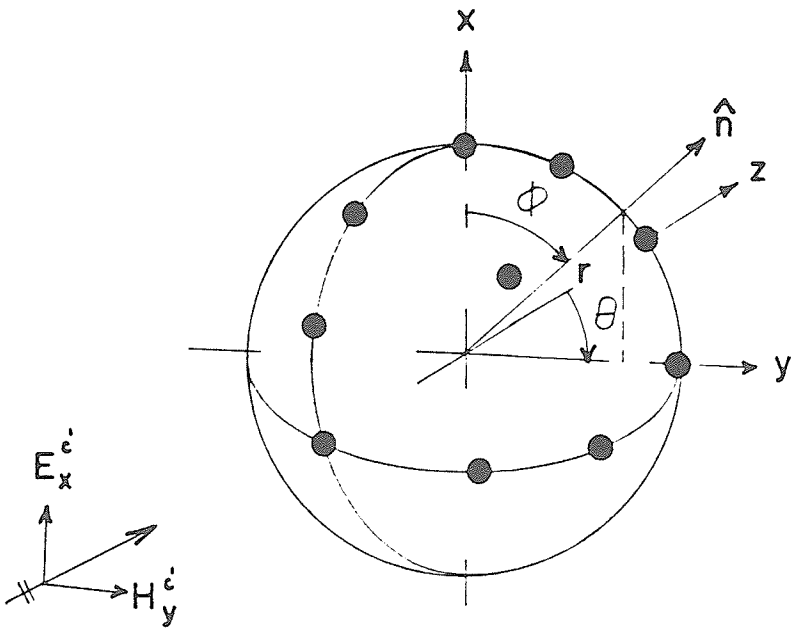

FIG. 6.11: Scatterer problem geometry

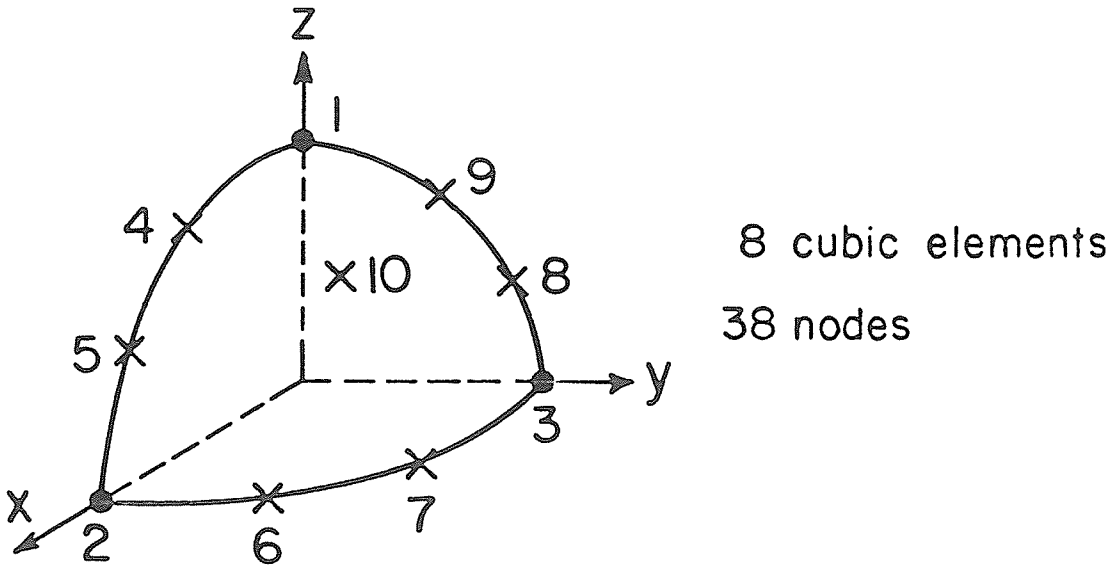

FIG. 6.12: BEM model of sphere - positive octant

Using the asymptotic form of [6.39], the far-field is obtained as

$$\bar{E}^s(\bar{r})\Big|_{r\to\infty} = \frac{jk}{4\pi r} e^{-jkr} \int_S \{(\hat{r} \cdot \bar{J}(s'))\ \hat{r} - \bar{J}(s')\}\ e^{jk\ \hat{r} \cdot \bar{r}'}\ ds' \quad [6.45]$$

Following [6.41], the RCS is mathematically given by

$$\sigma(\theta, \phi) = \lim_{r\to\infty} 4\pi r^2 \frac{|\bar{E}^s|^2}{|\bar{E}^i|^2} \quad [6.46]$$

which is simplified to give

$$\sigma(\theta, \phi) = \frac{1}{4\pi} [\int_S jk\{(\hat{r} \cdot \bar{J}(s'))\ \hat{r} - \bar{J}(s')\}\ e^{jk\ \hat{r} \cdot \bar{r}'}\ ds']^2 \quad [6.47]$$

where E- and H-plane RCS are as defined for the MFIE case.

6.4 Scattering from the Perfectly Conducting Sphere

The MFIE of [6.34] is implemented to solve this problem using Galerkin's method. Due to the nature of the problem, only surface currents can flow where $\bar{J}(s)$ accounts for the jump discontinuity in magnetic field encountered in crossing this surface. As such, $\bar{J}$ need only be specified in terms of a pair of orthogonal surface vectors to fully describe the problem. The integral formulation [6.34] can then be resolved into two scalar equations involving $2N$ unknowns (*e.g.*, Oshiro & Su (1965)). This resolution scheme runs into problems in the treatment of angular geometries — creases and edges, especially when higher-order interpolation involving node-point values, are used. The notable exception is pulse-expansion for sources where the independent variable is solicited only at the patch-centroid. As a result, the present BEM code is specified in cartesian coordinates involving $3N$ unknowns. It is

felt that with the efficient use of quadrature data, acceptable precision may be obtainable without placing too heavy demands on solution time.

The BEM model of the sphere consist of 8 cubic elements involving 38 nodes, each with 3 degrees of freedom (Figure 6.12). Without resorting to symmetry, a total of 114 unknowns are required. The cubic element has precision in surface modelling, to two decimal places. With quarter-space symmetry (as in Oshiro & Su (1965)), a total of 16 nodes and 48 variables would be sufficient.

On resolving the discretized version of [6.34] into component forms, the resulting matrix assembly may be given by

$$\begin{bmatrix} S_1 + A & S_2 & S_3 \\ S_4 & S_5 + A & S_6 \\ S_7 & S_8 & S_9 + A \end{bmatrix} \begin{bmatrix} \underline{J}_x \\ \underline{J}_y \\ \underline{J}_z \end{bmatrix} \qquad \begin{bmatrix} \underline{b}_1 \\ \underline{b}_2 \\ \underline{b}_3 \end{bmatrix} \qquad [6.48]$$

where $\underline{J}_x$, $\underline{J}_y$ and $\underline{J}_z$ are column vectors of the respective component of current density. The sub-matrices denoted S_i resemble

$$S_i = \int_S \underline{\alpha}(s) \int_S K_i \, \underline{\alpha}^T(s') \, ds'ds \quad ; \quad i = 1, 2, \ldots, 9 \qquad [6.49]$$

where K_i are the respective kernels given by

$$K_1 = n_y(s) \frac{\partial G}{\partial y'} + n_z(s) \frac{\partial G}{\partial z'}$$

$$K_2 = - n_y(s) \frac{\partial G}{\partial x'}$$

$$K_3 = - n_z(s) \frac{\partial G}{\partial x'}$$

$$K_4 = - n_x(s) \frac{\partial G}{\partial y'}$$

$$K_5 = n_z(s) \frac{\partial G}{\partial z'} + n_x(s) \frac{\partial G}{\partial x'} \qquad [6.50]$$

$$K_6 = - n_z(s) \frac{\partial G}{\partial y'}$$

$$K_7 = - n_x(s) \frac{\partial G}{\partial z'}$$

$$K_8 = - n_y(s) \frac{\partial G}{\partial z'}$$

$$K_9 = n_x(s) \frac{\partial G}{\partial x'} + n_y(s) \frac{\partial G}{\partial y'}$$

Along the main diagonal, the additional square-matrix A is due to the vector second kind integral and is given by

$$A = - \int \frac{1}{2} \underline{\alpha}(s) \, \underline{\alpha}^T(s) \, ds \qquad [6.51]$$

Finally, the excitation vector is formed from the stacking of the respective x,y and z components and represented as

$$\underline{b}_1 = -\int_S \underline{\alpha}(s)\ \{n_y(s)\ H_z^i(s) - n_z(s)\ H_y^i(s)\}ds$$

$$\underline{b}_2 = -\int_S \underline{\alpha}(s)\ \{n_z(s)\ H_x^i(s) - n_x(s)\ H_z^i(s)\}ds \qquad [6.52]$$

$$\underline{b}_3 = -\int_S \underline{\alpha}(s)\ \{n_x(s)\ H_y^i(s) - n_y(s)\ H_x^i(s)\}ds$$

Of the nine kernels shown in [6.50] only the three forms resulting from the taking of first derivatives of G with respect to x', y' and z' are unique. Hence, for integration over the source co-ordinates, only three function evaluations are required followed by a multiplication with the appropriate normal component. This manner of accumulating the system matrix *en masse* reduces fill-time by at least three times when compared to the more obvious *block-by-block* scheme.

The kernels of [6.50] can be shown to behave as

$$\frac{e^{-jkd}}{4\pi d} + \frac{jk}{4\pi}\ e^{-jkd} \qquad [6.53]$$

in the limit of vanishing d. The first term of [6.53] is the free-space Green's function and thus has r^{-1} behaviour. The remaining term is superposed on the first and is seen to cause a cosine modulation of the imaginary term. Provided [6.53] is not overly oscillatory over the interval of integration, the numerical scheme outlined in Subsection 3.2.2 will be effective. As $k \to 0$, the Poisson Green's function is seen to appear in [6.53].

Finally, the incident field is assumed to be a plane wave (TEM) with linear polarization in the x-direction and propagating along the positive z-axis. Thus, the incident field resembles

$$\bar{H}^i(\bar{r}) = \hat{j}\, H_y^i\, e^{-jkz} \qquad [6.54]$$

The calculated E- and H-plane current magnitudes for ka = 1.7 are shown in Figure 6.13(a). The solid and dashed lines correspond to plots of exact results published in King & Wu (1959). This particular set of data is obtained using the 38 node model involving 114 unknowns and 16-point quadrature over each element. Inspection of Figure 6.13(a) shows that the H-plane current magnitudes are in closer agreement with the exact, especially in the area away from the centers of the illuminated and shadow regions. The discrepancy in E-plane data may be due to the higher-order current variation and the inability of the interpolation scheme to follow this behaviour. A 36-point quadrature produced the plots of Figure 6.13(b), showing overall improvement. Execution time requirements are given in Table 6.2.

TABLE 6.2: Timing Requirement for Scattering Calculation

Order of quadrature	Execution time* CPU seconds	Matrix fill time(%)	Surface area
4	58	78	12.5422
6	200	88	12.5424

* All computations performed on the University of Manitoba AMDAHL 470 V7 system.

The calculated values for surface area offer an indication of the fidelity in geometrical representation. For a unit sphere, the exact value is 4π or 12.5664 which when compared to the last column in Table 6.2, show less than .2% error in overall surface description. More importantly, the only difference between the two tabulated values is

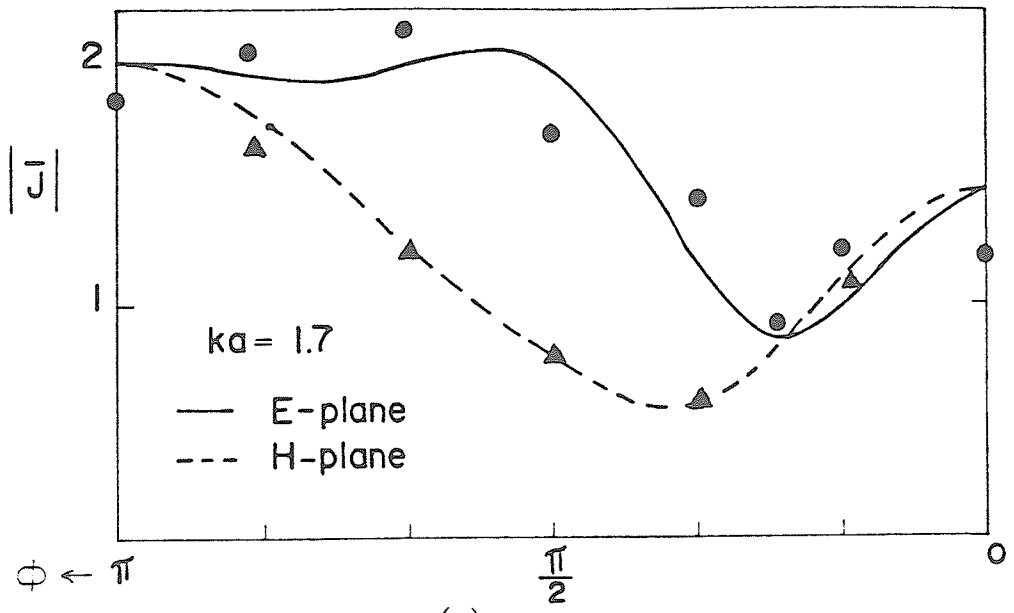

(a)

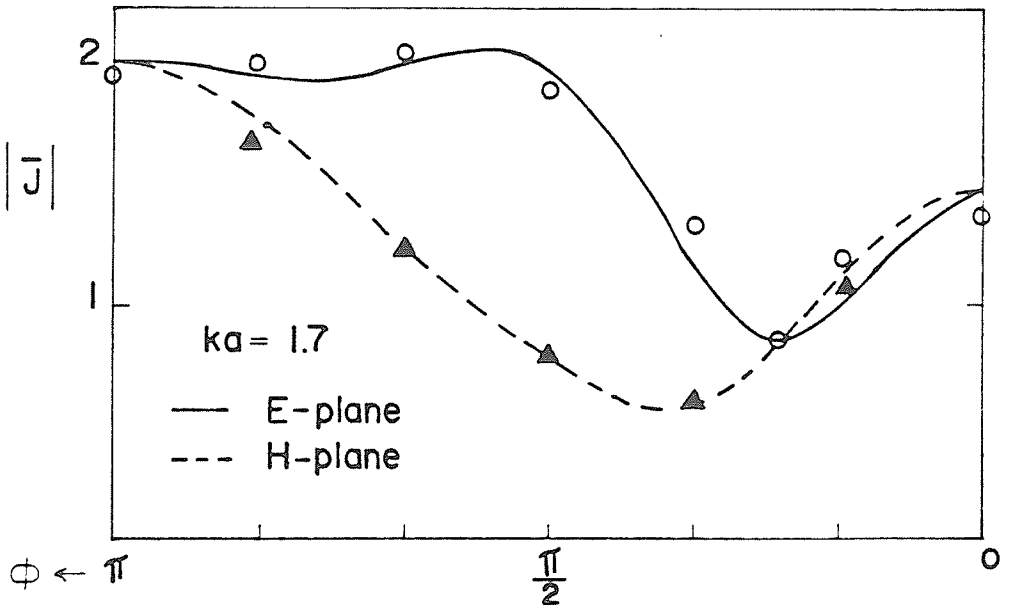

(b)

FIG. 6.13: E- and H-plane current magnitudes for ka = 1.7:
(a) NG = 4; and
(b) NG = 6

in the fourth decimal place. This means that a cubic element is sufficient to model one octant of a sphere. However, an increase in quadrature order is seen to be necessary for better solution accuracy. Probably a fifth order quadrature would have sufficed except that the element has an internal node at the centroid, thus running into numerical inaccuracies when the center point of the quadrature grid approaches this node.

Analogous to the two-dimensional example, the total $\bar{H}$-field magnitudes are computed along a wave trajectory passing through the center of the sphere. Figure 6.14 shows the expected nulling of interior fields using 16-point quadrature. The sinusoid in front of the sphere is reminiscent of a standing wave effect caused by an obstacle. Plots of normalized E- and H-plane bistatic cross-sections for a few values of ka are illustrated in Figure 6.15. These results are generated using the lower-order quadrature scheme and are comparable to those given in King & Wu (1959). This better agreement in scattering cross-section than in current distribution, is a natural consequence of the *energy* method. Convergence in this regard implies that energy-related parameters will enjoy better precision.

The upper frequency for this model may be assumed to be at about $ka \simeq 3.5$. This means approximately 2 elements/λ^2 or a surface area to node ratio of $.12\lambda^2$. Compared to a suggested collocation patch area (Burke & Poggio, 1977) of $.04\lambda^2$, or a sampling rate of $25/\lambda^2$, the BEM model shows a reduction by a factor of 3 in the number of unknowns. Again, denoting n_s, n_p and n_g to be the number of BEM elements, pulse-expansion patches, and order of quadrature, respectively; the number of operations (point-to-point accumulation) required for matrix fill is $n_s^2\, n_g^4$ for the former, and $n_p^2\, n_g^2$ for the latter. Even though n_p is

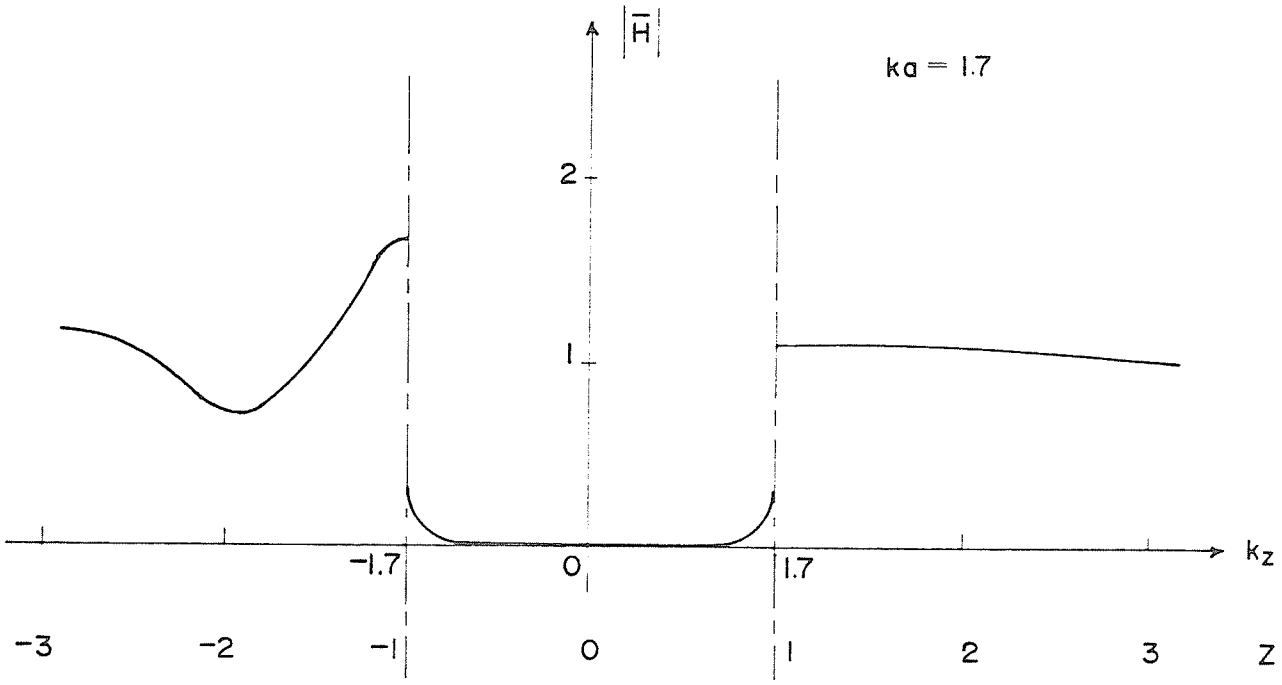

FIG. 6.14: Computed near-field

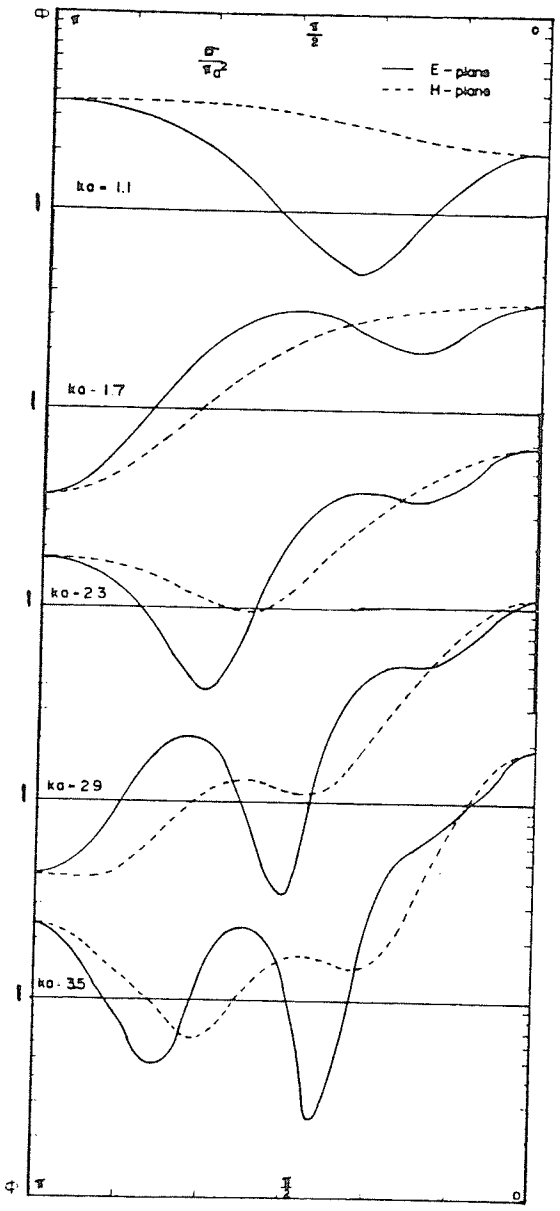

FIG. 6.15: Normalized E- and H-plane bistatic cross-sections

quite a bit larger than n_s, the order of quadrature for the BEM model goes up as the fourth power. Hence, quite a bit more CPU time is needed by this particular model.

One obvious way to cut down on the computation time, is to introduce $\frac{1}{8}$ symmetry, thus reducing treatment to one element and 10 nodes. This would effectively reduce the number of operations by a factor of 64. Another saving could be realized by resolving $\bar{J}$ on S into two surface components (especially for the sphere), thus requiring only 20 unknowns. To improve on source interpolation, the choice is between going to a quartic element, and using two lower-order elements in place of just one.

The main drawback of the present interpolation scheme, not really felt in two-dimensions, is the requirement for more unknowns for increasing orders of interpolation. For up to a linear variation, this scheme is definitely viable since all nodes are shared by at least two or more elements. Succeeding orders need interior nodes whose data contribute to this one element only. Hence, any algorithm that allows the usage of information from exterior nodes, especially for high-order interpolation, and yet remains sufficiently flexible for general application, would be advantageous for three-dimensional problems.

VII. CONCLUSION

The scope of this thesis has been the solution of field problems posed in boundary integral form. The introduction of the digital computer a few decades ago has rekindled renewed interest in this mode of solution and done much to spur development of efficient numerical algorithms to fill the void separating this and the sophisticated mathematics that has been the norm of partial differential equation (pde) problem solution. In this regard, the BEM algorithm is proving to be a creditable proponent. Of special significance is the fact that it originated from an extension of the finite element method (FEM) (originally developed to address pde formulated problems), to integral equation problems. When compared to the pde scheme of things, it offers certain intrinsic advantages. Principal among them is the reduction of problem dimension by one since it seeks a boundary representation for any prescribed problem region. One immediate spin-off is reflected in the size of the system matrix which is very much smaller (although dense) than that of the pde counterpart for the same problem. Also, the amount of input data is minimal compared to the volume of data normally required for a pde analysis using the FEM or finite-difference techniques.

Another advantage is that boundary conditions are built into the formulation thus making for algorithmic simplicity and compactness. Because of the boundedness of the operator, the integral formulation has a natural ability to model open region problems physically where field effects vanish asymptotically in the proper manner. In contrast, all pde solution schemes can handle only a finite region of space, thus calling for artificial truncation of problem boundaries. An added bonus lies

in the better accuracy normally observed, a trait due to the integration process being a *smoothing* operation.

One frequently cited disadvantage is its inability to cater for inhomogeneous media. This is due in part to the decision to retain the flexibility for treating arbitrarily shaped surfaces with general boundary conditions; an ability made possible only through the exclusive use of the free-space Green's function. The alternative is to devise problem-dependent Green's functions — a procedure that may sometimes be more involved than the actual problem itself. For problems that involve volumetric sources and even anisotropy, the integral equation formulation may still be the more viable alternative. However, material inhomogeneous and nonlinearities are better handled by the partial differential operator. Hence, for complete field definition, an artificial boundary may be created to isolate a finite region within which a partial differential solution is sought. Exterior to this boundary, an integral equation method may be applicable with consequent tie-in at the common interface. An example of this hybrid solution scheme is the mutually constrained *picture-frame* technique of McDonald & Wexler (1980) where the exterior integral formulation is used to compute constraint equations that serve as the boundary conditions for the interior partial differential region. Another example is the *unimoment method* of Mei (1974), where the interior problem is solved using finite-differences involving a *shooting method*, or a Ricatti transformation for the generation of trial function pairs. The exterior solution is then expanded by cylindrical or spherical harmonics with unknown coefficients and matched at the interface, thus requiring the solution of a system of $4N$ linear equations. Other techniques that require the mechanical coupling of individual system matrices

are detailed in Kelly *et al* (1979) and Shaw (1978). One conceivable area for future work could be the automated algorithmic (and geometric) coupling of the BEM to the FEM along the lines of McDonald & Wexler (1980). An immediate improvement would be the savings incurred in deleting the layer of finite elements representing the region (homogeneous) of overlap of the two solution schemes. This simplification is made possible by the capability to address Green's function singularity at the common interface, in a direct manner.

Another detriment to the choice of integral equations for field solution is the kernel singularity. Inappropriate attempts to handle the singular kernels (or totally ignoring them), will lead to matrix ill-conditioning especially for increasingly large matrices. In a well-conditioned system, the solution is described by hyperplanes that intersect at $90°$ (Wexler, 1969) so that the intersection is relatively insensitive to round-off error. As matrix conditioning deteriorates, the included angles decrease to the point of instability. The ability to identify and numerically treat singularities in a manner previously outlined, will ameliorate this traditional problem area.

One obvious characteristic of the integral equation formulation, is the denseness of the matrix due to mutual interaction of all source points. For the moment, the BEM uses a triangularization procedure which although of order N^3, is still three times more efficient than inversion. At high frequencies where problem dimensions may be many wavelengths long, or even where problem geometry may be very large, such a practice may not be practical or even possible due to core limitations. For the situation that the matrix size may be accomodated on the computer, the practice of suppressing altogether smallish off-diagonal terms

to obtain some measure of sparseness, is crude at best and needs to be justified on an individual basis. A more elegant manner for obtaining sparsity using subsectioning of problem regions, is discussed in Wexler (1979). This scheme is derived from a method of tearing - *diakoptics* - where problem solution is accomplished by treating individual component parts and their interactions in sequence (*e.g.*, Happ (1974)). This problem forms another basis for future work with the BEM to handle electromagnetically large structures. An alternative strategy involves matrix iterative procedures that require only N^2 operations. The disadvantage lies in the total re-analysis required for every new set of excitation functions. This differs from the previous technique where part or all of the system matrix may be inverted and stored in factored form for use in re-analysis. For extremely large problems, the matrix may be segmented and treated sequentially as in the *progressive numerical method* of Shoamanesh & Shafai (1976).

In summary, Chapters II and III have provided some salient features of the BEM that shows it to be a generalized numerical code capable of addressing a wide range of engineering problems. Although exemplary problems in subsequent chapters have been drawn from the electrical discipline, its application is by no means restricted in this sense. The successful treatments of static, interface, and time-harmonic problems in Chapters IV, V and VI respectively, attest to its versatility. In particular, the treatment of Green's function singularity is seen to be adequate as is apparent from the low-order quadratures required. This treatment is not *exact* in the sense of faithfully duplicating function behaviour except in the vicinity of the singularity. Such a scheme may not be possible given the arbitrariness in selection of element sizes.

Therefore, the main objective is to concentrate on the localized behaviour instead. From experience, results have indicated that at times, the order of quadrature for the *self-element* may be adequate, but overall accuracy is hindered by the low orders of quadrature chosen for surrounding elements.

From a purely economical point of view, the present BEM algorithm may not be as viable as the pulse-expansion, point-matching technique (*e.g.*, NEC) for three-dimensional problems. This is because the number of independent variables increases as the order of interpolation, thus pushing up processing time per element. One immediate improvement in this regard would be to redefine a new set of interpolation functions for sources, where mid-side and internal nodal data may be stored at vertex positions in the form of derivative information (*e.g.*, spline interpolation (Coons, 1974)). In essence, fewer variables would be required to specify the same problem. The Lagrange interpolation scheme could still be retained for surface modelling, depending on the precision of the new interpolation scheme. Another alternative would be to implement a polynomial expansion, point-matching scheme with accompanying treatment of Green's function singularities at vertex nodes. The resulting number of operations would then be proportional to the square of the quadrature order n_g^2 (rather than n_g^4 as before), and would be in the same range as that required by NEC. However, it has the added capability for accurate surface representation as well. The main underlying advantage of the BEM algorithm is the use of Galerkin's method, which ensures the stability of the matrix. Especially when working in a less well-defined area, the assurance that the matrix will be well-behaved means one less source of aggravation in problem solution.

REFERENCES

Abramovitz, M. and Stegun, I.A. (eds.) (1968). Handbook of Mathematical Functions, Dover Pubs. Inc., New York.

Acton, F.S. (1970). Numerical Methods that Work, Harper & Row, Publishers, New York.

Al-Badwaihy, K.A. and Yen, J.L. (1975). "Extended Boundary Condition integral equations for perfectly conducting and dielectric bodies: formulation and uniqueness," IEEE Trans. Antennas & Propagation, vol. AP-23, 546-551.

Andreasen, M.G. (1965). "Scattering from cylinders with arbitrary surface impedance," Proc. IEEE, vol. 53, 812-817.

Bolomey, J-C. and Tabbara, W. (1973), "Numerical aspects on coupling between complementary boundary value problems," IEEE Trans. Antennas & Propagation, vol. AP-21, no. 3, 356-363.

Bowman, J.J., Senior, T.B.A. and Uslenghi, P.L.E. (eds.) (1969). Electromagnetic and Acoustic Scattering by Simple Shapes, American Elsevier Publishing Co. Inc., New York.

Burke, G.J. and Poggio, A.J. (1977). Numerical Electromagnetic Code (NEC) - Method of Moments, Part I & II, Tech. Doc #116, Naval Ocean Systems Center, San Diego, California.

Burnside, W.D., Yu, C.L. and Marhefka, R.J. (1975). "A technique to combine the Geometrical Theory of Diffraction and the Moment Methods," Succinct paper, IEEE Trans. Antennas & Propagation, vol. AP-23, 551-558.

Coons, S.A. (1974). "Surface patches and B-spline curves," in Computer Aided Geometric Design, Barnhill, R.E.and Riesenfield, R.F., Academic Press, New York.

Cruse, T.A. (1974). "An improved boundary-integral equation method for three-dimensional elastic stress analysis," Comp. & Struct., vol. 4, 741-754.

Decreton, M.C. (1972). Treatment of Singularities in the Finite-Element Method, M.Sc. Thesis, University of Manitoba, Winnipeg, Canada.

Garbacz, R.J. (1965). "Modal expansions for resonant scattering phenomena," Proc. IEEE, 856-864.

Happ, H.H. (1974). "Diakoptics - The Solution of System Problems of Tearing," (Invited Paper), Proc. IEEE, vol. 62, 930-940.

Harrington, R.F. (1961). Time-Harmonic Electromagnetic Fields, McGraw-Hill, New York.

Harrington, R.F. (1968). Field Computation by Moment Methods, Macmillan, New York.

Jaswon, M.A. and Symm, G.T. (1977). Integral Equation Methods in Potential Theory and Elastostatics, Academic Press, New York.

Jeng, G. (1977). Isoparametric, Finite-Element Boundary Integral Solution of Three-Dimensional Fields, Ph.D. Dissertation, University of Manitoba, Winnipeg, Canada.

Jeng, G. and Wexler, A. (1978). "Self-adjoint variational formulation of problems having non-self-adjoint operators," IEEE Trans. Microwave Theory and Techniques, vol. MTT-26, 91-94.

Kelly, D.W., Mustoe, G.G.W. and Zienkiewicz, O.C. (1979). "Coupling boundary element methods with other numerical methods, in Developments in Boundary Element Methods - I, Banerjee, P.K. & Butterfield, R. (eds.), Applied Science Publishers Ltd., Barking, Essex, England.

King, R.W.P. and Wu, T.T. (1959). The Scattering and Diffraction of Waves, Harvard University Press, Cambridge, Mass.

Kleinman, R.E. (1965). "The Rayleigh region," Proc. IEEE, vol. 53, 848-856.

Lachat, J.C. (1975). A Further Development of the Boundary Integral Technique for Elastostatics, Ph.D. Dissertation, University of Southampton, United Kingdom.

Lachat, J.C. and Watson, J.O. (1976). "Effective numerical treatment of boundary integral equations," Int. J. Num. Meth. Eng., vol. 10, 991-1005.

Lean, M.H. and Wexler, A. (1979a). MANBEP: A Scalar Isoparametric BEM Program (Preliminary Version), Tech. Rept. TR 79-3, Dept. Elec. Eng., University of Manitoba, Winnipeg, Canada.

Lean, M.H., Friedman, M. and Wexler, A. (1979b). "Application of the boundary element method in electrical engineering problems," in Developments in Boundary Element Methods - I, Banerjee, P.K. & Butterfield, R. (eds.) Applied Science Publishers Ltd., Barking, Essex, England.

Lean, M.H. and Wexler, A. (1980). MANBEP-2DS: A Scalar Isoparametric BEM Program for Two-Dimensional Fields, internal report, Dept. Elec. Eng., University of Manitoba, Winnipeg, Canada.

Lean, M.H. and Wexler, A. (1981a). "Application of the Boundary Element Method to electromagnetic scattering problems," in 1981 IEEE AP-S International Symposium Digest, vol. 1, Los Angeles, California.

Lean, M.H. and Wexler, A. (1981b). "Accurate field computation with the Boundary Element Method," to be presented at Compumag - Chicago, Sept. 14-17 (also to be published in IEEE Trans. Magnetics, March 1982).

Lin, Y.T. and Richmond, J.H. (1975). "EM modelling of aircraft at low frequencies," IEEE Trans. Antennas & Propagation, vol. AP-23, 53-56.

McDonald, B.H., Friedman, M. and Wexler, A. (1974). "Variational solution of integral equations," IEEE Trans. Microwave Theory and Techniques, vol. MTT-22, 237-248.

McDonald, B.H. (1975). Constrained Variational Solution of Field Problems, Ph.D. Dissertation, University of Manitoba, Winnipeg, Canada.

McDonald, B.H. and Wexler, A. (1980). "Mutually constrained partial differential and integral equation field formulations," in Finite Elements in Electrical and Magnetic Field Problems, Chari, M.V.K. and Silvester, P.P. (eds.), John Wiley & Sons Ltd., New York.

Mei, K.K. and Van Bladel, J. (1963). "Low-frequency scattering by rectangular cylinders," IEEE Trans. Antennas & Propagation, vol. AP-11, 52-56.

Mei, K.K. (1974). "Unimoment method of solving antenna and scattering problems," IEEE Trans. Antennas & Propagation, vol. AP-22, 760-766.

Mikhlin, S.G. (1964). Variational Methods in Mathematical Physics, Macmillan, New York.

Miller, E.K. and Poggio, A.J. (1978). "Moment-method techniques in electromagnetics from an application viewpoint," in Electromagnetic Scattering, Uslenghi, P.L.E. (ed.), Academic Press, New York.

Mitchell, A.R. and Wait, R. (1977). The Finite Element Method in Partial Differential Equations, John Wiley & Sons. Ltd., New York.

Mitzner, K.M. (1968). "Numerical solution of the exterior scattering problem at eigen frequencies of the interior problem," Fall URSI meeting, Boston, Mass.

Morita, N. (1979). "Resonant solutions involved in the integral equation approach to scattering from conducting and dielectric cylinders," IEEE Trans. Antennas & Propagation, vol. AP-27, 869-871.

Mullin, C.S., Sandburg, R. and Velline, C.O. (1965). "A numerical technique for the determination of scattering cross-sections of infinite cylinders of arbitrary geometrical cross-section," IEEE Trans. Antennas & Propagation, vol. AP-13, 141-149.

Nedelec, J.C. (1976). "Curved finite element methods for the solution of singular integral equations on surfaces in R^3," Comp. App. Mech. Eng. vol. 8, 61-80.

Noble, B. (1971a). A Bibliography on: "Methods for Solving Integral Equations," author listing and subject listing, Tech. Repts. #1176 and #1177, Math. Res. Cent., U. of Wisconsin, Madison, Wis.

Noble, B. (1971b). "Some applications of the numerical solution of integral equations to boundary value problems," in Conference on Applications of Numerical Analysis, Morris. J.L. (ed.), Springer-Verlag, Berlin.

Oshiro, F.K. and Su, C.S. (1965). A Source Distribution Technique for the Solution of General Electromagnetic Scattering Problems - Phase 1 Report, Northrop, Norair, NOR 65-271.

Poggio, A.J. and Miller, E.K. (1973). "Integral equation solutions of three-dimensional scattering problems," in Computer Techniques for Electromagnetics, Mittra, R. (ed.), Pergamon Press Ltd., New York.

Richmond, J.H. (1966). "A wire-grid model for scattering by conducting bodies," IEEE Trans. Antennas & Propagation, vol. AP-14, 782-786.

Richmond, J.H. (1969). Computer Analysis of Three-Dimensional Wire Antennas, Electro-Science Laboratory, Tech. Rept. 2708-4, Ohio State University, Ohio.

Shafai, L. (1969). Electromagnetic Fields in the Presence of Cylindrical Objects of Arbitrary Physical Properties and Cross-Sections, Ph.D. Dissertation, Univeristy of Toronto, Ontario, Canada.

Shaw, R.P. (1978). "Coupling boundary integral equation methods to other numerical techniques," in Recent Advances in Boundary Element Methods, Brebbia, C.A. (ed.), Pentech Press, London: Plymouth.

Shoamanesh, A. and Shafai, L. (1976). "An approximate method for investigation of large circular loop arrays," in Large Engineering Systems, Proc. Int. Symp., Wexler, A. (ed.), Pergamon Press, 120-138.

Stakgold, I. (1967). Boundary Value Problems of Mathematical Physics, Vol. I, Macmillan, New York.

Stakgold, I. (1968). Boundary Value Problems of Mathematical Physics, Vol. II, Macmillan, New York.

Stakgold, I. (1979). Green's Functions and Boundary Value Problems, John Wiley & Sons, Inc., New York.

Stroud, A.H. and Secrest, D. (1966). Gaussian Quadrature Formulas, Prentice-Hall, Englewood Cliffs, N.J.

Telford, W.M., Geldart, L.P., Sheriff, R.E. and Keys, D.A. (1976). Applied Geophysics, Cambridge University Press, London, 632-642.

Thiele, G.A. (1973). "Wire antennas," in Computer Techniques for Electromagnetics, Mittra, R. (ed.), Pergamon Press Ltd., New York.

Thiele, G.A. and Newhouse, T.H. (1975). "A hybrid technique for combining moment methods with the Geometrical Theory of Diffraction," IEEE Trans. Antennas & Propagation, vol. AP-23, 62-69.

Van Bladel, J. (1964). Electromagnetic Fields, McGraw-Hill, New York.

Waterman, P.C. (1965). "Matrix formulation of electromagnetic scattering," Proc. IEEE, vol. 53, 805-812.

Waterman, P.C. (1973). "Numerical solution of electromagnetic scattering problems," in Computer Techniques for Electromagnetics, Mittra, R. (ed.), Pergamon Press Ltd., New York.

Wexler, A. (1969). "Computation of electromagnetic fields," (Invited Paper), IEEE Trans. Microwave Theory & Techniques, vol. 17, 416-439.

Wexler, A. (1979). Perspectives on the Solution of Simultaneous Equations, Tech. Rept. TR 79-2, Dept. of Elec. Eng., University of Manitoba, Winnipeg, Canada.

Wexler, A. (1980). Finite Elements for Technologists, Tech. Rept. TR 80-4, Dept. of Elec. Eng., University of Manitoba, Winnipeg, Canada.

Zabreyko, P.P., Koshelev, A.I., Krasnosel'skii, M.A., Mikhlin, S.G., Rakovshchik, L.S. and Stet'senko, V. Ya. (1975). Integral Equations - a Reference Text, Noordhoff International Publishing, Leyden, The Netherlands.